NAG2-541

025921-31-T

A finite element—boundary integral method for electromagnetic scattering

J. D. Collins and J. L. Volakis

National Aeronautics and
Space Administration
Ames Research Center
Moffett Field CA 94035

Pacific Missile Test Center
Pt. Mugu CA 93042-5000

Mission Research Corp.
3975 Research Blvd.
Dayton OH 45430

Northrop Corp.
8900 E. Washington Blvd.
Pico Rivera CA 90660

June 1992

THE UNIVERSITY OF MICHIGAN

Radiation Laboratory
Department of Electrical Engineering
and Computer Science
Ann Arbor, Michigan 48109-2122
USA

TECHNICAL REPORT

for NASA Grant NAG-2-541

NASA Technical Monitor: Alex Woo

Grant Title:

Development of 3D Electromagnetic Modeling Tools
for Airborne Vehicles

Report Title:

A Finite Element–Boundary Integral Method for
Electromagnetic Scattering

Institution:

Radiation Laboratory
Department of Electrical Engineering
 and Computer Science
The University of Michigan
Ann Arbor MI 48109-2122

Period Covered:

Feb. 1992 – Sept. 1992

Report Authors:

J.D. Collins and J.L. Volakis

Principal Investigator:

John L. Volakis
Telephone: (313) 764-0500

I

A finite element–boundary integral method for electromagnetic scattering

J. D. Collins[1] and J. L. Volakis

Radiation Laboratory
Department of Electrical Engineering
and Computer Science
The University of Michigan
Ann Arbor MI 48109-2122

PRECEDING PAGE BLANK NOT FILMED

iii

ABSTRACT

A Finite Element – Boundary Integral Method for Electromagnetic Scattering

A method that combines the finite element and boundary integral techniques for the numerical solution of electromagnetic scattering problems is presented. The finite element method is well known for requiring a low order storage and for its capability to model inhomogeneous structures. Of particular emphasis in this work is the reduction of the storage requirement by terminating the finite element mesh on a boundary in a fashion which renders the boundary integrals in convolutional form. The fast Fourier transform is then used to evaluate these integrals in a conjugate gradient solver, without a need to generate the actual matrix. This method has a marked advantage over traditional integral equation approaches with respect to the storage requirement of highly inhomogeneous structures.

Rectangular, circular and ogival mesh termination boundaries are examined for two-dimensional scattering. In the case of axially symmetric structures, the boundary integral matrix storage is reduced by exploiting matrix symmetries and solving the resulting system via the conjugate gradient method. In each case, several results are presented for various scatterers aimed at validating the method and providing an assessment of its capabilities.

Important in methods incorporating boundary integral equations is the issue of internal resonance. A method is implemented for their removal, and is shown to be effective in the two-dimensional and three-dimensional applications.

TABLE OF CONTENTS

LIST OF FIGURES

ix

LIST OF TABLES

CHAPTER I

Introduction

Over the years, integral equation (IE) techniques have been employed for evaluating the electromagnetic fields scattered from various structures. Special cases of the IE methods are surface integral equation (SIE) methods and volume integral equation (VIE) methods, which have been the workhorses in computational electromagnetics for the past two decades. They have been used to solve the scattering from simple structures, such as smooth perfectly conducting bodies and homogeneous material structures to more complicated ones such as multi–layered coated conductors. However, the classical SIE and VIE techniques result in fully populated matrices whose required storage is $O(N^2)$, where N is the number of unknowns in the model. Consequently, as the size of the structure increases, the memory demand may become much greater than the storage available on existing computing resources. To circumvent this, the IE may be cast in convolutional form by a proper choice of the discretization model. The resulting system can then solved via the conjugate gradient method, using the fast Fourier transform (FFT) to evaluate the discrete integral operator. The use of the FFT requires storage on the same order as the dimensionality of the scattering body (i.e., $O(N_d^3)$ for three–dimensional scatterers using VIE, where N_d denotes the number of cells per dimension), but is still lower than that required

by the fully populated version. This method, referred to as the CGFFT method has been recently employed by several authors to solve two–dimensional (2–D) and three–dimensional (3–D) inhomogeneous scattering problems [1, 2, 3]. Nevertheless, for 3–D applications the storage requirement remains problematic and furthermore, rectangular grid meshing results in a stair–case approximation of otherwise smooth scatterers.

In an effort to further reduce the storage requirement, partial differential equation (PDE) methods were considered, since these methods provide for an $O(N)$ storage requirement. Among them are the finite difference (FD) methods [4] and finite element (FE) methods [5]. Finite difference techniques typically suffer from the same staircasing problems as the CGFFT methods and may have difficulties in modeling numerical dispersion when solved in the time domain (TD). Frequency domain solutions (of primary interest in this study) allow for accurate (conformal) modeling of the scattering structure since, for instance, triangles and tetrahedrals can be used for discretizing surfaces and volumes, respectively. However, when the finite element method (or any other PDE method) is employed, the mesh must be truncated at a distance from the structure on which an approximate or exact boundary condition is applied.

Various methods for truncating the FE mesh have been employed. Among them are the simple enforcement of an approximate absorbing boundary conditions (ABC) at the mesh boundary and the unimoment method. The ABC's are popular because they result in a banded sub–matrix structure. However, they require additional unknowns since the enclosure must be placed at a distance approximating the far field region. This distance may be large for structures with sharp edges and as a result a large number of unknowns is required, especially for 3–D applications. In the

unimoment method [6], the scattered field in the unbounded region is represented by an eigenfunction expansion. The coefficients of the expansion are then determined by enforcing continuity at the circular mesh termination boundary. This method produces a dense square sub–matrix whose dimension is proportional to the number of modes. It also requires the truncation of an infinite series which may be slowly convergent for irregular structures, thus resulting in a large storage requirement.

An exact termination method is the boundary integral equation, first introduced by Hsieh [7] and McDonald and Wexler [8] in the early 1970's. The method is heretofore referred to as the finite element – boundary integral (FE–BI) technique and is the subject of this thesis. The boundary integral equation employs the free–space Green's function which implicitly satisfies the radiation condition at infinity. Since the integral equation is exact, the mesh termination boundary may be brought very close to the scatterer to minimize the meshing of the free–space regions enclosed by the termination boundary. The main drawback of the method is again the dense submatrix structure associated with the boundary integral equation. However, by carefully choosing the shape of the boundary, some of the boundary integral terms are cast into convolution form. Thus, on employing a conjugate gradient solver, these integral operators may be evaluated via the FFT as was done in the CGFFT method. The required storage of the boundary integral is then reduced toward $O(N)$ and allows for the accurate solution of large inhomogeneous scatterers as well as small targets.

In this thesis, the FE–BI technique (presented in general terms in chapter II) is developed for two–dimensional and axial–symmetric structures. The two–dimensional case is based on [9]. Chapter III contains a FE–BI formulation for rectangular enclosures, leading to simple boundary integrals some of which have convolutional form,

thus leading to a reduction in the memory requirement. In chapter IV, circular and ogival enclosures are considered. For the circular boundary, the boundary integral is entirely convolutional in form and an $O(N)$ storage requirement is thus achieved at all times. Circular enclosures are consequently preferred for storage efficiency if the structure's outer boundary does not substantially deviate from a circle.

In chapter VI, the FE–BI formulation is developed for axially symmetric structures. The finite element method for this problem was originally developed by Morgan and Mei using the coupled azimuthal potential (CAP) equations for generating the FE matrix system. In that formulation, the unimoment method was employed for terminating the mesh, whereas in our implementation the boundary integral equation is instead employed for this purpose. It is related to Flemings implementation [10] for circular boundaries, but the present formulation allows for an arbitrarily shaped enclosure. Consequently the boundary integrals are no longer convolutional and the storage reduction is in this case achieved by exploiting certain symmetry properties of the boundary integral subsystem. A problem with the CAP equations is the presence of a singularity in the finite elements which tends to corrupt the solution, and a method is presented for circumventing this difficulty.

A difficulty with most boundary integral formulations is the appearance of internal resonances which corrupt the solution. These resonances correspond to the eigenvalues of the integral operator, and also occur at the same location as the cut–off frequencies of a resonator with conducting walls of the same shape as the mesh termination boundary and filled with the same material as the unbounded medium. The resonances are particularly problematic when the structure becomes electrically large, in which case the eigenvalues are very closely spaced. Without any correction, computations for large structures are unreliable, and a method for correcting the

resonance problem is developed in chapter V.

Specific contributions of this work include the implementation of the FE–BI for rectangular, circular and ogival boundaries as described in chapters III and IV in a manner taking advantage of storage reduction schemes. A new method is also presented for suppressing the resonance corruption problem existing in almost all implementations employing some form of a boundary integral equation over a closed surface or contour. This method involves the introduction of a complex wavenumber and is demonstrated for both 2–D and axial–symmetric bodies. The implementation of the FE–BI method for axially symmetric structures as described in chapter VI is for the most part new and incorporates a scheme for treating the line singularity associated with the CAP equations. This resulted in real matrices for lossless scatterers, a property consistent with 2–D and 3–D implementations of the finite element method.

CHAPTER II

Fundamental Concepts

In this chapter, some basic concepts are presented as applied to electromagnetic scattering and its computation via the FE–BI method. At the end of the chapter, the conjugate gradient matrix solver is also appended.

2.1 Basic Electromagnetic Theory

The overall goal in any electromagnetic problem is the solution of Maxwell's equations subject to given boundary conditions. In the frequency domain, Maxwell's equations in free space are

$$\nabla \times \overline{E} = -j\omega\mu\overline{H} \tag{2.1}$$

$$\nabla \times \overline{H} = j\omega\epsilon\overline{E} \tag{2.2}$$

$$\nabla \cdot (\epsilon\overline{E}) = 0 \tag{2.3}$$

$$\nabla \cdot (\mu\overline{H}) = 0 \tag{2.4}$$

where

$$\overline{E}(\overline{r}) = \text{electric field strength [Volts/meter]} \tag{2.5}$$

$$\overline{H}(\overline{r}) = \text{magnetic field strength [Amperes/meter]} \tag{2.6}$$

$$\epsilon(\overline{r}) = \text{electric permittivity [Henrys/meter]} \tag{2.7}$$

$$\mu(\bar{r}) = \text{magnetic permeability [Farads/meter]} \qquad (2.8)$$

Note that the last two equations, which are based on Gauss' law, can be obtained by taking the divergence of the first two equations. Thus for time harmonic fields, only the first two of Maxwell's equations are needed for a unique solution of $\bar{E}$ and $\bar{H}$.

By substituting (2.2) into (2.1) and vice versa, we obtain

$$\nabla \times \frac{1}{\mu} \nabla \times \bar{E} - \omega^2 \epsilon \bar{E} = 0 \qquad (2.9)$$

$$\nabla \times \frac{1}{\epsilon} \nabla \times \bar{H} - \omega^2 \mu \bar{H} = 0 \qquad (2.10)$$

which are commonly referred to as the vector wave equations. They must be solved and are subject to the boundary conditions on the particular scatterer as well as the radiation condition. Typically when solving (2.9) and (2.10) for a piecewise homogeneous scatterer, the following conditions must be explicitly imposed:

- Continuity of tangential $\bar{E}$ and $\bar{H}$

- Continuity of normal $\mu\bar{H}$ and $\epsilon\bar{E}$

- Tangential $\bar{E} = 0$ on metallic surfaces

For radiation and scattering problems, the radiation condition must be also satisfied. This condition assumes that the wave must be outwardly propagating and must attenuate no slower than the inverse of the distance far from the source. Expressed in mathematical terms,

$$\lim_{r \to \infty} [\eta \bar{H} - \hat{r} \times \bar{E}] = 0 \qquad (2.11)$$

$$\lim_{r \to \infty} [\bar{E} - \hat{r} \times \eta \bar{H}] = 0 \qquad (2.12)$$

where $\eta = \sqrt{\frac{\mu}{\epsilon}}$ is the impedance of unbounded medium and $\hat{r}$ is the unit radial vector in spherical coordinates.

The media considered is this work is linear and isotropic and the material parameters μ and ϵ are often normalized to their free space (vacuum) values of $\epsilon_0 \simeq$ 8.85 $\times$ 10^{-12} H/m and $\mu_0 = 4\pi \times 10^{-7}$ F/m. The relative constitutive parameters of the medium will be denoted by

$$\epsilon_r = \frac{\epsilon}{\epsilon_0} \tag{2.13}$$

$$\mu_r = \frac{\mu}{\mu_0} \tag{2.14}$$

A fundamental solution of the wave equation is the plane wave

$$E(\bar{r}) = e^{-j\bar{k}\cdot\bar{r}} \tag{2.15}$$

where $k = \omega\sqrt{\mu\epsilon}$ and $\omega = 2\pi f$ is the frequency in rad/sec. For lossy media, μ and ϵ are complex and thus $k = k_r + jk_i$, implying an exponentially decaying field. Note that the required condition, $k_i \leq 0$, ensures that the wave does not grow exponentially and, consequently, the imaginary part of μ and ϵ must likewise be less than zero.

2.2   The FE–BI Approach

To solve PDE's (2.9) and (2.10), the scattering body is first enclosed in an artificial surface S bounding a volume V and for this application all sources will be assumed to reside in the unbounded region outside S. To satisfy Maxwell's equations in this volume, the vector wave equation for the electric field in (2.9) is discretized via the method of weighted residuals. Though not given here, a similar approach in terms of the magnetic field may developed in a parallel fashion.

The volume V is first divided into N_e elements. Within each element, the weighted residual expression is given by

$$\iiint\limits_{V^e} \overline{W}_i^e \cdot (\nabla \times \frac{1}{\mu} \nabla \times \overline{E} - \omega^2 \epsilon \overline{E}) dV = 0 \tag{2.16}$$

where W_i^e is the ith weighting function over the eth element. First, we temporarily define $\overline{A}$ as

$$\overline{A} = \frac{1}{\mu}\nabla \times \overline{E} \qquad (2.17)$$

and recall the identity

$$\overline{W_i^e} \cdot \nabla \times \overline{A} = \nabla \cdot (\overline{A} \times \overline{W_i^e}) + \overline{A} \cdot \nabla \times \overline{W_i^e} \qquad (2.18)$$

Using this identity, the first term in (2.16) can be rewritten as

$$\iiint_{V^e} \overline{W_i^e} \cdot \nabla \times \overline{A}dV^e = \iiint_{V^e} \nabla \cdot (\overline{A} \times \overline{W_i^e})dV^e + \iiint_{V^e} \overline{A} \cdot \nabla \times \overline{W_i^e}dV^e$$

$$= \oiint_{S^e} \hat{n}^e \cdot (\overline{A} \times \overline{W_i^e})dS^e + \iiint_{V^e} \overline{A} \cdot \nabla \times \overline{W_i^e}dV^e \qquad (2.19)$$

where the last equality was obtained by invoking the divergence theorem and thus, S^e is the surface enclosing V^e and $\hat{n}^e$ is its outward unit normal. Substituting (2.19) into (2.16) yields

$$\iiint_{V^e} \left[(\frac{1}{\mu}\nabla \times \overline{E}) \cdot (\nabla \times \overline{W_i^e}) - \omega^2\epsilon\overline{E}\right] dV^e = \oiint_{S^e} \hat{n}^e \cdot (\frac{1}{\mu}\nabla \times \overline{E}) \times \overline{W_i^e}dS^e \qquad (2.20)$$

and upon rearranging this we have

$$\iiint_{V^e} \left[(\frac{1}{\mu}\nabla \times \overline{E}) \cdot (\nabla \times \overline{W_i^e}) - \omega^2\epsilon\overline{E}\right] dV^e = \oiint_{S^e} j\omega\overline{W_i^e} \cdot (\hat{n}^e \times \overline{H})dS^e \qquad (2.21)$$

For scatterers comprised in part of conducting material, the surface boundary of the volume V is $S = S_a + S_c$, where the subscript a denotes the exterior boundary and the subscript c denotes the conducting boundary. In the assembly of the finite element equations, the fully discretized form of (2.21) is summed over all elements. Since the tangential fields are continuous across material interfaces, the surface integral in (2.21) will cancel everywhere except on S_a and S_c. Thus, unless S^e intersects S_a or S_c, the surface integral may be removed.

To construct a system of equations from (2.21), the field in element e may be represented as

$$\overline{E}^e = \sum_{j=1}^{n} \overline{N}_j^e(x,y,z) E_j^e \qquad (2.22)$$

$$\hat{n} \times \overline{E}^e = \sum_{j=1}^{m} \hat{n} \times \overline{N}_j^e(x,y,z) E_j^{te} \qquad (2.23)$$

$$\hat{n} \times \overline{H}^e = \sum_{j=1}^{m} \hat{n} \times \overline{N}_j^e(x,y,z) H_j^{te} \qquad (2.24)$$

where the superscript t denotes the tangent to the boundary of element e. (These vector shape functions must also be chosen to satisfy the divergence condition given by (2.3).) Substituting this expansion into (2.21) and using Galerkin's approach (i.e., $\overline{W}_i^e = \overline{N}_i^e$) gives

$$\sum_{j=1}^{n} E_j^e \iiint_{V^e} \frac{1}{\mu} \left[(\nabla \times \overline{N}_i^e) \cdot (\nabla \times \overline{N}_j^e) - k^2 \overline{N}_i^e \overline{N}_j^e \right] dV^e$$

$$= \sum_{j=1}^{n} H_j^{te} \oiint_{\substack{S^e \in S_a}} j\omega \overline{N}_i^e \cdot (\hat{n}^e \times \overline{N}_j^e) dS^e + \sum_{j=1}^{n} H_j^{te} \oiint_{\substack{S^e \in S_c}} j\omega \overline{N}_i^e \cdot (\hat{n}^e \times \overline{N}_j^e) dS^e \quad (2.25)$$

where $k = \omega\sqrt{\mu\epsilon}$.

After summing over all elements, our system takes the form

$$\begin{bmatrix} K_{aa}^{nn} & K_{aa}^{nt} & K_{aI}^{n} & K_{ac}^{nt} & K_{ac}^{nn} & 0 \\ K_{aa}^{tn} & K_{aa}^{tt} & K_{aI}^{t} & K_{ac}^{tt} & K_{ac}^{tn} & B_{aa} \\ K_{Ia}^{n} & K_{Ia}^{t} & K_{II} & K_{Ic}^{t} & K_{Ic}^{n} & 0 \\ K_{ca}^{nn} & K_{ca}^{nt} & K_{cI}^{n} & K_{cc}^{nn} & K_{cc}^{nt} & 0 \\ K_{ca}^{tn} & K_{ca}^{tt} & K_{cI}^{t} & K_{cc}^{tn} & K_{cc}^{tt} & 0 \end{bmatrix} \begin{bmatrix} \{E_a^n\} \\ \{E_a^t\} \\ \{E_I\} \\ \{E_c^n\} \\ \{E_c^t\} \\ \{H_a^t\} \end{bmatrix} = \begin{bmatrix} 0 \\ 0 \\ 0 \\ 0 \\ B_{cc}H_c^t \end{bmatrix} \qquad (2.26)$$

In these the subscript a refers to unknowns on S_a, c refers to the set of unknowns on S_c and I refers to the remaining unknowns. Furthermore, the superscripts n and t refer to the normal and tangential components, respectively, of the weighting and/or

testing functions. The application of the boundary condition on S_c results in the following system

$$
\begin{bmatrix}
K_{aa}^{nn} & K_{aa}^{nt} & K_{aI}^{n} & K_{ac}^{nt} & 0 & 0 \\
K_{aa}^{tn} & K_{aa}^{tt} & K_{aI}^{t} & K_{ac}^{tt} & 0 & B_{aa} \\
K_{Ia}^{n} & K_{Ia}^{t} & K_{II} & K_{Ic}^{t} & 0 & 0 \\
K_{ca}^{nn} & K_{ca}^{nt} & K_{cI}^{n} & K_{cc}^{nn} & 0 & 0 \\
0 & 0 & 0 & 0 & I & 0
\end{bmatrix}
\begin{bmatrix}
\{E_a^n\} \\
\{E_a^t\} \\
\{E_I\} \\
\{E_c^n\} \\
\{E_c^t\} \\
\{H_a^t\}
\end{bmatrix}
=
\begin{bmatrix}
0 \\
0 \\
0 \\
0 \\
0 \\
0
\end{bmatrix}
\tag{2.27}
$$

Clearly, another equation is necessary relating E_a^t and H_a^t on S_a. The FE–BI approach employs the Stratton–Chu integral equation for the purpose. This equation relates the electric and magnetic fields via the integral equation

$$
\overline{E}(\overline{r}) = \overline{E}^i(\overline{r}) + \oiint_{S'} \left\{ -jk_0\left[\hat{n}' \times \eta_0 \overline{H}(\overline{r}')\right]g(\overline{r},\overline{r}') + \frac{1}{jk_0}\left[\hat{n}' \cdot \nabla' \times \eta_0 \overline{H}(\overline{r}')\right]\nabla'g(\overline{r},\overline{r}') \right.
$$
$$
\left. + \left[\hat{n}' \times \overline{E}(\overline{r}')\right] \times \nabla'g(\overline{r},\overline{r}')\right\}dS'
$$

$$\tag{2.28}$$

where $\eta_0 = \sqrt{\mu_0/\epsilon_0}$ and g is the free space Green's function. Evaluating this equation on the surface S_a and discretizing it, we obtain the subsystem

$$
L_{aa}^t\{E_a^t\} + M_{aa}^t\{H_a^t\} = U_a^i \tag{2.29}
$$

which relates the tangential fields on S_a. Combining (2.29) and (2.27) we obtain the

block matrix

$$
\begin{bmatrix}
K_{aa}^{nn} & K_{aa}^{nt} & K_{aI}^{n} & K_{ac}^{nt} & 0 & 0 \\
K_{aa}^{tn} & K_{aa}^{tt} & K_{aI}^{t} & K_{ac}^{tt} & 0 & B_{aa} \\
K_{Ia}^{n} & K_{Ia}^{t} & K_{II} & K_{Ic}^{t} & 0 & 0 \\
K_{ca}^{nn} & K_{ca}^{nt} & K_{cI}^{n} & K_{cc}^{nn} & 0 & 0 \\
0 & 0 & 0 & 0 & I & 0 \\
0 & L_{aa}^{t} & 0 & 0 & 0 & M_{aa}^{t}
\end{bmatrix}
\begin{bmatrix}
\{E_a^n\} \\
\{E_a^t\} \\
\{E_I\} \\
\{E_c^n\} \\
\{E_c^t\} \\
\{H_a^t\}
\end{bmatrix}
=
\begin{bmatrix}
0 \\
0 \\
0 \\
0 \\
0 \\
\{U_a^i\}
\end{bmatrix}
\tag{2.30}
$$

which, after applying the condition on S_c, can be solved uniquely for the interior and boundary fields. The resulting system is then solved via the conjugate gradient method.

After the fields in the solution region have been determined, the scattered fields are computed by evaluating the integral equation in the far zone. In particular a quantity called the echowidth is computed for 2-D problems and is given by [11]

$$
\sigma = \lim_{\rho \to \infty} 2\pi\rho \frac{|\phi^s|^2}{|\phi^i|^2}
\tag{2.31}
$$

where ρ is the usual cylindrical coordinate and ϕ denotes either E_z or H_z. For three-dimensional applications, the quantity of interest is the radar cross section (RCS) and its expression is

$$
\sigma = \lim_{r \to \infty} 4\pi r^2 \frac{|\overline{E}^s(\overline{r})|^2}{|\overline{E}^i(\overline{r})|^2}
\tag{2.32}
$$

where r is the radial spherical coordinate. Expressed in component form we have

$$
\sigma_{pq} = \lim_{r \to \infty} 4\pi r^2 \frac{|E_p^s(\overline{r})|^2}{|E_q^i(\overline{r})|^2}
\tag{2.33}
$$

where p and q represent the polarization of the scattered and incident fields, respectively.

2.3   The Conjugate Gradient Method

The CG algorithm is employed throughout this work and is given as follows for solving the system $Ax = b$.

Initialize the residual and search vectors

$$\gamma_b = \| \, [\, \phi^{inc} \quad 0 \quad 0 \quad 0 \,]^T \, \|_2^2 = \| \, b \, \|_2^2$$

$$s = A\phi^{(0)}$$

$$r^{(1)} = b - s$$

$$s = A^a r^{(1)}$$

$$\gamma_s = \| \, s \, \|_2^2$$

$$\beta^{(0)} = \gamma_s^{-1}$$

$$p^{(1)} = \beta^{(0)} s$$

Iterate for $k = 1, ..., N_g$

$$s = Ap^{(k)}$$

$$\gamma_s = \| \, s \, \|_2^2$$

$$\alpha^{(k)} = \gamma_s^{-1}$$

$$\phi^{(k+1)} = \phi^{(k)} + \alpha^{(k)} p^{(k)}$$

$$r^{(k+1)} = r^{(k)} - \alpha^{(k)} p^{(k)}$$

$$\gamma_r = \| \, r^{(k+1)} \, \|_2^2$$

$$s = A^a r^{(k+1)}$$

$$\gamma_s = \| \, s \, \|_2^2$$

$$\beta^{(k)} = \gamma_s^{-1}$$

$$p^{(k+1)} = p^{(k)} + \beta^{(k)} s^{(k)}$$

Terminate when $k = N_g$ or $\sqrt{\frac{\gamma_x}{\gamma_b}} < $ tolerance.

The given tolerance must be used with caution. In each of the FE–BI techniques developed, the excitation b is only partially full. If the simple preconditioner of dividing by the diagonal value is employed, then those rows associated with an excitation component of zero will consequently not scale the excitation. In other words for those rows, b will not change in value while the matrix itself does. As a result, the residual error will be scaled differently and, consequently, the tolerance criterion will be scaled differently as well. This may lead to artificially small normalized residual errors and cause the convergence criterion to be satisfied before convergence is actually achieved.

One way to avoid this is to compute the far field in terms of σ at one or more angles every few iterations and compare the current value to the previous one. When the difference is sufficiently small for 15 or 20 consecutive iterations, convergence is assumed to have been achieved.

CHAPTER III

A Finite Element – Boundary Integral Formulation for Two-dimensional Scattering with a Rectangular Termination Boundary

3.1 Introduction

In this section an FE–BI method is developed for two-dimensional scattering in which the exterior boundary is rectangular in shape. This enclosure ensures some of the boundary integral terms are convolutional and are therefore amenable to evaluation via the FFT in the conjugate gradient solver. Results are presented for several structures.

3.2 Analysis

Consider a cylindrical body of arbitrary cross-section and composition illuminated by the plane wave

$$\overline{\phi}^{inc}(\overline{\rho}) = \hat{z}\phi_z^{inc}(\overline{\rho}) = \hat{z}e^{jk_o\rho\cos(\theta-\theta_o)} \tag{3.1}$$

as indicated in Fig. 3.1. To evaluate the fields scattered from this object, two boundaries are placed tightly around the body as shown in Fig. 3.2. Inside the outer boundary, the Finite Element Method is applied to solve the Helmholtz equation
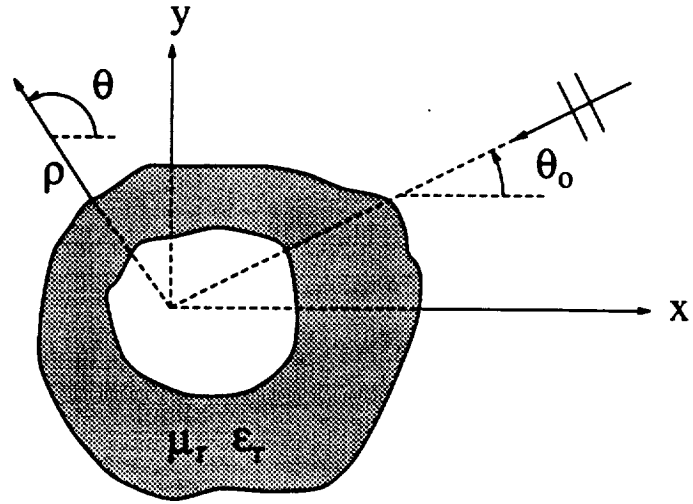
Figure 3.1: Geometry of the scatterer
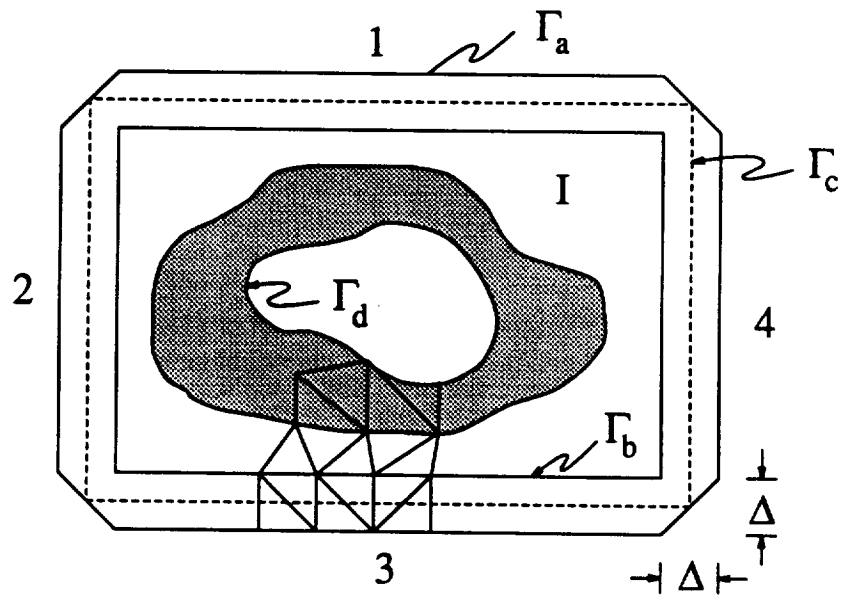
Figure 3.2: Partially discretized body

given by

$$\nabla \cdot [v(\overline{p})\nabla\phi(\overline{p})] + k_o^2 u(\overline{p})\phi(\overline{p}) = 0 \tag{3.2}$$

where

$$\phi(\overline{p}) = E_z(\overline{p}) \tag{3.3}$$

$$v(\overline{p}) = \frac{1}{\mu_r(\overline{p})} \tag{3.4}$$

$$u(\overline{p}) = \epsilon_r(\overline{p}) \tag{3.5}$$

for E-polarization and

$$\phi(\overline{p}) = H_z(\overline{p}) \tag{3.6}$$

$$v(\overline{p}) = \frac{1}{\epsilon_r(\overline{p})} \tag{3.7}$$

$$u(\overline{p}) = \mu_r(\overline{p}) \tag{3.8}$$

for H-polarization. Also, $k_o = \omega\sqrt{\mu_o\epsilon_o}$ is the wave number, and μ_r and ϵ_r are the relative permeablility and permittivity, respectively.

The appropriate boundary condition is enforced on the surface of the impenetrable boundary, while the radiation condition is satisfied implicitly by evaluating the integral equation

$$\phi(\overline{p}) = \phi^{\text{inc}}(\overline{p}) - \oint_{\Gamma_c}\left\{G(\overline{p},\overline{p}')\left[\frac{\partial}{\partial n'}\phi(\overline{p}')\right] - \phi(\overline{p}')\left[\frac{\partial}{\partial n'}G(\overline{p},\overline{p}')\right]\right\}dl' \tag{3.9}$$

on the boundary Γ_a, where

$$G(\overline{p},\overline{p}') = -\frac{j}{4}H_o^{(2)}(k_o|\overline{p} - \overline{p}'|) \tag{3.10}$$

is the 2-D Green's function in which $H_o^{(2)}(\cdot)$ denotes the zeroth order Hankel function of the second kind. Furthermore, $\overline{p}$ and $\overline{p}'$ are the usual observation and source position vectors, respectively, and

$$|\overline{p} - \overline{p}'| = \sqrt{(x - x')^2 + (y - y')^2} \tag{3.11}$$

Symbol	Description
N_g	number of nodes in the finite element mesh
N_e	number of elements in the finite element mesh
N_x	number of nodes on Γ_a or Γ_b along the x-direction
N_y	number of nodes on Γ_a or Γ_b along the y-direction
N_a	total number of nodes on Γ_a
N_b	total number of nodes on Γ_b
N_{ab}	$N_a + N_b$
Γ_a	$\sum_{i=1}^{4} \Gamma_{a_i}$
Γ_b	$\sum_{i=1}^{4} \Gamma_{b_i}$
Γ_c	$\sum_{i=1}^{4} \Gamma_{c_i}$
(x_{a_i}, y_{a_i})	coordinates of a point on contour Γ_{a_i}
(x_{b_i}, y_{b_i})	coordinates of a point on contour Γ_{b_i}

Table 3.1: Definitions for the finite element mesh

The normal derivatives are taken in the direction of the outward normal of Γ_c.

3.2.1 Discretization of the Object and Field Quantities

In Fig. 3.2, Γ_a is the field/observation point boundary, and Γ_c is the integration contour, which is placed midway between Γ_a and Γ_b. Also, Γ_d denotes the contour enclosing the impenetrable portion of the scatterer. Herewith, each side of Γ_a, Γ_b and Γ_c are numbered counterclockwise starting from the top side, as indicated in Fig. 3.2. The fields in the region between Γ_a and Γ_d satisfy (3.2) in conjunction with the required boundary condition on Γ_d. The boundary integral equation (3.9) will be enforced on Γ_a.

Symbol	Description
ϕ_{a_i}	nodal fields on Γ_{a_i}
ϕ_{b_i}	nodal fields on Γ_{b_i}
ϕ'_{b_i}	nodal fields on Γ_{b_i}
ϕ_d	nodal fields on Γ_d
ϕ_I	region enclosed by Γ_b and Γ_d, exclusive

Table 3.2: Definitions of the field vectors

To numerically solve (3.2), it is required that the region within Γ_a be discretized. This is done in a traditional manner when employing the finite element method. The global node numbering starts from the right endpoint of contour Γ_{a_1} and proceeds counterclockwise. The numbering continues beginning at the right endpoint of contour Γ_{b_1} and proceeds counterclockwise. Within Γ_b, the nodes are numbered arbitrarily. The definitions pertaining to the FE mesh are given in Table 3.1. Each node corresponds to an unknown field value to be determined. It is important to associate the unknown field values corresponding to the various node groups on contours Γ_a and Γ_b by using different variables. The labeling scheme is given in Table 3.2, and this discrimination of the nodal fields is required, since they are treated differently in the analysis.

3.2.2 Derivation of the Finite Element Matrix

One of several approaches may be used to generate the finite element matrix, such as the variational approach or the method of weighted residuals. In this development, we will utilize Galerkin's method, which is a special case of the method of weighted

residuals with the distinction that the testing functions are the same as the basis functions.

Proceeding with the finite element analysis, we may rewrite (3.2) as

$$\frac{\partial}{\partial x}\left[v(x,y)\frac{\partial}{\partial x}\phi(x,y)\right] + \frac{\partial}{\partial y}\left[v(x,y)\frac{\partial}{\partial y}\phi(x,y)\right] + k_o^2 u(x,y)\phi(x,y) = 0 \quad (3.12)$$

the residual of which is given by

$$R = -\frac{\partial}{\partial x}\left[v(x,y)\frac{\partial}{\partial x}\phi(x,y)\right] - \frac{\partial}{\partial y}\left[v(x,y)\frac{\partial}{\partial y}\phi(x,y)\right] - k_o^2 u(x,y)\phi(x,y) \quad (3.13)$$

The field within Γ_a may be represented as a summation of piecewise continuous functions and, thus, may be written as

$$\phi(x,y) = \sum_{e=1}^{N_e} \phi^e(x,y) \quad (3.14)$$

where $\phi^e(x,y)$ is the field within element e. It is expanded as

$$\phi^e(x,y) \simeq \sum_{j=1}^{n} N_j^e(x,y)\,\phi_j^e \quad (3.15)$$

where N_i^e's are the standard shape functions (found in any standard finite element book), ϕ_i^e's are the fields at the nodes, and n is the number of nodes per element ($n = 3$ for linear elements considered here). The weighted residual equation for the eth element is defined by

$$\iint_{S^e} N_i^e R\, dx dy = 0 \quad i = 1, ..., n \quad (3.16)$$

where S^e denotes the surface area of the eth element. Inserting (3.15) and (3.13) into (3.16) yields

$$\sum_{j=1}^{n}\iint_{S^e} N_i^e\left[-\frac{\partial}{\partial x}\left(v\frac{\partial N_j^e}{\partial x}\right) - \frac{\partial}{\partial y}\left(v\frac{\partial N_j^e}{\partial y}\right) - k_o^2 u N_j^e\right]\phi_j^e\, dx dy = 0$$

$$i = 1, 2, ..., n \quad (3.17)$$

Further, by using the identities

$$N_i^e \frac{\partial}{\partial x} \left(v \frac{\partial N_j^e}{\partial x} \right) = \frac{\partial}{\partial x} \left(v \frac{\partial N_j^e}{\partial x} N_i^e \right) - v \frac{\partial N_i^e}{\partial x} \frac{\partial N_j^e}{\partial x} \tag{3.18}$$

$$N_i^e \frac{\partial}{\partial y} \left(v \frac{\partial N_j^e}{\partial y} \right) = \frac{\partial}{\partial y} \left(v \frac{\partial N_j^e}{\partial y} N_i^e \right) - v \frac{\partial N_i^e}{\partial y} \frac{\partial N_j^e}{\partial y} \tag{3.19}$$

and the divergence theorem

$$\iint_{S^e} \left(\frac{\partial u}{\partial x} + \frac{\partial v}{\partial y} \right) dx dy = \oint_{C^e} \hat{n} \cdot (u\hat{x} + v\hat{y}) \, dl \tag{3.20}$$

where C^e is the contour enclosing the eth element, (3.17) becomes

$$\sum_{j=1}^{n} \iint_{S^e} \left(v \frac{\partial N_i^e}{\partial x} \frac{\partial N_j^e}{\partial x} + v \frac{\partial N_i^e}{\partial y} \frac{\partial N_j^e}{\partial y} - k_o^2 u N_i^e N_j^e \right) \phi_j^e \, dx dy$$

$$= \sum_{j=1}^{n} \oint_{C^e} N_i^e \phi_j^e \left(v \frac{\partial N_j^e}{\partial x} \hat{x} + v \frac{\partial N_j^e}{\partial y} \hat{y} \right) \cdot \hat{n} \, dl \quad i = 1, 2, ..., n \tag{3.21}$$

This may be written in matrix form as

$$A^e \phi^e = b^e \tag{3.22}$$

where

$$[A^e]_{ij} = \iint_{S^e} \left(v \frac{\partial N_i^e}{\partial x} \frac{\partial N_j^e}{\partial x} + v \frac{\partial N_i^e}{\partial y} \frac{\partial N_j^e}{\partial y} - k_o^2 u N_i^e N_j^e \right) dx dy \tag{3.23}$$

and

$$\{b^e\}_i = \sum_{j=1}^{n} \oint_{C^e} N_i^e \phi_j^e \left(v \frac{\partial N_j^e}{\partial x} \hat{x} + v \frac{\partial N_j^e}{\partial y} \hat{y} \right) \cdot \hat{n} \, dl \quad i = 1, 2, ..., n \tag{3.24}$$

For linear triangular elements, N_i^e are given by

$$N_i^e = \frac{1}{2\Omega^e} (a_i^e + b_i^e x + c_i^e y) \tag{3.25}$$

and

$$\Omega^e = \frac{1}{2} \begin{vmatrix} 1 & x_1^e & y_1^e \\ 1 & x_2^e & y_2^e \\ 1 & x_3^e & y_3^e \end{vmatrix} = \frac{1}{2} (b_i^e c_j^e - b_j^e c_i^e) \tag{3.26}$$

$$a_i^e = x_j^e y_k^e - x_k^e y_j^e \tag{3.27}$$

$$b_i^e = y_j^e - y_k^e \tag{3.28}$$

$$c_i^e = x_k^e - x_j^e \tag{3.29}$$

where (x_i^e, y_i^e) is the coordinate of the ith node of the eth element. From (3.25)

$$\frac{\partial N_i^e}{\partial x} = \frac{b_i^e}{2\Omega^e} \tag{3.30}$$

$$\frac{\partial N_i^e}{\partial y} = \frac{c_i^e}{2\Omega^e} \tag{3.31}$$

Substituting these and the formula [5]

$$\iint\limits_{S^e} (N_1^e)^p (N_2^e)^q \, dx dy = 2\Omega^e \frac{p!q!}{(p+q+2)!} \tag{3.32}$$

into (3.23), we find

$$[A^e]_{ij} = \frac{v^e}{4\Omega^e}(b_i^e b_j^e + c_i^e c_j^e) - k_o^2 u^e \frac{\Omega^e}{12}(1 + \delta_{ij}) \tag{3.33}$$

where

$$\delta_{ij} = \begin{cases} 1 & \text{if } i = j \\ 0 & \text{otherwise} \end{cases} \tag{3.34}$$

In (3.33) we have assumed that u and v (the material constitutive parameters) are constant within each element and are given by u^e and v^e, respectively. By summing over all elements as implied by (3.14), we may write the overall system in block form as

$$\begin{bmatrix} A_{aa} & A_{ab} & 0 & 0 \\ A_{ba} & A_{bb} & A_{bI} & 0 \\ 0 & A_{Ib} & A_{II} & A_{Id} \\ 0 & 0 & A_{dI} & A_{dd} \end{bmatrix} \begin{bmatrix} \phi_a \\ \phi_b \\ \phi_I \\ \phi_d \end{bmatrix} = \begin{bmatrix} b_a \\ 0 \\ 0 \\ 0 \end{bmatrix} \tag{3.35}$$

In this, the values of the elements in the submatrix A_{pq} are the contributions associated with the nodes in group p which are connected directly to the nodes in group q.

One can easily show that the line integral contribution (3.24) of those elements vanishes everywhere, unless the element has a side in common with Γ_a. As a result, b^e contributes only from the boundary Γ_a of the finite element region, as indicated by the presence of the vector b_a in (3.35). Without *a priori* knowledge of the total field on that boundary, b^a cannot be determined. We may, however, provide the appropriate condition on this boundary by utilizing the integral equation (3.9). This amounts to replacing the first block-row of the matrix (associated with ϕ_a on Γ_a) with a discrete form of this integral equation.

3.2.3 Evaluation of Boundary Integral

The boundary integral in (3.9) may be written as a summation of four integrals, one for each side of the contour Γ_c as

$$
\begin{aligned}
\phi(\overline{p}) = \phi^{inc}(\overline{p}) &- \int_{\Gamma_{c_1}} \left[G(\overline{p},\overline{p}')\frac{\partial}{\partial n_y}\phi(\overline{p}') - \phi(\overline{p}')\frac{\partial}{\partial y'}G(\overline{p},\overline{p}') \right] dl_{c_1} \\
&- \int_{\Gamma_{c_2}} \left[G(\overline{p},\overline{p}')\frac{\partial}{\partial n_x}\phi(\overline{p}') + \phi(\overline{p}')\frac{\partial}{\partial x'}G(\overline{p},\overline{p}') \right] dl_{c_2} \\
&- \int_{\Gamma_{c_3}} \left[G(\overline{p},\overline{p}')\frac{\partial}{\partial n_y}\phi(\overline{p}') + \phi(\overline{p}')\frac{\partial}{\partial y'}G(\overline{p},\overline{p}') \right] dl_{c_3} \\
&- \int_{\Gamma_{c_4}} \left[G(\overline{p},\overline{p}')\frac{\partial}{\partial n_x}\phi(\overline{p}') - \phi(\overline{p}')\frac{\partial}{\partial x'}G(\overline{p},\overline{p}') \right] dl_{c_4}
\end{aligned} \tag{3.36}
$$

where the derivatives along the x and y directions, denoted by $\frac{\partial}{\partial n_x}$ and $\frac{\partial}{\partial n_y}$, respectively, have been left in this form for the later convenience of determining them numerically. More explicitly, we have

$$
\phi(x, y_{a_1}) = \phi^{inc}(x, y_{a_1})
$$

$$- \int_{\Gamma_{c_1}} \left[G(x - x', y_{a_3}, y_{c_1}) \frac{\partial}{\partial n_y} \phi(x', y_{c_1}) - \phi(x', y_{c_1}) \frac{\partial}{\partial y'} G(x - x', y_{a_3}, y_{c_1}) \right] dx'$$

$$- \int_{\Gamma_{c_2}} \left[G(x, x_{c_2}, y_{a_3}, y') \frac{\partial}{\partial n_x} \phi(x_{c_2}, y') + \phi(x_{c_2}, y') \frac{\partial}{\partial x'} G(x, x_{c_2}, y_{a_3}, y') \right] dy'$$

$$- \int_{\Gamma_{c_3}} \left[G(x - x', y_{a_3}, y_{c_3}) \frac{\partial}{\partial n_y} \phi(x', y_{c_3}) + \phi(x', y_{c_3}) \frac{\partial}{\partial y'} G(x - x', y_{a_3}, y_{c_3}) \right] dx'$$

$$- \int_{\Gamma_{c_4}} \left[G(x, x_{c_4}, y_{a_3}, y') \frac{\partial}{\partial n_x} \phi(x_{c_4}, y') - \phi(x_{c_4}, y') \frac{\partial}{\partial x'} G(x, x_{c_4}, y_{a_3}, y') \right] dy'$$

$$(3.37)$$

and

$$\phi(x_{a_{\frac{2}{4}}}, y) = \phi^{inc}(x_{a_{\frac{2}{4}}}, y)$$

$$- \int_{\Gamma_{c_1}} \left[G(x_{a_{\frac{2}{4}}}, x', y, y_{c_1}) \frac{\partial}{\partial n_y} \phi(x', y_{c_1}) - \phi(x', y_{c_1}) \frac{\partial}{\partial y'} G(x_{a_{\frac{2}{4}}}, x', y, y_{c_1}) \right] dx'$$

$$- \int_{\Gamma_{c_2}} \left[G(x_{a_{\frac{2}{4}}}, x_{c_2}, y - y') \frac{\partial}{\partial n_x} \phi(x_{c_2}, y') + \phi(x_{c_2}, y') \frac{\partial}{\partial x'} G(x_{a_{\frac{2}{4}}}, x_{c_2}, y - y') \right] dy'$$

$$- \int_{\Gamma_{c_3}} \left[G(x_{a_{\frac{2}{4}}}, x', y, y_{c_3}) \frac{\partial}{\partial n_y} \phi(x', y_{c_3}) + \phi(x', y_{c_3}) \frac{\partial}{\partial y'} G(x_{a_{\frac{2}{4}}}, x', y, y_{c_3}) \right] dx'$$

$$- \int_{\Gamma_{c_4}} \left[G(x_{a_{\frac{2}{4}}}, x_{c_4}, y - y') \frac{\partial}{\partial n_x} \phi(x_{c_4}, y') - \phi(x_{c_4}, y') \frac{\partial}{\partial x'} G(x_{a_{\frac{2}{4}}}, x_{c_4}, y - y') \right] dy'$$

$$(3.38)$$

where the first subscript on x or y refers to the contour (a, b or c), and the second refers to the contour number (see Fig. 3.2 and Table 3.1). It is noted that the arguments of the Green's functions have been modified to imply a convolution when appropriate, and this representation will be used throughout.

The normal derivatives of ϕ may be evaluated via the central difference formulas

$$\frac{\partial}{\partial n_x} \phi(x_c, y') = \frac{1}{\Delta} [\phi(x_a, y') - \phi(x_b, y')] + O(\Delta^2) \qquad (3.39)$$

$$\frac{\partial}{\partial n_y} \phi(x', y_c) = \frac{1}{\Delta} [\phi(x', y_a) - \phi(x', y_b)] + O(\Delta^2) \qquad (3.40)$$

where Δ is the displacement of Γ_a from Γ_b (Δ is usually less than one tenth of a

wavelength). Substituting (3.39) and (3.40) into (3.37) and (3.38), we obtain

$$\phi(x, y_{a_{\frac{1}{3}}}) = \phi^{inc}(x, y_{a_{\frac{1}{3}}})$$

$$- \int_{\Gamma_{c_1}} \left[K_y^- G(x - x', y_{a_{\frac{1}{3}}}, y_{c_1}) \phi(x', y_{a_1}) - K_y^+ G(x - x', y_{a_{\frac{1}{3}}}, y_{c_1}) \phi(x', y_{b_1}) \right] dx'$$

$$- \int_{\Gamma_{c_2}} \left[K_x^+ G(x, x_{c_2}, y_{a_{\frac{1}{3}}}, y') \phi(x_{a_2}, y') - K_x^- G(x, x_{c_2}, y_{a_{\frac{1}{3}}}, y') \phi(x_{b_2}, y') \right] dy'$$

$$- \int_{\Gamma_{c_3}} \left[K_y^+ G(x - x', y_{a_{\frac{1}{3}}}, y_{c_3}) \phi(x', y_{a_3}) - K_y^- G(x - x', y_{a_{\frac{1}{3}}}, y_{c_3}) \phi(x', y_{b_3}) \right] dx'$$

$$- \int_{\Gamma_{c_4}} \left[K_x^- G(x, x_{c_4}, y_{a_{\frac{1}{3}}}, y') \phi(x_{a_4}, y') - K_x^+ G(x, x_{c_4}, y_{a_{\frac{1}{3}}}, y') \phi(x_{b_4}, y') \right] dy'$$

$$(3.41)$$

and

$$\phi(x_{a_{\frac{2}{4}}}, y) = \phi^{inc}(x_{a_{\frac{2}{4}}}, y)$$

$$- \int_{\Gamma_{c_1}} \left[K_y^- G(x_{a_{\frac{2}{4}}}, x', y, y_{c_1}) \phi(x', y_{a_1}) - K_y^+ G(x_{a_{\frac{2}{4}}}, x', y, y_{c_1}) \phi(x', y_{b_1}) \right] dx'$$

$$- \int_{\Gamma_{c_2}} \left[K_x^+ G(x_{a_{\frac{2}{4}}}, x_{c_2}, y - y') \phi(x_{a_2}, y') - K_x^- G(x_{a_{\frac{2}{4}}}, x_{c_2}, y - y') \phi(x_{b_2}, y') \right] dy'$$

$$- \int_{\Gamma_{c_3}} \left[K_y^+ G(x_{a_{\frac{2}{4}}}, x', y, y_{c_3}) \phi(x', y_{a_3}) - K_y^- G(x_{a_{\frac{2}{4}}}, x', y, y_{c_3}) \phi(x', y_{b_3}) \right] dx'$$

$$- \int_{\Gamma_{c_4}} \left[K_x^- G(x_{a_{\frac{2}{4}}}, x_{c_4}, y - y') \phi(x_{a_4}, y') - K_x^+ G(x_{a_{\frac{2}{4}}}, x_{c_4}, y - y') \phi(x_{b_4}, y') \right] dy'$$

$$(3.42)$$

in which

$$K_x^\pm = \frac{1}{\Delta} \pm \frac{1}{2} \frac{\partial}{\partial x'} \tag{3.43}$$

$$K_y^\pm = \frac{1}{\Delta} \pm \frac{1}{2} \frac{\partial}{\partial y'} \tag{3.44}$$

Assuming a pulse basis expansion for the nodal fields (i.e., piecewise constant functions centered at nodes on contours Γ_a and Γ_b), a midpoint integration may be performed for the evaluation of the integrals in (3.41) and (3.42), to obtain

$$\phi(x_i, y_{a_{\frac{1}{3}}}) = \phi^{inc}(x_i, y_{a_{\frac{1}{3}}})$$

$$- \Delta \sum_{j=1}^{N_x} \left[K_y^- G(x_i - x_j, y_{a_3}, y_{c_1}) \phi(x_j, y_{a_1}) - K_y^+ G(x_i - x_j, y_{a_3}, y_{c_1}) \phi(x_j, y_{b_1}) \right]$$

$$- \Delta \sum_{j=1}^{N_y} \left[K_x^+ G(x_i, x_{c_2}, y_{a_3}, y_j) \phi(x_{a_2}, y_j) - K_x^- G(x_i, x_{c_2}, y_{a_3}, y_j) \phi(x_{b_2}, y_j) \right]$$

$$- \Delta \sum_{j=1}^{N_x} \left[K_y^+ G(x_i - x_j, y_{a_3}, y_{c_3}) \phi(x_j, y_{a_3}) - K_y^- G(x_i - x_j, y_{a_3}, y_{c_3}) \phi(x_j, y_{b_3}) \right]$$

$$- \Delta \sum_{j=1}^{N_y} \left[K_x^- G(x_i, x_{c_4}, y_{a_3}, y_j) \phi(x_{a_4}, y_j) - K_x^+ G(x_i, x_{c_4}, y_{a_3}, y_j) \phi(x_{b_4}, y_j) \right]$$

$$(3.45)$$

and

$$\phi(x_{a_2}, y_i) = \phi^{inc}(x_{a_2}, y_i)$$
$$\phantom{\phi(x_{a_2}, y_i) =} - \Delta \sum_{j=1}^{N_y} \left[K_y^- G(x_{a_2}, x_j, y_i, y_{c_1}) \phi(x_j, y_{a_1}) - K_y^+ G(x_{a_2}, x_j, y_i, y_{c_1}) \phi(x_j, y_{b_1}) \right]$$

$$\phantom{\phi(x_{a_2}, y_i) =} - \Delta \sum_{j=1}^{N_x} \left[K_x^+ G(x_{a_2}, x_{c_2}, y_i - y_j) \phi(x_{a_2}, y_j) - K_x^- G(x_{a_2}, x_{c_2}, y_i - y_j) \phi(x_{b_2}, y_j) \right]$$

$$\phantom{\phi(x_{a_2}, y_i) =} - \Delta \sum_{j=1}^{N_y} \left[K_y^+ G(x_{a_2}, x_j, y_i, y_{c_3}) \phi(x_j, y_{a_3}) - K_y^- G(x_{a_2}, x_j, y_i, y_{c_3}) \phi(x_j, y_{b_3}) \right]$$

$$\phantom{\phi(x_{a_2}, y_i) =} - \Delta \sum_{j=1}^{N_x} \left[K_x^- G(x_{a_2}, x_{c_4}, y_i - y_j) \phi(x_{a_4}, y_j) - K_x^+ G(x_{a_2}, x_{c_4}, y_i - y_j) \phi(x_{b_4}, y_j) \right]$$

$$(3.46)$$

In these x_i and y_i denote the ith matching/testing points corresponding to the nodal locations on Γ_a, while x_j and y_j denote locations on Γ_b. We recognize some of the terms in (3.45) and (3.46) as discrete convolutions amenable to numerical evaluation via FFT. The subsystem (3.45) and (3.46) may be written more concisely as

$$\begin{bmatrix} \phi_{a_1} \\ \phi_{a_2} \\ \phi_{a_3} \\ \phi_{a_4} \end{bmatrix} = \begin{bmatrix} \phi_{a_1}^{inc} \\ \phi_{a_2}^{inc} \\ \phi_{a_3}^{inc} \\ \phi_{a_4}^{inc} \end{bmatrix} - \begin{bmatrix} S_{a_1 b_1}^- & T_{a_1 b_2}^+ & S_{a_1 b_3}^+ R_x & T_{a_1 b_4}^- \\ T_{a_2 b_1}^- & S_{a_2 b_2}^+ & T_{a_2 b_3}^+ & S_{a_2 b_4}^- R_y \\ S_{a_3 b_1}^- R_x & T_{a_3 b_2}^+ & S_{a_3 b_3}^+ & T_{a_3 b_4}^- \\ T_{a_4 b_1}^- & S_{a_4 b_2}^+ R_y & T_{a_4 b_3}^+ & S_{a_4 b_4}^- \end{bmatrix} \begin{bmatrix} \phi_{a_1} \\ \phi_{a_2} \\ \phi_{a_3} \\ \phi_{a_4} \end{bmatrix}$$

$$+ \begin{bmatrix} S^+_{a_1b_1} & T^-_{a_1b_2} & S^-_{a_1b_3}R_x & T^+_{a_1b_4} \\ T^+_{a_2b_1} & S^-_{a_2b_2} & T^-_{a_2b_3} & S^+_{a_2b_4}R_y \\ S^+_{a_3b_1}R_x & T^-_{a_3b_2} & S^-_{a_3b_3} & T^+_{a_3b_4} \\ T^+_{a_4b_1} & S^-_{a_4b_2}R_y & T^-_{a_4b_3} & S^+_{a_4b_4} \end{bmatrix} \begin{bmatrix} \phi'_{b_1} \\ \phi'_{b_2} \\ \phi'_{b_3} \\ \phi'_{b_4} \end{bmatrix}$$

$$(3.47)$$

with the various parameters to be given explicitly later. The matrices $R_{x,y}$ simply reverse the order of the unknown vector so that the convolutions may be performed properly. This is required solely because of the employed counterclockwise nodal numbering scheme.

Since

$$\left(\phi'_{b_i} \right)_{\text{last}} = \left(\phi'_{b_j} \right)_{\text{first}} \begin{cases} i = 1, 2, 3, 4 \\ j = 2, 3, 4, 1 \end{cases} \tag{3.48}$$

the vector

$$\begin{bmatrix} \phi'_{b_1} & \phi'_{b_2} & \phi'_{b_3} & \phi'_{b_4} \end{bmatrix}^T \tag{3.49}$$

can be related to the actual unknowns on the contour Γ_b via a transformation D_b as

$$\phi'_b = D_b \phi_b \tag{3.50}$$

and (3.47) may then be written as

$$(I + L_{aa})\phi_a - L_{ab}D_b\phi_b = \phi^{inc}_a \tag{3.51}$$

or

$$\begin{bmatrix} A^{BI} \end{bmatrix} \begin{bmatrix} \phi_a \\ \phi_b \end{bmatrix} = \phi^{inc}_a \tag{3.52}$$

where

$$I + L_{aa} = \begin{bmatrix} I + S^-_{a_1b_1} & T^+_{a_1b_2} & S^+_{a_1b_3}R_x & T^-_{a_1b_4} \\ T^-_{a_2b_1} & I + S^+_{a_2b_2} & T^+_{a_2b_3} & S^-_{a_2b_4}R_y \\ S^-_{a_3b_1}R_x & T^+_{a_3b_2} & I + S^+_{a_3b_3} & T^-_{a_3b_4} \\ T^-_{a_4b_1} & S^+_{a_4b_2}R_y & T^+_{a_4b_3} & I + S^-_{a_4b_4} \end{bmatrix} \tag{3.53}$$

and

$$L_{ab} = \begin{bmatrix} S^+_{a_1b_1} & T^-_{a_1b_2} & S^-_{a_1b_3}R_x & T^+_{a_1b_4} \\ T^+_{a_2b_1} & S^-_{a_2b_2} & T^-_{a_2b_3} & S^+_{a_2b_4}R_y \\ S^+_{a_3b_1}R_x & T^-_{a_3b_2} & S^-_{a_3b_3} & T^+_{a_3b_4} \\ T^+_{a_4b_1} & S^-_{a_4b_2}R_y & T^-_{a_4b_3} & S^+_{a_4b_4} \end{bmatrix} \tag{3.54}$$

After replacing the first block row of (3.35) with (3.51), the complete system may be finally written as

$$\begin{bmatrix} I + L_{aa} & -L_{ab}D_b & 0 & 0 \\ A_{ba} & A_{bb} & A_{bI} & 0 \\ 0 & A_{Ib} & A_{II} & A_{Id} \\ 0 & 0 & A_{dI} & A_{dd} \end{bmatrix} \begin{bmatrix} \phi_a \\ \phi_b \\ \phi_I \\ \phi_d \end{bmatrix} = \begin{bmatrix} \phi_a^{inc} \\ 0 \\ 0 \\ 0 \end{bmatrix} \tag{3.55}$$

to be solved via the CG algorithm.

The elements of A^{BI} defined above may be evaluated via the discrete Fourier transform. Specifically, we have

$$S^\pm_{a_1b_{1_3}}\phi_{b_{1_3}} = DFT^{-1}\left\{DFT[G(x,y_{a_1},y_{b_{1_3}}) \pm G_y(x,y_{a_1},y_{b_{1_3}})]DFT[\phi_{b_{1_3}}]\right\} \tag{3.56}$$

$$S^\pm_{a_3b_{1_3}}\phi_{b_{1_3}} = DFT^{-1}\left\{DFT[G(x,y_{a_3},y_{b_{1_3}}) \pm G_y(x,y_{a_3},y_{b_{1_3}})]DFT[\phi_{b_{1_3}}]\right\} \tag{3.57}$$

$$S^\pm_{a_2b_{2_4}}\phi_{b_{2_4}} = DFT^{-1}\left\{DFT[G(x_{a_2},x_{b_{2_4}},y) \pm G_x(x_{a_2},x_{b_{2_4}},y)]DFT[\phi_{b_{2_4}}]\right\} \tag{3.58}$$

$$S^{\pm}_{a_4 b_2} \phi_{b_2} = DFT^{-1} \left\{ DFT[G(x_{a_4}, x_{b_2}, y) \pm G_x(x_{a_4}, x_{b_2}, y)] DFT[\phi_{b_2}] \right\} \quad (3.59)$$

in which DFT denotes the discrete Fourier transform operator. Also

$$G(x, x', y, y') = \frac{-j}{4} H_o^{(2)}(k_o|\rho - \rho'|) = \frac{-j}{4} H_o^{(2)}\left(k_o\sqrt{(x - x')^2 + (y - y')^2}\right) \quad (3.60)$$

$$G_x(x, x', y, y') = \frac{\Delta}{2} \frac{\partial}{\partial x'} G(x, x', y, y')$$

$$= -\frac{j}{8} \Delta k_o \frac{H_1^{(2)}\left(k_o\sqrt{(x - x')^2 + (y - y')^2}\right)}{\sqrt{(x - x')^2 + (y - y')^2}} (x - x') \quad (3.61)$$

$$G_y(x, x', y, y') = \frac{\Delta}{2} \frac{\partial}{\partial y'} G(x, x', y, y')$$

$$= -\frac{j}{8} \Delta k_o \frac{H_1^{(2)}\left(k_o\sqrt{(x - x')^2 + (y - y')^2}\right)}{\sqrt{(x - x')^2 + (y - y')^2}} (y - y') \quad (3.62)$$

Special cases of the convolution operators for the chosen mesh are given as

$$G_x(x_{a_2}, x_{b_2}, y - y') =$$

$$\mp \frac{j}{8} k_o \frac{H_1^{(2)}\left(k_o\sqrt{(x_{a_2} - x_{b_2} + (y - y')^2)^2}\right)}{\sqrt{(x_{a_2} - x_{b_2})^2 + (y - y')^2}} |x_{a_2} - x_{b_2}| \Delta \quad \left\{ \begin{array}{c} x_{a_4} \\ x_{a_2} \end{array} \right. \quad (3.63)$$

$$G_y(x - x', y_{a_1}, y_{b_1}) =$$

$$\mp \frac{j}{8} k_o \frac{H_1^{(2)}\left(k_o\sqrt{(x - x')^2 + (y_{a_1} - y_{b_1})^2}\right)}{\sqrt{(x - x')^2 + (y_{a_1} - y_{b_1})^2}} |y_{a_1} - y_{b_1}| \Delta \quad \left\{ \begin{array}{c} y_{a_1} \\ y_{a_3} \end{array} \right. \quad (3.64)$$

and the corresponding expressions for G are implied by the arguments in the previous two equations. Additionally, the upper coordinate in the braces corresponds to the upper sign and likewise for the lower one.

The cross-term element submatrices are given by

$$\left[T^{\pm}_{a_1 b_2} \right]_{ij} = G(x_i, x_{b_2}, y_{a_1}, y_j) \pm G_x(x_i, x_{b_2}, y_{a_1}, y_j) \quad (3.65)$$

$$\left[T^{\pm}_{a_2 b_1} \right]_{ij} = G(x_{a_2}, x_j, y_i, y_{b_1}) \pm G_y(x_{a_2}, x_j, y_i, y_{b_1}) \quad (3.66)$$

with

$$G_x(x_i, x_{b_2\atop 4}, y_{a_1\atop 3}, y_j) =$$

$$\mp \frac{j}{8} k_o \frac{H_1^{(2)}\left(k_o\sqrt{(x_i - x_{b_2\atop 4})^2 + (y_{a_1\atop 3} - y_j)^2}\right)}{\sqrt{(x_i - x_{b_2\atop 4})^2 + (y_{a_1\atop 3} - y_j)^2}} |x_i - x_{b_2\atop 4}|\Delta \quad \begin{cases} x_{b_2} \\ x_{b_4} \end{cases} \quad (3.67)$$

and

$$G_y(x_{a_2\atop 4}, x_j, y_i, y_{b_1\atop 3}) =$$

$$\mp \frac{j}{8} k_o \frac{H_1^{(2)}\left(k_o\sqrt{(x_{a_2\atop 4} - x_j)^2 + (y_i - y_{b_1\atop 3})^2}\right)}{\sqrt{(x_{a_2\atop 4} - x_j)^2 + (y_i - y_{b_1\atop 3})^2}} |y_i - y_{b_1\atop 3}|\Delta \quad \begin{cases} y_{b_3} \\ y_{b_1} \end{cases} \quad (3.68)$$

where again the corresponding expressions for G are implied by the arguments of the previous two equations. Making the substitutions

$$(x_i - x_{b_2\atop 4})^2 = (i - \tfrac{1}{2})^2 \Delta^2 \tag{3.69}$$

$$(y_{a_1\atop 3} - y_j)^2 = j^2 \Delta^2 \tag{3.70}$$

$$\Longrightarrow \sqrt{(x_i - x_{b_2\atop 4})^2 + (y_{a_1\atop 3} - y_j)^2} = \Delta\sqrt{(i - \tfrac{1}{2})^2 + j^2} \tag{3.71}$$

and

$$(x_{a_2\atop 4} - x_j)^2 = j^2 \Delta^2 \tag{3.72}$$

$$(y_i - y_{b_1\atop 3})^2 = (i - \tfrac{1}{2})^2 \Delta^2 \tag{3.73}$$

$$\Longrightarrow \sqrt{(x_{a_2\atop 4} - x_j)^2 + (y_i - y_{b_1\atop 3})^2} = \Delta\sqrt{j^2 + (i - \tfrac{1}{2})^2} \tag{3.74}$$

we may write G_x and G_y as

$$G_x(x_i, x_{b_2\atop 4}, y_{a_1\atop 3}, y_j) = \mp\frac{j}{8} k_o \frac{H_1^{(2)}\left(k_o\Delta\sqrt{(i - \tfrac{1}{2})^2 + j^2}\right)}{\sqrt{(i - \tfrac{1}{2})^2 + j^2}} |i - \tfrac{1}{2}|\Delta \quad \begin{cases} x_{b_2} \\ x_{b_4} \end{cases} \quad (3.75)$$

$$G_y(x_{a_2\atop 4}, x_j, y_i, y_{b_1\atop 3}) = \mp\frac{j}{8} k_o \frac{H_1^{(2)}\left(k_o\sqrt{j^2 + (i - \tfrac{1}{2})^2}\right)}{\sqrt{j^2 + (i - \tfrac{1}{2})^2}} |i - \tfrac{1}{2}|\Delta \quad \begin{cases} y_{b_3} \\ y_{b_1} \end{cases} \quad (3.76)$$

to be used in the actual implementation of the system. Since each of the above relations are similar, we are required to store only one of them and alter the signs accordingly. It should be noted that, however, this is not the most efficient method of storage. Storing only a few of the cross term values and using an interpolation scheme will reduce the storage considerably. Of course, an interpolation table of (3.75) and (3.76) will lead to a substantial reduction in memory at the expense of some computational efficiency.

Assuming that the positive sign is chosen in equations (3.75) and (3.76), we have

$$T^+_{a_2 b_1 \atop 4} = T^-_{a_2 b_1 \atop 4}$$

$$T^+_{a_1 b_2 \atop 3} = T^+_{a_1 b_2 \atop 3}$$

$$T^+_{a_2 b_3 \atop 4} = T^+_{a_2 b_3 \atop 4}$$

$$T^+_{a_1 b_4 \atop 3} = T^-_{a_1 b_4 \atop 3}$$

$$(3.77)$$

Choosing the positive sign for the (3.63) and (3.64), we also find

$$S^+_{a_1 b_1 \atop 3} = S^+_{a_1 b_1 \atop 3}$$

$$S^+_{a_2 b_2 \atop 4} = S^-_{a_2 b_2 \atop 4}$$

$$S^+_{a_3 b_1 \atop 3} = S^-_{a_3 b_1 \atop 3}$$

$$S^+_{a_4 b_2 \atop 4} = S^+_{a_4 b_2 \atop 4}$$

$$(3.78)$$

Thus, the elements of A^{BI} may be written as

$$
I + L_{aa} = \begin{bmatrix}
I + \mathcal{S}^-_{a_1 b_1} & \mathcal{T}^+_{a_1 b_2} & \mathcal{S}^+_{a_1 b_3} R_x & \mathcal{T}^+_{a_1 b_4} \\
\mathcal{T}^+_{a_2 b_1} & I + \mathcal{S}^-_{a_2 b_2} & \mathcal{T}^+_{a_2 b_3} & \mathcal{S}^+_{a_2 b_4} R_y \\
\mathcal{S}^+_{a_3 b_1} R_x & \mathcal{T}^+_{a_3 b_2} & I + \mathcal{S}^-_{a_3 b_3} & \mathcal{T}^+_{a_3 b_4} \\
\mathcal{T}^+_{a_4 b_1} & \mathcal{S}^+_{a_4 b_2} R_y & \mathcal{T}^+_{a_4 b_3} & I + \mathcal{S}^-_{a_4 b_4}
\end{bmatrix}
$$

$$
L_{ab} = \begin{bmatrix}
\mathcal{S}^+_{a_1 b_1} & \mathcal{T}^-_{a_1 b_2} & \mathcal{S}^-_{a_1 b_3} R_x & \mathcal{T}^-_{a_1 b_4} \\
\mathcal{T}^-_{a_2 b_1} & \mathcal{S}^+_{a_2 b_2} & \mathcal{T}^-_{a_2 b_3} & \mathcal{S}^-_{a_2 b_4} R_y \\
\mathcal{S}^-_{a_3 b_1} R_x & \mathcal{T}^-_{a_3 b_2} & \mathcal{S}^+_{a_3 b_3} & \mathcal{T}^-_{a_3 b_4} \\
\mathcal{T}^-_{a_4 b_1} & \mathcal{S}^-_{a_4 b_2} R_y & \mathcal{T}^-_{a_4 b_3} & \mathcal{S}^+_{a_4 b_4}
\end{bmatrix}
$$

$$(3.79)$$

The elements of the adjoint of A^{BI} required in the implementation of the CG algorithm are

$$
(I + L_{aa})^a = \begin{bmatrix}
I + (\mathcal{S}^-_{a_1 b_1})^a & (\mathcal{T}^+_{a_2 b_1})^a & R^T_x(\mathcal{S}^+_{a_3 b_1})^a & (\mathcal{T}^+_{a_4 b_1})^a \\
(\mathcal{T}^+_{a_1 b_2})^a & I + (\mathcal{S}^-_{a_2 b_2})^a & (\mathcal{T}^+_{a_3 b_2})^a & R^T_y(\mathcal{S}^+_{a_4 b_2})^a \\
R^T_x(\mathcal{S}^+_{a_1 b_3})^a & (\mathcal{T}^+_{a_2 b_3})^a & I + (\mathcal{S}^-_{a_3 b_3})^a & (\mathcal{T}^+_{a_4 b_3})^a \\
(\mathcal{T}^+_{a_1 b_4})^a & R^T_y(\mathcal{S}^+_{a_2 b_4})^a & (\mathcal{T}^+_{a_3 b_4})^a & I + (\mathcal{S}^-_{a_4 b_4})^a
\end{bmatrix}
$$

$$
(L_{ab} D_b)^a = \begin{bmatrix} D^T_b \end{bmatrix} \begin{bmatrix}
(\mathcal{S}^+_{a_1 b_1})^a & (\mathcal{T}^-_{a_2 b_1})^a & R^T_x(\mathcal{S}^-_{a_3 b_1})^a & (\mathcal{T}^-_{a_4 b_1})^a \\
(\mathcal{T}^-_{a_1 b_2})^a & (\mathcal{S}^+_{a_2 b_2})^a & (\mathcal{T}^-_{a_3 b_2})^a & R^T_y(\mathcal{S}^-_{a_4 b_2})^a \\
R^T_x(\mathcal{S}^-_{a_1 b_3})^a & (\mathcal{T}^-_{a_2 b_3})^a & (\mathcal{S}^+_{a_3 b_3})^a & (\mathcal{T}^-_{a_4 b_3})^a \\
(\mathcal{T}^-_{a_1 b_4})^a & R^T_y(\mathcal{S}^-_{a_2 b_4})^a & (\mathcal{T}^-_{a_3 b_4})^a & (\mathcal{S}^+_{a_4 b_4})^a
\end{bmatrix}
$$

$$(3.80)$$

3.2.4 A CGFFT Implementation

The conjugate gradient algorithm presented in section 2.3 is employed for solving the FE–BI system (3.55). The required numerical computation of Az and $A^a z$ are

performed by first decomposing the system into a summation of two matrices; one involving operators associated with the boundary integral and another involving the elements of the finite element matrix. Then system matrix-vector products may then be written as

$$\{s\} = \{s\}_{BI} + \{s\}_{FE} \tag{3.81}$$

where

$$\{s\}_{BI} = \begin{bmatrix} I + L_{aa} & L_{ab}D_b & 0 & 0 \\ 0 & 0 & 0 & 0 \\ 0 & 0 & 0 & 0 \\ 0 & 0 & 0 & 0 \end{bmatrix} \begin{bmatrix} z_1 \\ z_2 \\ z_3 \\ z_4 \end{bmatrix} \tag{3.82}$$

and

$$\{s\}_{FE} = \begin{bmatrix} 0 & 0 & 0 & 0 \\ A_{ba} & A_{bb} & A_{bI} & 0 \\ 0 & A_{Ib} & A_{II} & A_{Id} \\ 0 & 0 & A_{dI} & A_{dd} \end{bmatrix} \begin{bmatrix} z_1 \\ z_2 \\ z_3 \\ z_4 \end{bmatrix} \tag{3.83}$$

For the adjoint operations, we have

$$\{s\}_{BI} = \begin{bmatrix} I + L_{aa}^a & 0 & 0 & 0 \\ D_b^T L_{ab}^a & 0 & 0 & 0 \\ 0 & 0 & 0 & 0 \\ 0 & 0 & 0 & 0 \end{bmatrix} \begin{bmatrix} z_1 \\ z_2 \\ z_3 \\ z_4 \end{bmatrix} \tag{3.84}$$

and

$$\{s\}_{FE} = \begin{bmatrix} 0 & A_{ba}^a & 0 & 0 \\ 0 & A_{bb}^a & A_{Ib}^a & 0 \\ 0 & A_{bI}^a & A_{II}^a & A_{dI}^a \\ 0 & 0 & A_{Id}^a & A_{dd}^a \end{bmatrix} \begin{bmatrix} z_1 \\ z_2 \\ z_3 \\ z_4 \end{bmatrix} \tag{3.85}$$

In each case, the operation is performed such that only the resulting vector $\{s\}$ need be stored.

3.3 Computational Considerations

The FE–BI method for rectangular enclosures is efficient in terms of memory usage and computation time, and each of these aspects is discussed in detail below.

3.3.1 Storage Efficiency

The fundamental advantage of this method is the reduction of storage requirements, so that the scattering by electrically large bodies may be evaluated. To show that the low storage requirement of $O(N_g)$ is assured, we refer to Tables 3.3 and 3.4. These contain a list of all major memory consuming variables. A summarized list is also given in Table 3.5. Specifically, Table 3.5 includes the memory requirements pertaining to the finite element matrix (FE), fast Fourier transforms (FT), boundary integral cross terms (Cross) and conjugate gradient variables (CG). N_c is one less than the number of elements connected to a particular node, and a typical value of 5 is used here.

To put the quantities of Table 3.5 in terms of N_g, the total number of nodes, we consider two special geometries. The mesh in Fig. 3.3 corresponds to a penetrable body, while that of Fig. 3.4 corresponds to an impenetrable structure tightly enclosed by the picture frame. Within each special case two extremes are considered; a mesh corresponding to a square object $(N_x = N_y)$ and a long strip $(N_x \gg N_y)$. In each case, N_g is assumed to be large.

Alluding to Table 3.6 the total storage is $O(N_g)$ for the square region, but is somewhere between $O(N_g)$ and $O(N_g^2)$ for the $(N_x \gg N_y)$ case. This is based

		Memory Consumption	
variable	*type*	*count*	*comment*
Mesh			
Xg	R	N_g	X coordinate of global nodes
Yg	R	N_g	Y coordinate of global nodes
Nglob	I	$3N_e$	Node-element connectivity
Pointers			
ABint	I	N_{ab}	Observation and integration points
Pnodes	I	Pnum	Nodes on conducting bodies
dmatl	I	$N_g - N_{ab}$	Element material properties
Finite Element Matrix (FE)			
Ar	C	$\sim (\frac{N_c+1}{2})(N_g - N_a)$	Non-zero values of FE matrix
col	I	$\sim (\frac{N_c+1}{2})(N_g - N_a)$	Column pointer of FE matrix
row	I	$N_g - N_a$	Pointer to rows of FE matrix
Conjugate Gradient (CG)			
Phiz	C	N_g	Unknown vector
CG1	C	N_g	Residual vector
CG2	C	N_g	Search vector
CG3	C	N_g	Temporary vector
q	C	$MAX(N_x, N_y)$	Temporary vector
phiinc	C	N_a	Incident field vector

Table 3.3: List of major memory-consuming variables

Memory Consumption (continued)			
code variable	*type*	*count*	*comment*
Fourier Transforms (FT)			
FTHx1	C	$2N_x$	Fourier transform along x-direction
FTHx2	C	$2N_x$	
FTHx3	C	$2N_x$	
FTHx4	C	$2N_x$	
FTHy1	C	$2N_y$	Fourier transform along y-direction
FTHy2	C	$2N_y$	
FTHy3	C	$2N_y$	
FTHy4	C	$2N_y$	
FT	C	$2\mathrm{MAX}(N_x, N_y)$	FT of unknown sub-vector
WR	R	$2\mathrm{MAX}(N_x, N_y)$	Temporary array
WI	R	$2\mathrm{MAX}(N_x, N_y)$	Temporary array
Cross-Term Matrices (Cross)			
PQp	C	$\sim \mathrm{MAX}(N_x, N_y)$	
PQm	C	$\sim \mathrm{MAX}(N_x, N_y)$	

Legend
R = REAL*4
C = COMPLEX
I = INTEGER*4

Table 3.4: List of major memory-consuming variables (continued)

Major Memory Consumption ($N_x \geq N_y$)		
Item	Type	Count
FE	COMPLEX	$(\frac{N_c+1}{2})[N_g - 2(N_x + N_y)]$
FT	COMPLEX	$12N_x + 8N_y$
Cross	COMPLEX	$2N_x^2$
CG	COMPLEX	$4N_g$

Table 3.5: Summary of major memory consumption

Major Memory Consumption: Penetrable		
Item	$N_x = N_y$	$N_x >> N_y$
FE	$(\frac{N_c+1}{2})(N_g - 4\sqrt{N_g})$	$(\frac{N_c+1}{2})N_g(1 - \frac{2}{N_y+2})$
FT	$20\sqrt{N_g}$	$12N_g/(N_y + 2)$
Cross	$2N_g$	$2(N_g/N_y)^2$
CG	$4N_g$	$4N_g$
total	$\sim 9N_g$	$\sim 2(\frac{N_g}{N_y+2})^2 + 6\frac{N_g}{2+N_y} + 7N_g$

Table 3.6: Summary of major memory consumption: filled mesh
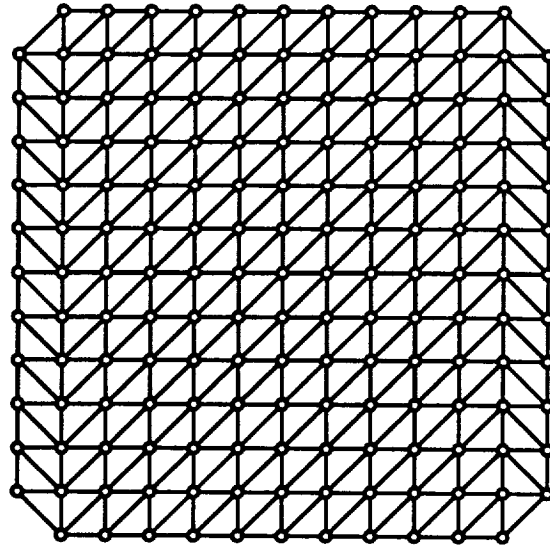
Figure 3.3: Example of the mesh of a penetrable structure
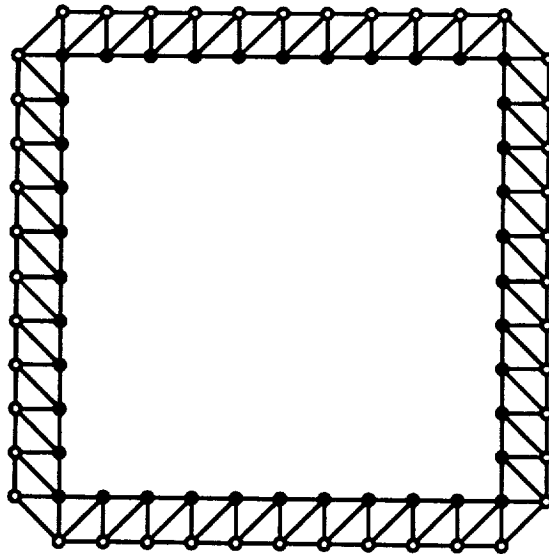
Figure 3.4: Example of the mesh of an impenetrable structure

on the assumption that all cross terms are individually stored, but by using an interpolation table, the $O(N_g)$ memory requirement can be assured regardless of the value of N_x with respect to N_y. In Table 3.7, more dramatic results for the storage of the cross term are listed. In this case, all of the unknowns are on the outer two boundaries, so it appears that the storage is $O(N_g^2)$ for the square case. One must note, however, that the factor multiplying the N_g term may be quite small. The strip case, on the other hand, requires an $O(N_g^2)$ storage. This case would be an unlikely candidate for the use of this method, since that structure would be handled much more efficiently via a direct implementation of the CGFFT method. As noted above, the storage of the cross terms may be brought down to $O(N_g)$ for all cases by using an interpolation table, and this will certainly be necessary in a 3-D implementation.

Major Memory Consumption: Impenetrable		
Item	$N_x = N_y$	$N_x >> N_y$
FE	$(\frac{N_c+1}{2})N_g/2$	$(\frac{N_c+1}{2})N_g/2$
FFT	$5N_g/2$	$3N_g$
Cross	$N_g^2/32$	$N_g^2/8$
CG	$4N_g$	$4N_g$
total	$\sim N_g^2/32 + 8N_g$	$\sim N_g^2/8 + 17N_g/2$

Table 3.7: Summary of major memory consumption: open mesh

3.3.2 Computational Efficiency

Since the primary importance of the FE–BI method is storage reduction, a comparable level of efficiency with alternative methods is a bonus. A method for which a fair comparison may be made is the standard CGFFT. This requires a 2-D FFT, which is slower than using multiple 1-D FFTs for large bodies. We compared the two methods for a specific penetrable scatterer using an Apollo 3500 without code optimization. The pertinent CPU times are compared in Table 3.8. The comparison provides only a relative measure of the speed difference.

3.4 Far Field Computation

The scattered fields may be computed as

$$\phi^s(\overline{p}) = -\oint_{\Gamma_c} \left\{ G(\overline{p},\overline{p}') \left[\frac{\partial}{\partial n'}\phi(\overline{p}') \right] - \phi(\overline{p}') \left[\frac{\partial}{\partial n'}G(\overline{p},\overline{p}') \right] \right\} dl' \qquad (3.86)$$

Body Properties		FE-CGFFT			CGFFT		
Composition	Dimensions	T/I (s)	I	Total	T/I (s)	I	Total
dielectric $\epsilon_r = 4 - j.1$	$2\lambda \times 2\lambda$	8.6	155	1333	170	33	5610

Legend
T/I = time/iteration
I = number of iterations

Table 3.8: A comparision of computation efficiency of the FE-CGFFT with the CGFFT method

Using the discretization scheme developed earlier, we have

$$
\phi^s(x,y) =
$$

$$
- \left\{ \int_{\Gamma_{c_1}} \left[K_y^- G(x,x',y,y_{c_1})\phi(x',y_{a_1}) - K_y^+ G(x,x',y,y_{c_1})\phi(x',y_{b_1}) \right] dx' \right.
$$

$$
+ \int_{\Gamma_{c_2}} \left[K_x^+ G(x,x_{c_2},y,y')\phi(x_{a_2},y') - K_x^- G(x,x_{c_2},y,y')\phi(x_{b_2},y') \right] dy'
$$

$$
+ \int_{\Gamma_{c_3}} \left[K_y^+ G(x,x',y,y_{c_3})\phi(x',y_{a_3}) - K_y^- G(x,x',y,y_{c_3})\phi(x',y_{b_3}) \right] dx'
$$

$$
\left. + \int_{\Gamma_{c_4}} \left[K_x^- G(x,x_{c_4},y,y')\phi(x_{a_4},y') - K_x^+ G(x,x_{c_4},y,y')\phi(x_{b_4},y') \right] dy' \right\}
$$

$$(3.87)$$

where the definitions for $K_x^\pm$ and $K_y^\pm$ are as specified previously. Letting

$$
\beta^x(x,y,y_c) = \frac{1}{\Delta} \int_{x_j-\frac{\Delta}{2}}^{x_j+\frac{\Delta}{2}} G(x,x',y,y_c)dx' \tag{3.88}
$$

$$
\beta^y(x,x_c,y) = \frac{1}{\Delta} \int_{y_j-\frac{\Delta}{2}}^{y_j+\frac{\Delta}{2}} G(x,x_c,y,y')dy' \tag{3.89}
$$

$$\gamma^x(x,y,y_c) = \frac{1}{2}\int_{x_j-\frac{\Delta}{2}}^{x_j+\frac{\Delta}{2}} \frac{\partial}{\partial y'}G(x,x',y,y_c)dx' \tag{3.90}$$

$$\gamma^y(x,x_c,y) = \frac{1}{2}\int_{y_j-\frac{\Delta}{2}}^{y_j+\frac{\Delta}{2}} \frac{\partial}{\partial x'}G(x,x_c,y,y')dy' \tag{3.91}$$

(3.87) becomes

$$\phi^s(x,y) =$$

$$-\left\{\sum_{j=1}^{N_x}\left([\beta^x(x,y,y_{c_1}) - \gamma^x(x,y,y_{c_1})]\{\phi_{a_1}\}_j - [\beta^x(x,y,y_{c_1}) + \gamma^x(x,y,y_{c_1})]\{\phi_{b_1}\}_j\right)\right.$$

$$+ \sum_{j=1}^{N_y}\left([\beta^y(x,x_{c_2},y) + \gamma^y(x,x_{c_2},y)]\{\phi_{a_2}\}_j - [\beta^y(x,x_{c_2},y) - \gamma^y(x,x_{c_2},y)]\{\phi_{b_2}\}_j\right)$$

$$+ \sum_{j=1}^{N_x}\left([\beta^x(x,y,y_{c_3}) + \gamma^x(x,y,y_{c_3})]\{\phi_{a_3}\}_j - [\beta^x(x,y,y_{c_3}) - \gamma^x(x,y,y_{c_3})]\{\phi_{b_3}\}_j\right)$$

$$\left. + \sum_{j=1}^{N_y}\left([\beta^y(x,x_{c_4},y) - \gamma^y(x,x_{c_4},y)]\{\phi_{a_4}\}_j - [\beta^y(x,x_{c_4},y) + \gamma^y(x,x_{c_4},y)]\{\phi_{b_4}\}_j\right)\right\} \tag{3.92}$$

valid for all observation points (x,y). To specialize (3.92) to far zone computations, we must introduce the appropriate asymptotic expansion for the Hankel functions implied in (3.88)-(3.91). In doing so, we have

$$\beta^x(x,y,y_{c_{\frac{1}{3}}}) = jf_o(\rho)f_1(\theta,y_{c_{\frac{1}{3}}})e^{jk_ox_j\cos\theta} \tag{3.93}$$

$$\beta^y(x,x_{c_{\frac{2}{4}}},y) = jf_o(\rho)f_2(\theta,x_{c_{\frac{2}{4}}})e^{jk_oy_j\sin\theta} \tag{3.94}$$

$$\gamma^x(x,y,y_{c_{\frac{1}{3}}}) = -f_o(\rho)f_1(\theta,y_{c_{\frac{1}{3}}})k_o\Delta\sin\theta e^{jk_ox_j\cos\theta} \tag{3.95}$$

$$\gamma^y(x,x_{c_{\frac{2}{4}}},y) = -f_o(\rho)f_2(\theta,x_{c_{\frac{2}{4}}})k_o\Delta\cos\theta e^{jk_oy_j\sin\theta} \tag{3.96}$$

where

$$f_o(\rho) = \frac{1}{4}\sqrt{\frac{2j}{\pi k_o\rho}}e^{-jk_o\rho} \tag{3.97}$$

$$f_1(\theta,y_{c_{\frac{1}{3}}}) = -e^{jk_oy_{c_{\frac{1}{3}}}\sin\theta} \tag{3.98}$$

$$f_2(\theta,x_{c_{\frac{2}{4}}}) = -e^{jk_ox_{c_{\frac{2}{4}}}\cos\theta} \tag{3.99}$$

in which (ρ, θ) imply the usual cylindrical coordinates of the observation point. Substituting expressions (3.93)-(3.96) into (3.92), we obtain

$$
\begin{aligned}
\phi_H^s(x,y) = -f_o(\rho) & \left\{ \sum_{j=1}^{N_x} \left([j + k_o \Delta \sin \theta] \{\phi_{a_1}\}_j - [j - k_o \Delta \sin \theta] \{\phi_{b_1}\}_j \right) f_1(\theta, y_{c_1}) e^{jk_o x_j \cos \theta} \right. \\
& + \sum_{j=1}^{N_y} \left([j - k_o \Delta \cos \theta] \{\phi_{a_2}\}_j - [j + k_o \Delta \cos \theta] \{\phi_{b_2}\}_j \right) f_2(\theta, x_{c_2}) e^{jk_o y_j \sin \theta} \\
& + \sum_{j=1}^{N_x} \left([j - k_o \Delta \sin \theta] \{\phi_{a_3}\}_j - [j + k_o \Delta \sin \theta] \{\phi_{b_3}\}_j \right) f_1(\theta, y_{c_3}) e^{jk_o x_j \cos \theta} \\
& \left. + \sum_{j=1}^{N_y} \left([j + k_o \Delta \cos \theta] \{\phi_{a_4}\}_j - [j - k_o \Delta \cos \theta] \{\phi_{b_4}\}_j \right) f_2(\theta, x_{c_4}) e^{jk_o y_j \sin \theta} \right\}
\end{aligned}
$$

(3.100)

From (3.100) the echowidth becomes

$$
\begin{aligned}
\sigma = \frac{1}{4k_o} & \left| \sum_{j=1}^{N_x} \left([j + k_o \Delta \sin \theta] \{\phi_{a_1}\}_j - [j - k_o \Delta \sin \theta] \{\phi_{b_1}\}_j \right) f_1(\theta, y_{c_1}) e^{jk_o x_j \cos \theta} \right. \\
& + \sum_{j=1}^{N_y} \left([j - k_o \Delta \cos \theta] \{\phi_{a_2}\}_j - [j + k_o \Delta \cos \theta] \{\phi_{b_2}\}_j \right) f_2(\theta, x_{c_2}) e^{jk_o y_j \sin \theta} \\
& + \sum_{j=1}^{N_x} \left([j - k_o \Delta \sin \theta] \{\phi_{a_3}\}_j - [j + k_o \Delta \sin \theta] \{\phi_{b_3}\}_j \right) f_1(\theta, y_{c_3}) e^{jk_o x_j \cos \theta} \\
& \left. + \sum_{j=1}^{N_y} \left([j + k_o \Delta \cos \theta] \{\phi_{a_4}\}_j - [j - k_o \Delta \cos \theta] \{\phi_{b_4}\}_j \right) f_2(\theta, x_{c_4}) e^{jk_o y_j \sin \theta} \right|^2
\end{aligned}
$$

(3.101)

3.5 Code Validation

The scattering patterns from several rectangular structures are presented. The echowidth is computed for each structure and compared to the results of the moment method. The bodies are discretized at a sampling rate of 20 samples/free-space wavelength.

Results are presented for the following cases:

- perfectly conducting bodies (Figs. 3.5 and 3.6)

- partially and fully coated perfectly conducting cylinders (Figs. 3.7 - 3.12)

- composite body (Fig. 3.13)

In each figure, the discretized geometry is shown along with the corresponding results. As seen in all cases, the generated patterns using the FE-CGFFT formulation are agree with the moment method data.

.25 x 2. λ Perfect Conductor (E-pol)
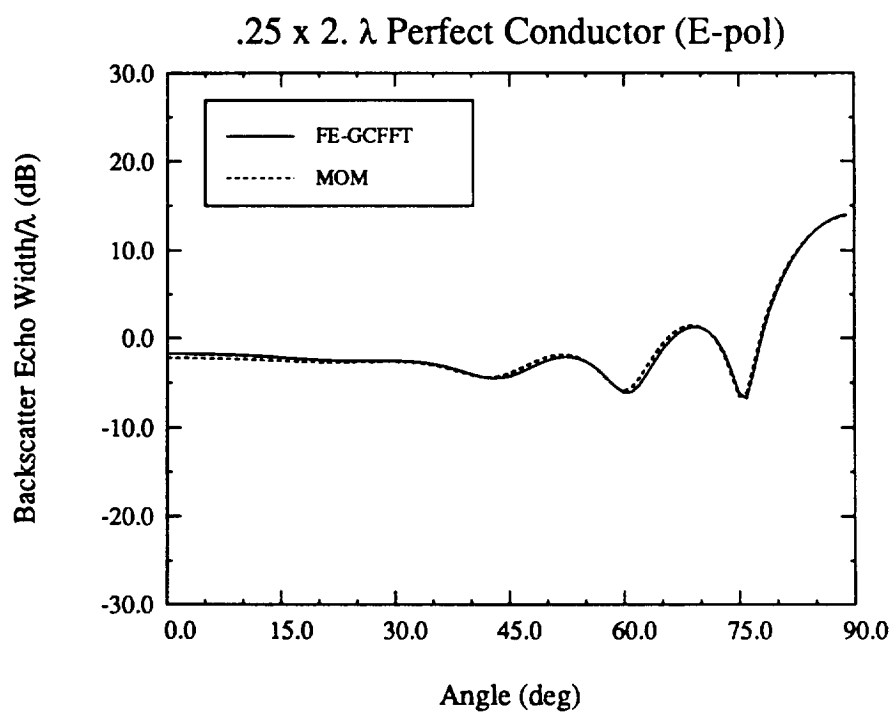
Figure 3.5: E_z backscatter from a .25 × 2λ body
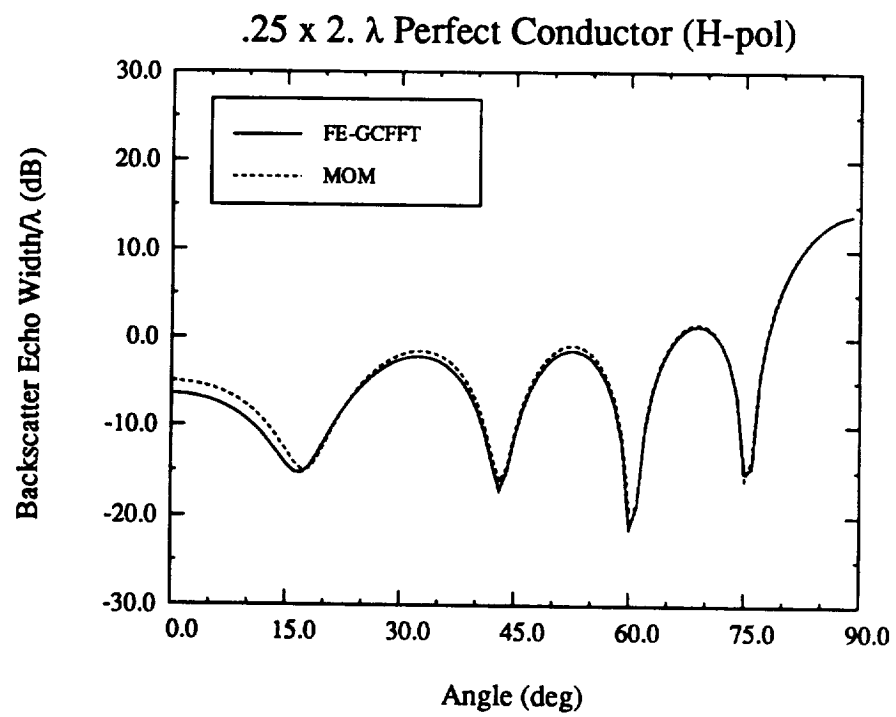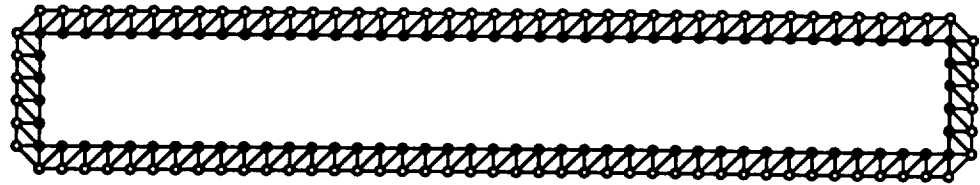
Figure 3.6: H_z backscatter from a .25 × 2λ body

.25 x 1. λ Coated Perfect Conductor (E-pol)
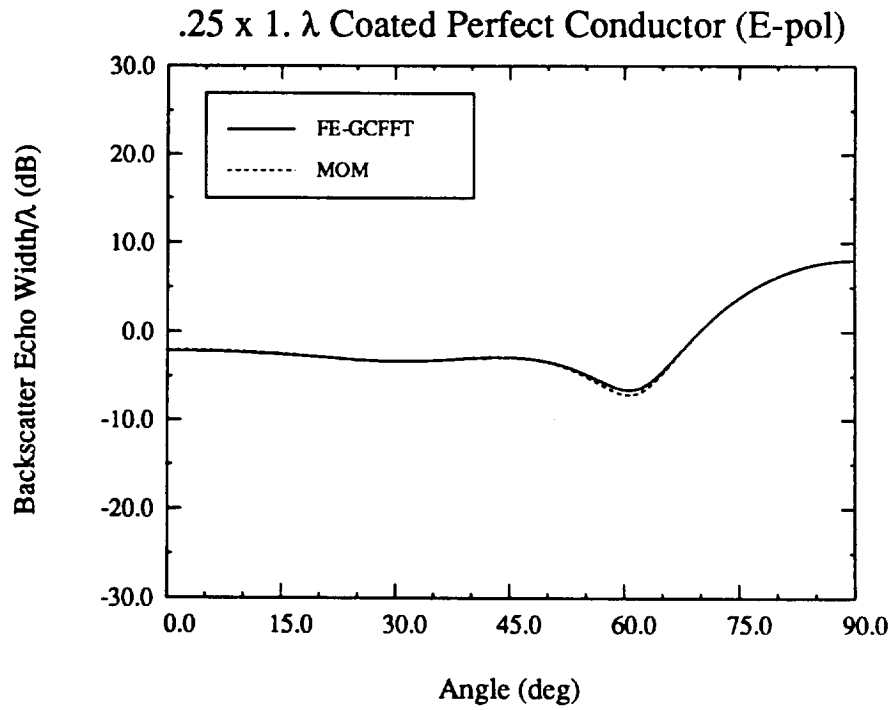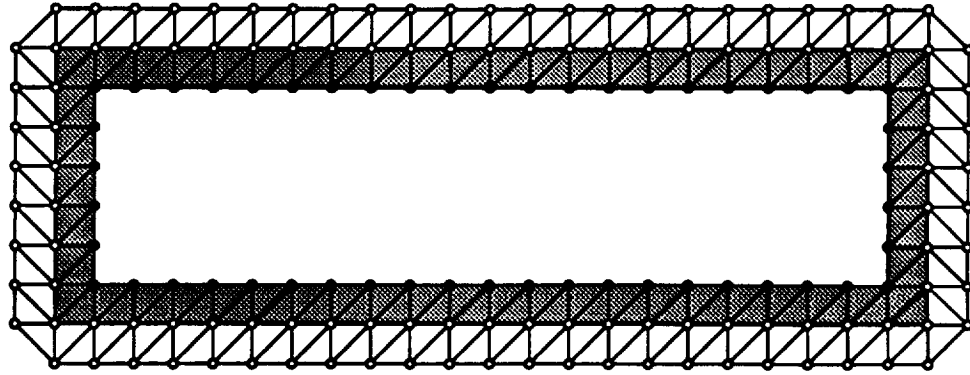
Figure 3.7: E_z backscatter from a .25 × 1λ perfect conductor with a λ/20 thick material coating containing the properties $\epsilon_r = 5. - j.5, \mu_r = 1$
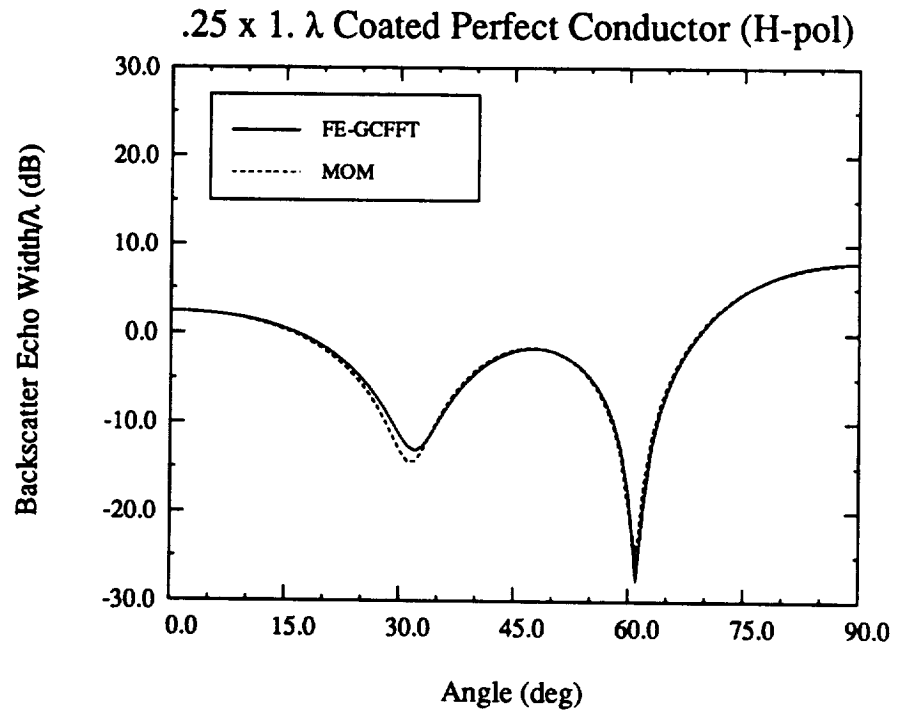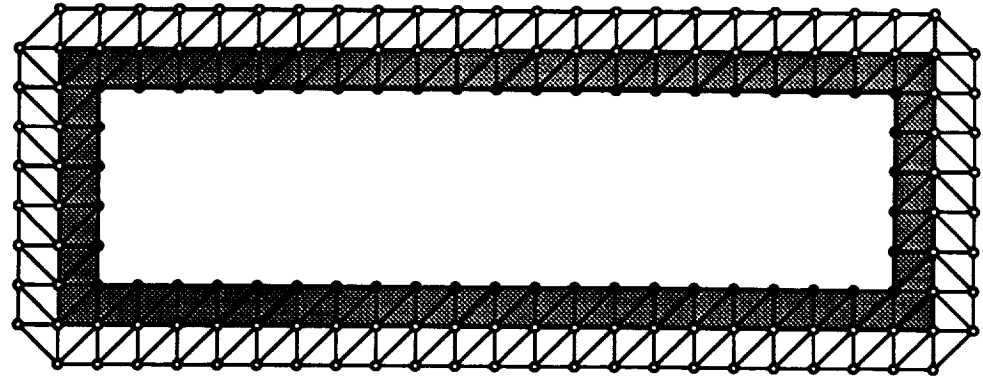
Figure 3.8: H_z backscatter from a .25 × 1λ perfect conductor with a λ/20 thick material coating containing the properties $\epsilon_r = 5. - j.5, \mu_r = 1$
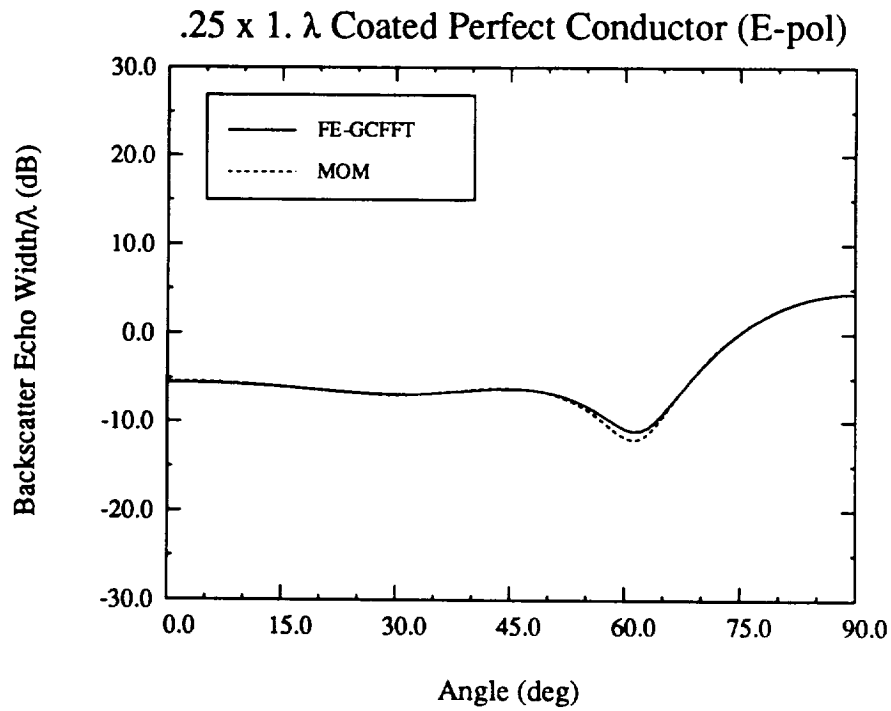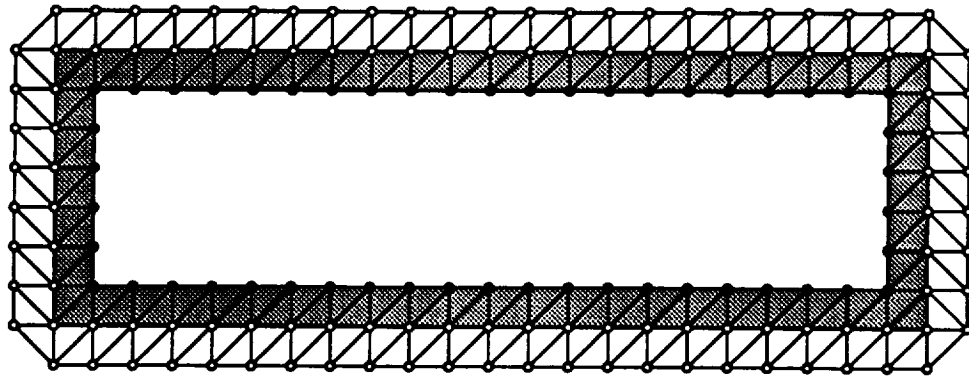
Figure 3.9: E_z backscatter from a $.25 \times 1\lambda$ perfect conductor with a $\lambda/20$ thick material coating containing the properties $\epsilon_r = 5. - j.5, \mu_r = 1.5 - j.5$
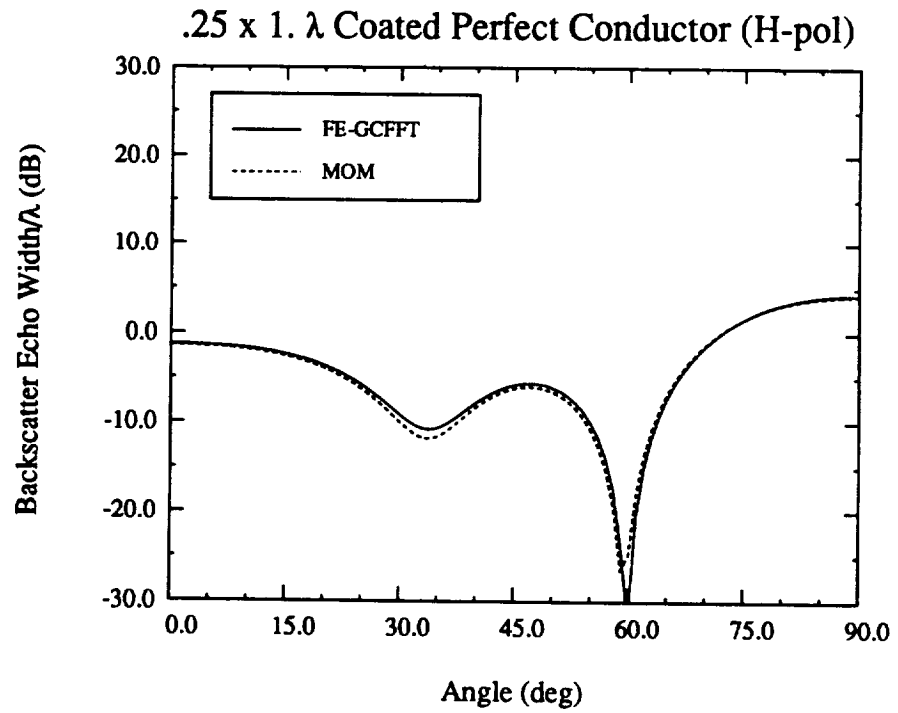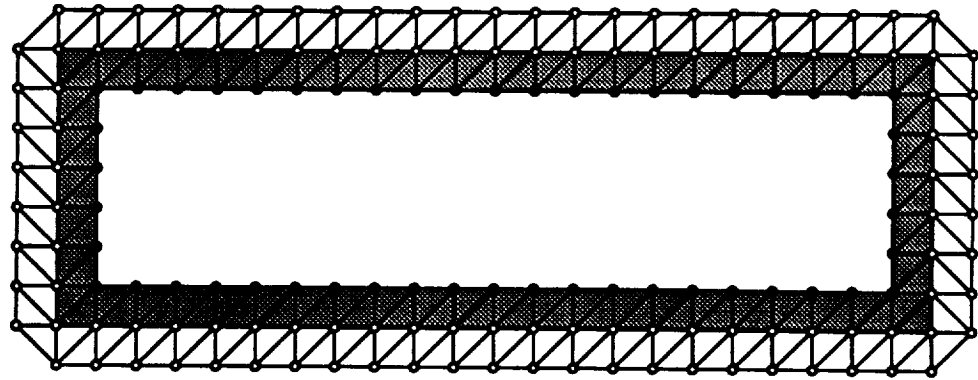
Figure 3.10: H_z backscatter from a .25 × 1λ perfect conductor with a $\lambda/20$ thick material coating containing the properties $\epsilon_r = 5. - j.5, \mu_r = 1.5 - j.5$
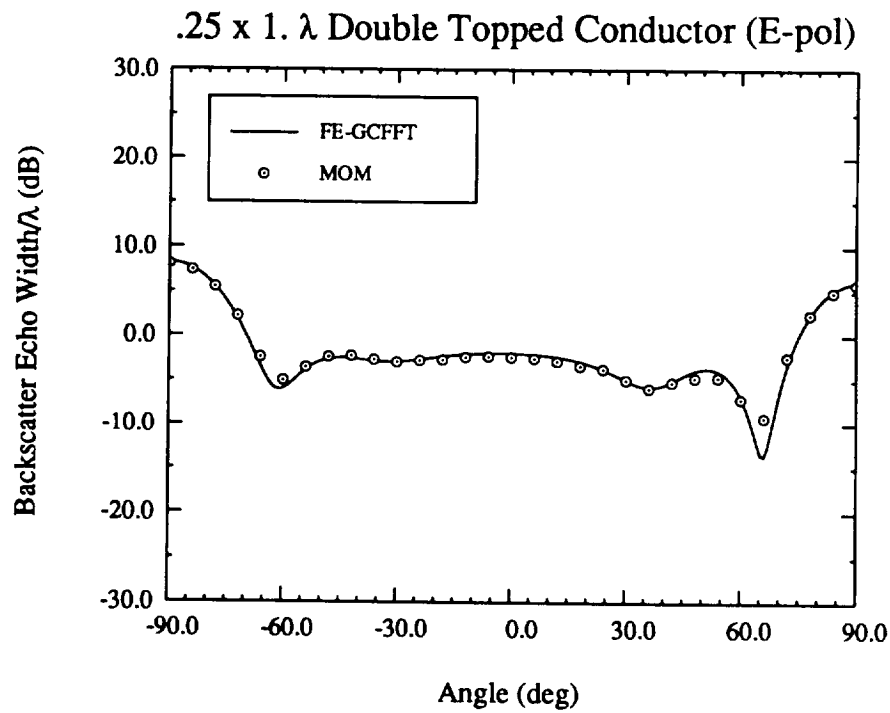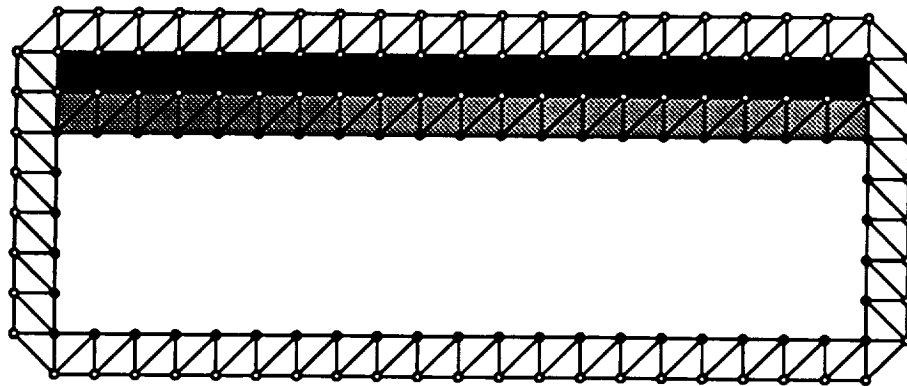
Figure 3.11: E_z backscatter from a $.25 \times 1\lambda$ perfect conductor with two $\lambda/20$ thick top material coatings. The lower layer has the properties $\epsilon_r = 2. - j.5, \mu_r = 1.5 - j.2$, and the upper layer has properties $\epsilon_r = 4. - j.5, \mu_r = 1.5 - j.2$
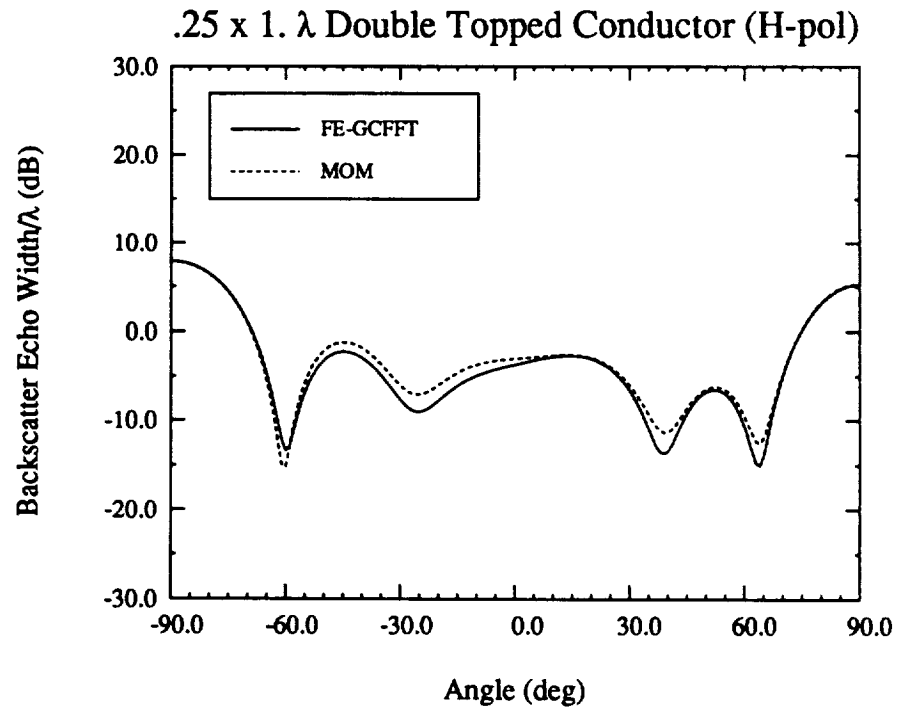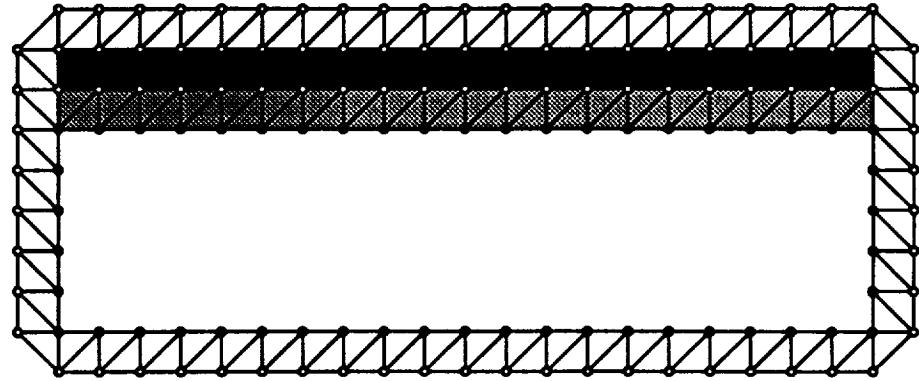
Figure 3.12: H_z backscatter from a .25×1λ perfect conductor with two λ/20 thick top material coatings. The lower layer has the properties $\epsilon_r = 2. - j.5, \mu_r = 1.5 - j.2$, and the upper layer has properties $\epsilon_r = 4. - j.5, \mu_r = 1.5 - j.2$
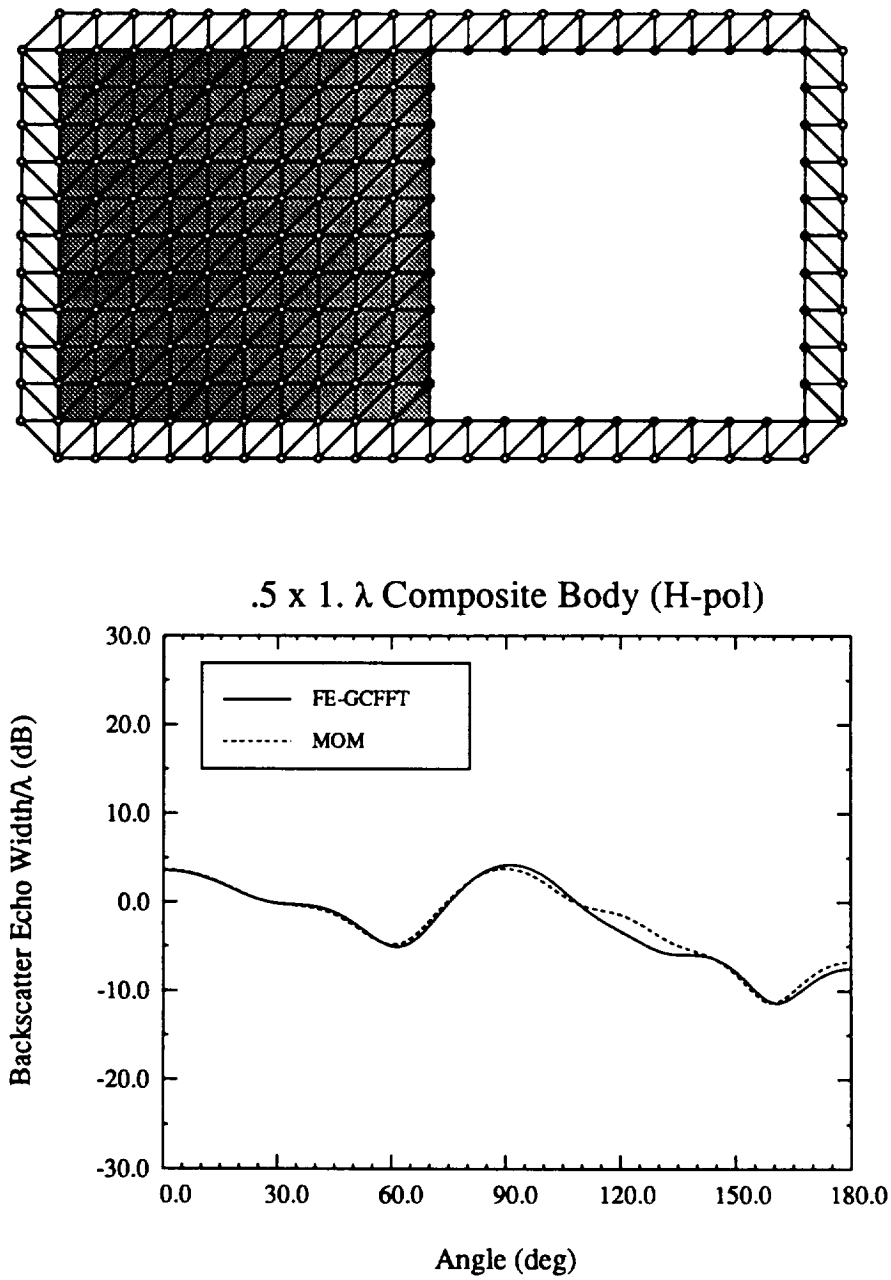
Figure 3.13: H_z scattering from a composite body. Both the perfect conductor and the dielectric body are $\lambda/2$ in each dimension. The material properties are $\epsilon_r = 5. - j.5, \mu_r = 1.5 - j.5$

3.6 Summary

A procedure was developed for computing the scattering by 2-D structures. This procedure combined the boundary integral and finite element methods, and the resulting system was solved via CGFFT. The main advantage of the new approach was a reduction in memory demand to $O(N)$ compared to $O(N^2)$ required with traditional solution techniques. A detailed map of the storage requirements was presented, and the principle memory consuming arrays were discussed. Also, the computational efficiency of the technique was examined and found favorable. To validate the proposed solution approach, several backscatter patterns were presented and compared with results based on traditional solution methods.

CHAPTER IV

A Finite Element – Boundary Integral Method for Two-dimensional Scattering Using Circular and Ogival Termination Boundaries

4.1 Introduction

It is possible to choose other boundaries that result in convolutional integrals, and in this chapter we consider circular and ogival enclosures. Clearly, a circular enclosure would be attractive for circular scatterers whereas an ogival boundary will be more attractive for those structures conforming to this boundary. In the case of the circular boundary the entire integral is convolutional ensuring the $O(N)$ memory demand of the system provided an iterative solver is used. When an ogival enclosure is used the integral becomes convolutional only if the observation and source points are on the same arc, but an efficient storage scheme is again required for the remaining "cross-terms" [1].

In the following sections, the pertinent FE–BI formulations are developed for the circular and ogival boundaries. Results for several circular and ogival structures are presented and shown to be in excellent agreement with that obtained by traditional methods.

---

[1] "cross terms" refer to integrals for which the source and observation points are not on the same arc
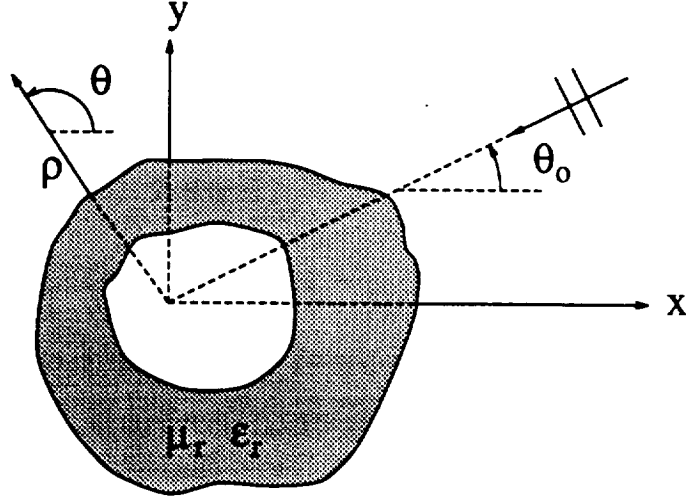
Figure 4.1: Geometry of the scatterer

4.2 Analysis

Consider the plane wave

$$\overline{\phi}^{inc}(\overline{\rho}) = \hat{z}\phi_z^{inc}(\overline{\rho}) = \hat{z}e^{jk_o\rho\cos(\theta-\theta_o)} \tag{4.1}$$

illuminating a composite cylinder as shown in Fig. 4.1 and we are interested in computing the scattered field. For the application of the Finite Element - Boundary Element Method the target is enclosed in a fictitious circular or ogival boundary as shown in Figs. 4.2 and 4.3. Within the boundary Γ_a, the finite element method is used to solve the Helmholtz equation

$$\nabla \cdot [v(\overline{\rho})\nabla\phi(\overline{\rho})] + k_o^2 v(\overline{\rho})\phi(\overline{\rho}) = 0 \tag{4.2}$$

where

$$\phi(\overline{\rho}) = E_z(\overline{\rho}), \quad u(\overline{\rho}) = \frac{1}{\mu_r(\overline{\rho})} \quad v(\overline{\rho}) = \epsilon_r(\overline{\rho}) \tag{4.3}$$

for E-polarization and

$$\phi(\overline{p}) = H_z(\overline{p}), \quad u(\overline{p}) = \frac{1}{\epsilon_r(\overline{p})}, \quad v(\overline{p}) = \mu_r(\overline{p}) \tag{4.4}$$

for H-polarization. The free-space wave number is $k_o = \omega\sqrt{\mu_o\epsilon_o}$ and μ_r and ϵ_r are the relative permeablility and permittivity, respectively. On the boundary Γ_a the Helmholtz integral equation

$$\phi(\overline{p}) = \phi^{inc}(\overline{p}) - \oint_{\Gamma_a} \left\{ G(\overline{p}, \overline{p}_a) \left[\frac{\partial}{\partial n_a} \phi(\overline{p}_a) \right] - \phi(\overline{p}_a) \left[\frac{\partial}{\partial n_a} G(\overline{p}, \overline{p}_a) \right] \right\} dl_a \tag{4.5}$$

provides the required boundary constraint, implicitly satisfying the radiation condition. In (4.5)

$$G(\overline{p}, \overline{p}_a) = -\frac{j}{4} H_o^{(2)}(k_o|\overline{p} - \overline{p}_a|) \tag{4.6}$$

is the 2-D free space Green's function where $H_o^{(2)}(\cdot)$ denotes the zeroth order Hankel function of the second kind. Also, $\frac{\partial}{\partial n_a}$ denotes differentiation with respect to the outward normal, whereas $\overline{p}$ and $\overline{p}_a$ are the usual source and observation points, respectively, and

$$|\overline{p} - \overline{p}_a| = \sqrt{(x - x_a)^2 + (y - y_a)^2} \tag{4.7}$$

4.2.1 Circular Enclosure

Discretization of the Scatterer and Field Quantities

The region enclosed by Γ_a, denoted as R_a, is discretized into N_e finite elements as illustrated in Fig. 4.2. In the figure, ρ_a is the radius of the circle and α_a is the integration angle along this boundary (Further definitions for the finite element mesh are indicated in Table 4.1, while the definitions of the field vectors are indicated in Table 4.2.). We note that nodes along Γ_a are equispaced with angular displacement Δ.
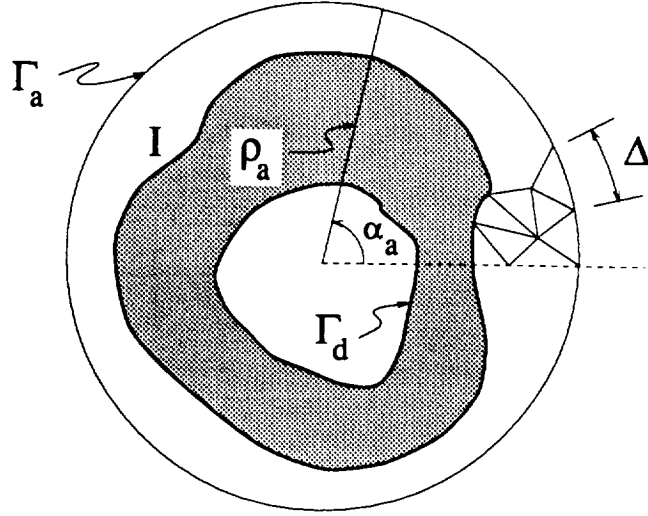
Figure 4.2: Partially discretized body in a circular enclosure

Symbol	Description
N_n	number of nodes in the finite element mesh
N_g	number of unknowns
N_e	number of elements in the finite element mesh
N_a	number of nodes or elements on Γ_a
N_d	number of nodes or elements on Γ_d

Table 4.1: Definition of various quantities associated with the finite element mesh

Symbol	Description
ϕ_a	field at the nodes on Γ_a
ψ_a	normal derivative of the field at the nodes on Γ_a
ϕ_I	field at the nodes region I enclosed by Γ_a and Γ_d
ϕ_d	field at the nodes on Γ_d

Table 4.2: Definition of various field vectors associated with the finite element mesh and its boundary

Derivation of the Finite Element Matrix

The weighted residual expression over each element may be written as [5]

$$\iint_{S^e} R^e W_i^e dS^e = 0 \qquad i = 1, 2, 3 \tag{4.8}$$

where

$$R^e = -\frac{\partial}{\partial x}\left[u(x,y)\frac{\partial}{\partial x}\phi^e(x,y)\right] - \frac{\partial}{\partial y}\left[u(x,y)\frac{\partial}{\partial y}\phi^e(x,y)\right] - k_o^2 v(x,y)\phi^e(x,y) \tag{4.9}$$

In (4.9), W_i^e is the ith weighting function associated with the eth element. Substituting (4.9) into (4.8) and invoking the divergence theorem yields

$$\iint_{S^e}\left\{-u\left[\frac{\partial\phi^e}{\partial x}\frac{\partial W_i^e}{\partial x} + \frac{\partial\phi^e}{\partial y}\frac{\partial W_i^e}{\partial y}\right] + k_0^2 v\phi^e W_i^e\right\} d\Omega^e$$
$$+ \int_{\Gamma^e} W_i^e \psi^e d\Gamma^e = 0 \tag{4.10}$$

where Γ^e denotes the contour enclosing the eth element. Additionally,

$$\psi^e = u^e\frac{\partial\phi^e}{\partial n} \tag{4.11}$$

is zero outside element e. Summing over N_e elements we obtain

$$\sum_{e=1}^{N_e}\iint_{S^e}\left\{-u\left[\frac{\partial\phi^e}{\partial x}\frac{\partial W_i^e}{\partial x} + \frac{\partial\phi^e}{\partial y}\frac{\partial W_i^e}{\partial y}\right] + k_0^2 v\phi^e W_i^e\right\} d\Omega^e$$
$$+ \sum_{s=1}^{N_a}\int_{\Gamma_a^s} W_i^s \psi^s d\Gamma_a^s + \sum_{s=1}^{N_d}\int_{\Gamma_d^s} W_i^s \psi^s d\Gamma_d^s = 0 \tag{4.12}$$

where the summations over s refer to the elements with sides adjacent to the fictitious (Γ_a) and conducting (Γ_d) boundaries.

The integral over the conducting boundary in (4.12) vanishes all cases. This is obvious when no conductor is present. When $\phi = H_z$, the normal derivative of the field is zero on the conductor and the field unknowns on the boundary are allowed to "float" (i.e., they are not fixed to a specific value but are determined by solving the system). Finally, when $\phi = E_z$, imposing the Dirichlet condition after assembling the finite element system results in the elimination of those equations associated with the integral over Γ_d.

Proceeding with the discretization, the field and its derivative within each element may be expanded into a linear combination of shape functions

$$\phi^e = \sum_{j=1}^{3} N_j^e \, \phi_j^e \tag{4.13}$$

$$\psi^e = \sum_{k=1}^{3} N_k^e \, \psi_j^e \tag{4.14}$$

Substituting (4.13) and (4.14) into (4.10) and choosing $W_i^e = N_i^e$ (Galerkin's method), we obtain

$$\sum_{j=1}^{3} a_{ij}^e \phi_j^e - \sum_{k=1}^{3} \sum_{j=1}^{3} b_{ij}^s(k)\psi_j^e = 0 \tag{4.15}$$

where

$$a_{ij}^e = \iint\limits_{S^e} \left\{ u \left[\frac{\partial N_i^e}{\partial x} \frac{\partial N_j^e}{\partial x} + \frac{\partial N_i^e}{\partial y} \frac{\partial N_j^e}{\partial y} \right] - k_0^2 v N_i^e N_j^e \right\} d\Omega^e \tag{4.16}$$

and

$$b_{ij}^e(k) = \int_{\Gamma_a^e} N_j^e N_i^e \, dl^e \tag{4.17}$$

For linear triangular elements, N_i^e are given by

$$N_i^e = \frac{1}{2\Omega^e}(a_i^e + b_i^e x + c_i^e y) \tag{4.18}$$

with

$$\Omega^e = \tfrac{1}{2}(b_i^e c_j^e - b_j^e c_i^e) \tag{4.19}$$

$$a_i^e = x_j^e y_k^e - x_k^e y_j^e \tag{4.20}$$

$$b_i^e = y_j^e - y_k^e \tag{4.21}$$

$$c_i^e = x_k^e - x_j^e \tag{4.22}$$

and (x_i^e, y_i^e) being the coordinates of the ith node of the eth element. From (4.18)

$$\frac{\partial N_i^e}{\partial x} = \frac{b_i^e}{2\Omega^e} \tag{4.23}$$

$$\frac{\partial N_i^e}{\partial y} = \frac{c_i^e}{2\Omega^e} \tag{4.24}$$

Using (4.23), (4.24) and the identity

$$\iint_{S^e} (N_1^e)^p (N_2^e)^q dx dy = 2\Omega^e \frac{p!q!}{(p+q+2)!} \tag{4.25}$$

a_{ij} in (4.16) reduces to

$$a_{ij}^e = \frac{u^e}{4\Omega^e}(b_i^e b_j^e + c_i^e c_j^e) - k_o^2 v^e \frac{\Omega^e}{12}(1 + \delta_{ij}) \tag{4.26}$$

where

$$\delta_{ij} = \begin{cases} 1 & \text{if } i = j \\ 0 & \text{otherwise} \end{cases} \tag{4.27}$$

We note that in deriving (4.26) we have assumed that u and v (the reciprocal of the material constitutive parameters) are constant within each element and are given by u^e and v^e, respectively.

To find an algebraic expression for b_{ik}^s, we may reparametize the integral in (4.17) as

$$b_{ik}^s = \int_{\alpha_1}^{\alpha_1 + \Delta} P_i^s P_k^s r_a d\alpha \tag{4.28}$$

where P_1^s and P_2^s are given by

$$P_1^s(\alpha) = 1 - \frac{\alpha - \alpha_1^s}{\alpha_2^s - \alpha_1^s} \tag{4.29}$$

$$P_2^s(\alpha) = \frac{\alpha - \alpha_1^s}{\alpha_2^s - \alpha_1^s} \tag{4.30}$$

Integrating, we have

$$b_{ik}^s = \frac{r_a \Delta}{6}(\delta_{ik} + 1) \tag{4.31}$$

Substituting the previous equations into (4.12) a sparse matrix is obtained for the nodal fields that has the form

$$\begin{bmatrix} A_{aa} & A_{aI} & 0 & -B_{aa} \\ A_{Ia} & A_{II} & A_{Id} & 0 \\ 0 & A_{dI} & A_{dd} & 0 \\ 0 & 0 & 0 & 0 \end{bmatrix} \begin{bmatrix} \phi_a \\ \phi_I \\ \phi_d \\ \psi_a \end{bmatrix} = \begin{bmatrix} 0 \\ 0 \\ 0 \\ 0 \end{bmatrix} \tag{4.32}$$

In this, the values of the elements in the submatrix A_{pq} are the contributions associated with the nodes in group (region or boundary) p which are connected directly to the nodes in group q. Also,

$$[B_{aa}]_{ik} = \sum_{s=1}^{N_a} b_{ik}^s = \frac{r_a \Delta}{6}(\delta_{i-1,k} + 4\delta_{ik} + \delta_{i+1,k}) \tag{4.33}$$

The last row in (4.32) has been intentionally left blank to imply a need for another set of equations relating the fields and its derivatives on Γ_a. This additional set of equations is produced by discretizing the boundary integral equation.

Evaluation of the Boundary Integral

The boundary integral in (4.5) may be rewritten in cylindrical coordinates via the transformations

$$|\overline{\rho} - \overline{\rho}_a| = |\hat{x}(\rho \cos \alpha - \rho_a \cos \alpha_a) - \hat{y}(\rho \sin \alpha - \rho_a \sin \alpha_a)|$$

$$= \sqrt{\rho^2 + \rho_a^2 - 2\rho\rho_a \cos(\alpha - \alpha_a)} \tag{4.34}$$

where (ρ, α) and (ρ_a, α_a) are the usual source and observation points in cylindrical coordinates. For $|\rho| = |\rho_a|$,

$$|\overline{\rho} - \overline{\rho}_a| = 2\rho \left|\sin\left(\tfrac{\alpha-\alpha_a}{2}\right)\right| \tag{4.35}$$

and the Green's function and its normal derivative may be written as

$$G(\overline{\rho}, \overline{\rho}_a) = -\frac{j}{4}H_o^{(2)}\left(2k_o\rho_a \sin\left(\tfrac{\alpha-\alpha_a}{2}\right)\right) \tag{4.36}$$

$$\frac{\partial}{\partial n_a}G(\overline{\rho}, \overline{\rho}_a) = \frac{jk_o}{4}H_1^{(2)}\left(2k_o\rho_a \sin\left(\tfrac{\alpha-\alpha_a}{2}\right)\right)\sin\left(\tfrac{\alpha-\alpha_a}{2}\right). \tag{4.37}$$

We may now write (4.5) as

$$\tfrac{1}{2}\phi(\rho, \alpha) = \phi^{inc}(\rho, \alpha) - f_0(\rho, \alpha) + f_1(\rho, \alpha) \tag{4.38}$$

where as a result of (4.36) and (4.37)

$$f_0(\rho, \alpha) = -\frac{j}{4}\rho_a \int_0^{2\pi} \psi(\rho_a, \alpha_a)H_o^{(2)}\left(2k_o\rho_a \sin\left(\tfrac{\alpha-\alpha_a}{2}\right)\right)d\alpha_a \tag{4.39}$$

$$f_1(\rho, \alpha) = \frac{j}{4}\rho_a \fint_0^{2\pi} \phi(\rho_a, \alpha_a)H_1^{(2)}\left(2k_o\rho_a \sin\left(\tfrac{\alpha-\alpha_a}{2}\right)\right)\sin\left(\tfrac{\alpha-\alpha_a}{2}\right)d\alpha_a \tag{4.40}$$

with

$$\psi(\rho_a, \alpha_a) = \frac{\partial}{\partial \rho_a}\phi(\rho_a, \alpha_a) \tag{4.41}$$

The factor of $\tfrac{1}{2}$ in (4.38) accounts for the singularity associated with $H_1^{(2)}(\cdot)$ and the $\fint$ (4.40) denotes principal value.

We may now discretize (4.39) by expanding the field using pulse basis functions as

$$\psi(\rho_a, \alpha_a) \simeq \sum_{j=1}^{N_a} P_\Delta(\alpha_a - \alpha_j)\psi_j \tag{4.42}$$

where

$$P_\Delta(\alpha_a - \alpha_j) = \begin{cases} 1 & |\alpha_a - \alpha_j| \le \tfrac{\Delta}{2} \\ 0 & \text{otherwise} \end{cases} \tag{4.43}$$

and Δ is the angular width of the integration cell as indicated in Fig. 4.2. Thus, the discrete version of (4.39) may be written as

$$f_0(\rho, \alpha) = -\frac{j\rho_a}{4} \sum_{j=1}^{N_a} \psi_j \int_{\alpha_j - \frac{\Delta}{2}}^{\alpha_j + \frac{\Delta}{2}} H_o^{(2)} \left(2k_o\rho_a \sin\left(\frac{\alpha - \alpha_a}{2}\right)\right) d\alpha_a \qquad (4.44)$$

Performing point collocation and letting $u' = \alpha - \alpha_a$, we have

$$f_0(\rho, \alpha_i) = -\frac{j\rho_a}{4} \sum_{j=1}^{N_a} \psi_j \int_{(\alpha_i - \alpha_j) - \frac{\Delta}{2}}^{(\alpha_i - \alpha_j) + \frac{\Delta}{2}} H_o^{(2)} \left(2k_o\rho_a \sin\left(\frac{u'}{2}\right)\right) du' \qquad (4.45)$$

which may be written in compact form as

$$f_0(\rho, \alpha_i) = -\frac{j\rho_a}{4} \sum_{j=1}^{N_a} \psi_j h_0(\alpha_i - \alpha_j) \qquad (4.46)$$

where

$$h_0(\alpha_i - \alpha_j) = \int_{(\alpha_i - \alpha_j) - \frac{\Delta}{2}}^{(\alpha_i - \alpha_j) + \frac{\Delta}{2}} H_o^{(2)} \left(2k_o\rho_a \sin\left(\frac{u}{2}\right)\right) du \qquad (4.47)$$

It is clear that (4.46) is in the form of a discrete convolution and can thus be written as

$$f_0(\rho, \alpha) = DFT^{-1} \left\{ DFT(\psi) \bullet DFT(h_0) \right\} \qquad (4.48)$$

where the elements of h_0 are given by

$$h_0(p\Delta) = \begin{cases} \Delta \left\{ 1 - j\frac{2}{\pi} \left[\ln\left(\frac{\gamma k_o \rho_a \Delta}{4}\right) - 1 \right] \right\} & p = 0 \\ \int_{(p-\frac{1}{2})\Delta}^{(p+\frac{1}{2})\Delta} H_o^{(2)} \left(2k_o\rho_a \sin\left(\frac{u'}{2}\right)\right) du' & p = 1, ..., N_a - 1 \end{cases} \qquad (4.49)$$

where in developing the $p = 0$ term, the small argument approximation of the Hankel function was used and is given by [12]

$$\lim_{k\rho \to 0} H_n^{(2)}(k\rho) = \begin{cases} 1 - j\frac{2}{\pi} \ln\left(\frac{\gamma k \rho}{2}\right) & n = 0 \\ \frac{(k\rho)^n}{2^n n!} + j\frac{2^n (n-1)!}{\pi(k\rho)^n} & n > 1 \end{cases} \qquad (4.50)$$

in which $\gamma \simeq 1.781$. Through a similar analysis, the field may be approximated by the expansion

$$\phi(\rho_a, \alpha_a) \simeq \sum_{j=1}^{N_a} P_\Delta(\alpha_a - \alpha_j)\phi_j \tag{4.51}$$

and by substituting this into (4.40), we obtain

$$f_1(\rho, \alpha_i) = j\frac{k_0 \rho_a}{4} \sum_{j=1}^{N_a} \phi_j h_1(\alpha_i - \alpha_j) \tag{4.52}$$

where

$$h_1(\alpha_i - \alpha_j) = \int_{(\alpha_i - \alpha_j) - \frac{\Delta}{2}}^{(\alpha_i - \alpha_j) + \frac{\Delta}{2}} H_1^{(2)}\left(2k_o\rho_a \sin\left(\tfrac{u'}{2}\right)\right) \sin\left(\tfrac{u'}{2}\right) du' \tag{4.53}$$

Clearly, (4.52) may again be written in operator form as

$$f_1(\rho, \alpha) = DFT^{-1}\left\{DFT(\phi) \bullet DFT(h_1)\right\} \tag{4.54}$$

where

$$h_1(p\Delta) = \begin{cases} k_0\rho_a\left(\frac{\Delta}{2} - \sin\frac{\Delta}{2}\right) + j\frac{\Delta}{\pi k_0 \rho_a} & p = 0 \\ \int_{(p-\frac{1}{2})\frac{\Delta}{2}}^{(p+\frac{1}{2})\frac{\Delta}{2}} H_1^{(2)}\left(2k_o\rho_a \sin\left(\tfrac{u'}{2}\right)\right) \sin\left(\tfrac{u'}{2}\right) du' & p = 1, ..., N_a - 1 \end{cases} \tag{4.55}$$

where again (4.50) was employed.

Point matching (4.38) at each node results in the system

$$\tfrac{1}{2}\phi_i = \phi_i^{inc} - f_0(\rho, \alpha_i) + f_1(\rho, \alpha_i) \tag{4.56}$$

which may be written in operator form as

$$M_{aa}\phi_a - L_{aa}\psi_a = \phi_a^{inc} \tag{4.57}$$

where

$$[L_{aa}]_{ij} = \frac{j\rho_a}{4}h_0(\alpha_i - \alpha_j) \tag{4.58}$$

$$[M_{aa}]_{ij} = \tfrac{1}{2}\delta_{ij} - \frac{j\rho_a k_0}{4}h_1(\alpha_i - \alpha_j) \tag{4.59}$$
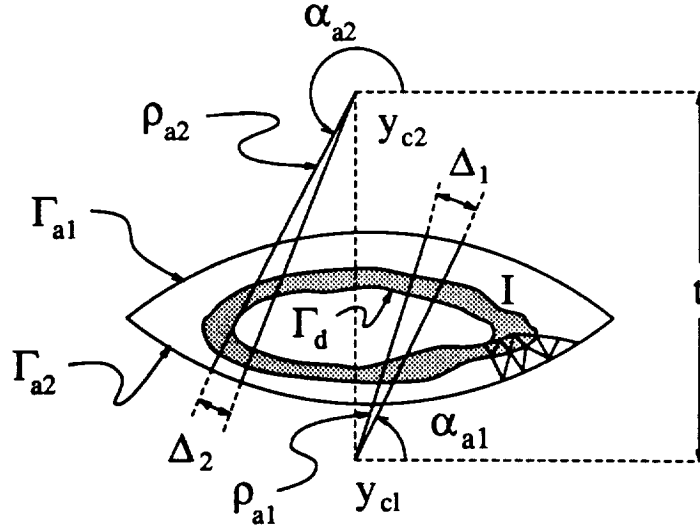
Figure 4.3: Partially discretized body with an ogival enclosure

A final system is obtained by combining (4.57) with (4.32) to yield

$$
\begin{bmatrix}
A_{aa} & A_{aI} & 0 & -B_{aa} \\
A_{Ia} & A_{II} & A_{Id} & 0 \\
0 & A_{dI} & A_{dd} & 0 \\
M_{aa} & 0 & 0 & -L_{aa}
\end{bmatrix}
\begin{bmatrix}
\phi_a \\
\phi_I \\
\phi_d \\
\psi_a
\end{bmatrix}
=
\begin{bmatrix}
0 \\
0 \\
0 \\
\phi_a^{inc}
\end{bmatrix}
\tag{4.60}
$$

which can be solved via the conjugate gradient algorithm to obtain the nodal fields.

4.2.2 Ogival Enclosure

Discretization of the Scatterer and Field Quantities

The region within Γ_a, denoted R_a, is discretized into N_e finite elements and a partial discretization is shown in Fig. 4.3 for the circular case. With respect to Fig. 4.3, the definitions of the various quantities are found in Table 4.3. Further definitions for the finite element mesh are indicated in Table 4.4, and the field vector definitions are indicated in Table 4.5.

Symbol	Description
Δ_p	angular displacement between nodes on Γ_{a_p}
ρ_{a_p}	radii of Γ_{a_p}
α_{a_p}	angular integration variable along Γ_{a_p}
t	distance between centers of curvature of Γ_{a_p}
y_{c_p}	y-coordinate of the center of curvature of Γ_{a_p}

Table 4.3: Geometric quantities in reference to the figure above

Symbol	Description
N_n	number of nodes in the finite element mesh
N_g	number of unknowns
N_e	number of elements in the finite element mesh
N_a	number of nodes $(=N_{a1} + N_{a2})$ on Γ_a
Γ_a	$\Gamma_{a_1} + \Gamma_{a_2}$

Table 4.4: Definitions for the finite element mesh with an ogival enclosure

Symbol	Description
ϕ_{a_p}	fields corresponding to the nodes on Γ_{a_p}, $p = 1, 2$
ψ_{a_p}	fields corresponding to the midpoints of the nodes on Γ_{a_p}
$\phi_{a_{p+\frac{1}{2}}}$	fields at the nodal midpoints on Γ_{a_p}
ϕ_I	fields corresponding to region I enclosed by Γ_a and Γ_d
ϕ_d	fields corresponding to the nodes on the Γ_d

Table 4.5: Definition of the field vectors for the ogival boundary

Derivation of the Finite Element Matrix

The derivation of the finite element matrix follows that described in section 4.2.1 with the exception of the matrix $B_{\alpha\alpha}$. Consider the ogival boundary as indicated in Fig. 4.3. The boundary contour Γ_α is comprised of two arcs labeled Γ_{α_1} and Γ_{α_2}, which form the vertices of the ogive where they meet. At the vertices the unknown normal field is discontinuous and will therefore be evaluated at the midpoint. Also, in evaluating the contour integral, the field derivative are expanded in terms of pulse basis functions, rather than linear functions. This results in a different $B_{\alpha\alpha}$ matrix and involves the replacement of P_j^e in (4.28) by the pulse basis function expansion

$$P_\Delta(\alpha - \alpha_j) = \begin{cases} 1 & \text{if } 0 \leq |\alpha - \alpha_j| \leq \frac{\Delta}{2} \\ 0 & \text{otherwise} \end{cases} \tag{4.61}$$

By integrating in cylindrical coordinates we then obtain

$$b_{ij}^e = \frac{l^e}{2}(\delta_{ij} + \delta_{i,j+1}), \quad j = 1, \; i = 1,2 \tag{4.62}$$

where l^e is the length of the eth boundary element along Γ_α and is equal to $\rho_{\alpha_p}\Delta_p$ for Γ_{α_p}, $p = 1,2$. Performing a summation over all boundary elements then yields

$$[B_{\alpha\alpha}]_{ij} = \sum_{e=1}^{N_e} b_{ij}^e = \frac{l^j}{2}(\delta_{ij} + \delta_{i,j+1}) \tag{4.63}$$

where l^j is the length of the jth element since the jth "node" (associated with the unknown ψ_j) is at the center of the jth boundary element.

The remainder of finite element analysis for this case proceeds exactly as in section 4.2.1.

Evaluation of the Boundary Integral

The evaluation of the boundary integral along an ogival contour is similar to that described for the circular boundary. For integration and observation points

on the same arc, the integrals become convolutions. On the other hand, when the integration and observation points reside on different contours, the integrals have no special form and must be discretized and stored in memory as efficiently as possible.

The distance between the source and observation points in terms of cylindrical coordinates for points on the same arc is given by

$$|\bar{\rho} - \bar{\rho}_{a_p}| = \sqrt{\rho^2 + \rho_{a_p}^2 - 2\rho\rho_{a_p}\cos(\alpha - \alpha_{a_p})} \quad p = 1, 2 \tag{4.64}$$

When the source and observation points are along different arcs, (4.64) becomes

$$|\bar{\rho}_q - \bar{\rho}_{a_p}| = \sqrt{(\rho\cos\alpha_q - \rho_a\cos\alpha_{a_p})^2 + (\rho\sin\alpha_q - \rho_a\sin\alpha_{a_p} + y_{c_q} - y_{c_p})^2}$$

$$p, q = 1, 2 \tag{4.65}$$

in which the subscript a_p refers to the integration coordinates along contour p and the subscript q refers to the observation coordinates. Also, y_{c_p} is the y-coordinate of the center of curvature for contour p for $p = 1, 2$. For further reference we note that (4.65) may be also rewritten as

$$|\bar{\rho}_{\frac{1}{2}} - \bar{\rho}_{a_{\frac{2}{1}}}| =$$

$$\sqrt{(\rho_{\frac{1}{2}}^2 + \rho_{a_{\frac{2}{1}}}^2 - 2\rho_{\frac{1}{2}}\rho_{a_{\frac{2}{1}}}\cos(\alpha_{\frac{1}{2}} - \alpha_{a_{\frac{2}{1}}}) + t^2 \mp 2t(\rho_{\frac{1}{2}}\sin\alpha_{\frac{1}{2}} - \rho_{a_{\frac{2}{1}}}\sin\alpha_{a_{\frac{2}{1}}})} \tag{4.66}$$

where $t = y_{c_2} - y_{c_1}$ and the upper sign corresponds to the upper set of subscripts.

To discretize (4.5), the fields are expanded as

$$\phi(\rho_a, \alpha_a) \simeq \sum_{j=1}^{N_{a_1}} P_\Delta(\alpha_a - \alpha_j)\phi_{j+\frac{1}{2}} + \sum_{j=N_{a_1}+1}^{N_a} P_\Delta(\alpha_a - \alpha_j)\phi_{j+\frac{1}{2}} \tag{4.67}$$

$$\psi(\rho_a, \alpha_a) \simeq \sum_{j=1}^{N_{a_1}} P_\Delta(\alpha_a - \alpha_j)\psi_j + \sum_{j=N_{a_1}+1}^{N_a} P_\Delta(\alpha_a - \alpha_j)\psi_j \tag{4.68}$$

where as before

$$P_\Delta(\alpha_a - \alpha_j) = \begin{cases} 1 & \text{if } |\alpha_a - \alpha_j| \leq \frac{\Delta}{2} \\ 0 & \text{otherwise} \end{cases} \tag{4.69}$$

and

$$\phi_{j+\frac{1}{2}} = \tfrac{1}{2}(\phi_j + \phi_{j+1}) \tag{4.70}$$

Substituting (4.67), (4.68) and (4.69) into (4.5) then yields

$$
\begin{aligned}
\tfrac{1}{2}\phi(\rho_1,\alpha_1) =\ & \phi^{inc}(\rho_1,\alpha_1) \\
& - \sum_{j=1}^{N_{a_1}} \psi_j \int_{\alpha_j}^{\alpha_j+\Delta_1} G_o(\rho_1,\rho_{a_1},\alpha_1-\alpha_{a_1})\rho_{a_1}d\alpha_{a_1} \\
& + \sum_{j=1}^{N_{a_1}} \phi_{j+\frac{1}{2}} \fint_{\alpha_j}^{\alpha_j+\Delta_1} \frac{\partial}{\partial\rho_{a_1}} G_o(\rho_1,\rho_{a_1},\alpha_1-\alpha_{a_1})\rho_{a_1}d\alpha_{a_1} \\
& - \sum_{j=N_{a_1}+1}^{N_a} \psi_j \int_{\alpha_j}^{\alpha_j+\Delta_2} G_o(\rho_1,\rho_{a_2},\alpha_1,\alpha_{a_2})\rho_{a_2}d\alpha_{a_2} \\
& + \sum_{j=N_{a_1}+1}^{N_a} \phi_{j+\frac{1}{2}} \fint_{\alpha_j}^{\alpha_j+\Delta_2} \frac{\partial}{\partial\rho_{a_2}} G_o(\rho_1,\rho_{a_2},\alpha_1,\alpha_{a_2})\rho_{a_2}d\alpha_{a_2} \tag{4.71}
\end{aligned}
$$

when the observation point is on Γ_{a_1} and

$$
\begin{aligned}
\tfrac{1}{2}\phi(\rho_2,\alpha_2) =\ & \phi^{inc}(\rho_2,\alpha_2) \\
& - \sum_{j=1}^{N_{a_1}} \psi_j \int_{\alpha_j}^{\alpha_j+\Delta_1} G_o(\rho_2,\rho_{a_1},\alpha_2,\alpha_{a_1})\rho_{a_1}d\alpha_{a_1} \\
& + \sum_{j=1}^{N_{a_1}} \phi_{j+\frac{1}{2}} \fint_{\alpha_j}^{\alpha_j+\Delta_1} \frac{\partial}{\partial\rho_{a_1}} G_o(\rho_2,\rho_{a_1},\alpha_2,\alpha_{a_1})\rho_{a_1}d\alpha_{a_1} \\
& - \sum_{j=N_{a_1}+1}^{N_a} \psi_j \int_{\alpha_j}^{\alpha_j+\Delta_2} G_o(\rho_2,\rho_{a_2},\alpha_2-\alpha_{a_2})\rho_{a_2}d\alpha_{a_2} \\
& + \sum_{j=N_{a_1}+1}^{N_a} \phi_{j+\frac{1}{2}} \fint_{\alpha_j}^{\alpha_j+\Delta_2} \frac{\partial}{\partial\rho_{a_2}} G_o(\rho_2,\rho_{a_2},\alpha_2-\alpha_{a_2})\rho_{a_2}d\alpha_{a_2} \tag{4.72}
\end{aligned}
$$

for observation on Γ_{a_2}. Performing point collocation at the nodal midpoints, (4.71) and (4.72) further reduce to

$$
\begin{aligned}
\tfrac{1}{2}\phi(\rho_1,\alpha_{i+\frac{1}{2}}) =\ & \phi^{inc}(\rho_1,\alpha_{i+\frac{1}{2}}) \\
& - \sum_{j=1}^{N_{a_1}} \psi_j \int_{\alpha_i-\alpha_j+\frac{\Delta}{2}}^{\alpha_i-\alpha_j+\frac{\Delta}{2}} G_o(\rho_1,\rho_{a_1},u)\rho_{a_1}du
\end{aligned}
$$

$$+ \sum_{j=1}^{N_{a_1}} \phi_{j+\frac{1}{2}} \int_{\alpha_i-\alpha_j+\frac{\Delta}{2}}^{\alpha_i-\alpha_j+\frac{\Delta}{2}} \frac{\partial}{\partial \rho_{a_1}} G_o(\rho_1, \rho_{a_1}, u) \rho_{a_1} du$$

$$- \sum_{j=N_{a_1}+1}^{N_a} \psi_j \int_{\alpha_j}^{\alpha_j+\Delta_2} G_o(\rho_1, \rho_{a_2}, \alpha_{i+\frac{1}{2}}, \alpha_{a_2}) \rho_{a_2} d\alpha_{a_2}$$

$$+ \sum_{j=N_{a_1}+1}^{N_a} \phi_{j+\frac{1}{2}} \int_{\alpha_j}^{\alpha_j+\Delta_2} \frac{\partial}{\partial \rho_{a_2}} G_o(\rho_1, \rho_{a_2}, \alpha_{i+\frac{1}{2}}, \alpha_{a_2}) \rho_{a_2} d\alpha_{a_2} \quad (4.73)$$

for observation on Γ_{a_1} and

$$\frac{1}{2} \phi(\rho_2, \alpha_{i+\frac{1}{2}}) = \phi^{inc}(\rho_2, \alpha_{i+\frac{1}{2}})$$

$$- \sum_{j=1}^{N_{a_1}} \psi_j \int_{\alpha_j}^{\alpha_j+\Delta_1} G_o(\rho_2, \rho_{a_1}, \alpha_{i+\frac{1}{2}}, \alpha_{a_1}) \rho_{a_1} d\alpha_{a_1}$$

$$+ \sum_{j=1}^{N_{a_1}} \phi_{j+\frac{1}{2}} \int_{\alpha_j}^{\alpha_j+\Delta_1} \frac{\partial}{\partial \rho_{a_1}} G_o(\rho_2, \rho_{a_1}, \alpha_{i+\frac{1}{2}}, \alpha_{a_1}) \rho_{a_1} d\alpha_{a_1}$$

$$- \sum_{j=N_{a_1}+1}^{N_a} \psi_j \int_{\alpha_i-\alpha_j+\frac{\Delta}{2}}^{\alpha_i-\alpha_j+\frac{\Delta}{2}} G_o(\rho_2, \rho_{a_2}, u) \rho_{a_2} du$$

$$+ \sum_{j=N_{a_1}+1}^{N_a} \phi_{j+\frac{1}{2}} \int_{\alpha_i-\alpha_j+\frac{\Delta}{2}}^{\alpha_i-\alpha_j+\frac{\Delta}{2}} \frac{\partial}{\partial \rho_{a_2}} G_o(\rho_2, \rho_{a_2}, u) \rho_{a_2} du \quad (4.74)$$

where the '$\frac{1}{2}$' in the subscript refers to the fictitious "node" midway between the actual nodes. A system of equations can now be obtained by testing (4.73) and (4.74) at a sequence of points on the contours. This yields

$$\frac{1}{4} C_1 \phi_{a_1} = \phi^{inc}_{a_1+\frac{1}{2}} - \left\{ L_{11} \psi_{a_1} + P_{12} \psi_{a_2} - \frac{1}{2} M_{11} C_1 \phi_{a_1} - \frac{1}{2} Q_{12} C_2 \phi_{a_2} \right\}$$

$$\frac{1}{4} C_2 \phi_{a_2} = \phi^{inc}_{a_2+\frac{1}{2}} - \left\{ P_{21} \psi_{a_1} + L_{22} \psi_{a_2} - \frac{1}{2} Q_{21} C_1 \phi_{a_1} - \frac{1}{2} M_{22} C_2 \phi_{a_2} \right\} \quad (4.75)$$

which can be alternatively written as

$$\left[\begin{bmatrix} \mathcal{M}_{11} C_1 & \mathcal{Q}_{12} C_2 \\ \mathcal{Q}_{21} C_1 & \mathcal{M}_{22} C_2 \end{bmatrix} \begin{bmatrix} D \end{bmatrix} \begin{matrix} L_{11} & P_{12} \\ P_{21} & L_{22} \end{matrix} \right] \begin{bmatrix} \phi_{a_1} \\ \phi_{a_2} \\ \psi_{a_1} \\ \psi_{a_2} \end{bmatrix} = \begin{bmatrix} \phi^{inc}_{a_1+\frac{1}{2}} \\ \phi^{inc}_{a_2+\frac{1}{2}} \end{bmatrix} \quad (4.76)$$

In this, the nonzero values of the upper bidiagonal matrix C are 1, and $\phi^{inc}_{a_p+\frac{1}{2}}$ the value of the incident field evaluated at the nodal midpoints. The matrix D accounts for the double use of the nodes at the endpoints and the remaining elements are given by

$$\mathcal{M}_{pp} = \tfrac{1}{2}(\tfrac{1}{2}I - M_{pp}) \tag{4.77}$$

$$\mathcal{Q}_{pq} = -\tfrac{1}{2}Q_{pq} \tag{4.78}$$

$$\tag{4.79}$$

for $p = 1,2$ in which

$$[M_{pp}]_{ij} = \int_{\alpha_i-\alpha_j+\frac{\Delta_p}{2}}^{\alpha_i-\alpha_j+\frac{\Delta_p}{2}} G_o(\rho_p, \rho_{a_p}, u)\rho_{a_p}du \tag{4.80}$$

$$[L_{pp}]_{ij} = \fint_{\alpha_i-\alpha_j+\frac{\Delta_p}{2}}^{\alpha_i-\alpha_j+\frac{\Delta_p}{2}} \frac{\partial}{\partial\rho_{a_p}} G_o(\rho_p, \rho_{a_p}, u)\rho_{a_p}du \tag{4.81}$$

$$[Q_{pq}]_{ij} = \int_{\alpha_j}^{\alpha_j+\Delta_q} G_o(\rho_p, \rho_{a_q}, \alpha_{i+\frac{1}{2}}, \alpha_{a_q})\rho_{a_q}d\alpha_{a_q} \tag{4.82}$$

and

$$[P_{pq}]_{ij} = \int_{\alpha_j}^{\alpha_j+\Delta_q} \frac{\partial}{\partial\rho_{a_q}} G_o(\rho_p, \rho_{a_q}, \alpha_{i+\frac{1}{2}}, \alpha_{a_q})\rho_{a_q}d\alpha_{a_q} \tag{4.83}$$

More explicitly, upon evaluation of the integrals

$$[M_{pp}]_{ij} = \begin{cases} j\frac{k_o\rho_{a_p}}{4}\left[k_o\rho_{a_p}(\frac{\Delta_p}{2} - \sin\frac{\Delta_p}{2}) + \frac{j\Delta_p}{\pi k_o\rho_{a_p}}\right] & i = j \\ j\frac{k_o\rho_{a_p}}{4}\int_{\alpha_i-\alpha_j+\frac{\Delta_p}{2}}^{\alpha_i-\alpha_j+\frac{\Delta_p}{2}} H_1^{(2)}(2k_o\rho_{a_p}\sin\frac{u}{2})\sin\frac{u}{2}du & i \neq j \end{cases} \tag{4.84}$$

$$[L_{pp}]_{ij} = \begin{cases} -j\frac{k_o\rho_{a_p}}{4}\left\{1 - j\frac{2}{\pi}\left[\ln\left(\frac{\gamma k_o\rho_{a_p}\Delta_p}{4}\right) - 1\right]\right\} & i = j \\ -j\frac{\rho_{a_p}}{4}\int_{\alpha_i-\alpha_j+\frac{\Delta_p}{2}}^{\alpha_i-\alpha_j+\frac{\Delta_p}{2}} H_0^{(2)}(2k_o\rho_{a_p}\sin\frac{u}{2})du & i \neq j \end{cases} \tag{4.85}$$

$$\left[Q^{12}_{21}\right]_{ij} = j\frac{k_o\rho_{a_2}}{4}\int_{\alpha_j}^{\alpha_j+\Delta_2} \frac{H_1^{(2)}(k_o\sqrt{\cdot\mp t\cdot})}{(k_o\sqrt{\cdot\mp t\cdot})} \left[\rho_{a_2} - \rho_1\cos(\alpha_1 - \alpha_{a_2}) \pm t\sin\alpha_{a_2}\right]d\alpha_{a_2} \tag{4.86}$$

$$\left[P^{12}_{21}\right]_{ij} = -j\frac{\rho_{a_2}}{4}\int_{\alpha_j}^{\alpha_j+\Delta_2} H_0^{(2)}(k_o\sqrt{\cdot\mp t\cdot})d\alpha_{a_2} \tag{4.87}$$

where the upper sign corresponds to the upper set of subscripts on P or Q, while the lower sign corresponds to the lower set of subscripts. Introducing the definitions

$$K_1 = \begin{bmatrix} \mathcal{M}_{11}C_1 & \mathcal{Q}_{12}C_2 \\ \mathcal{Q}_{21}C_1 & \mathcal{M}_{22}C_2 \end{bmatrix} \begin{bmatrix} D \end{bmatrix} \tag{4.88}$$

$$K_2 = \begin{bmatrix} L_{11} & P_{12} \\ P_{21} & L_{22} \end{bmatrix} \tag{4.89}$$

the system (4.76) may be combined with that derived via the finite element method to obtain

$$\begin{bmatrix} A_{aa} & A_{aI} & 0 & -B_{aa} \\ A_{Ia} & A_{II} & A_{Id} & 0 \\ 0 & A_{dI} & A_{dd} & 0 \\ K_1 & 0 & 0 & K_2 \end{bmatrix} \begin{bmatrix} \phi_a \\ \phi_I \\ \phi_d \\ \psi_a \end{bmatrix} = \begin{bmatrix} 0 \\ 0 \\ 0 \\ \phi_{a+\frac{1}{2}}^{inc} \end{bmatrix} \tag{4.90}$$

We note that (4.90) can be solved via the CG algorithm to take advantage of the convolution operators M and L in reducing the memory requirements. This algorithm is given next.

4.3 A CGFFT Implementation

In a manner similar to the previous chapter, the matrix vector multiplications Az and $A^a z$ is represented as a summation of matrices, one corresponding to the finite element portion of the system and the other corresponding to the boundary integral portion. Thus, a typical product may be represented as

$$\{s\} = \{s\}_{BI} + \{s\}_{FE} \tag{4.91}$$

where

$$\{s\}_{BI} = \begin{bmatrix} 0 & 0 & 0 & 0 \\ 0 & 0 & 0 & 0 \\ 0 & 0 & 0 & 0 \\ K_1 & 0 & 0 & K_2 \end{bmatrix} \begin{bmatrix} z_1 \\ z_2 \\ z_3 \\ z_4 \end{bmatrix} \qquad (4.92)$$

and

$$\{s\}_{FE} = \begin{bmatrix} A_{aa} & A_{aI} & 0 & B_{aa} \\ A_{Ia} & A_{II} & A_{Id} & 0 \\ 0 & 0 & A_{dd} & 0 \\ 0 & 0 & 0 & 0 \end{bmatrix} \begin{bmatrix} z_1 \\ z_2 \\ z_3 \\ z_4 \end{bmatrix} \qquad (4.93)$$

For the adjoint operations, we have

$$\{s\}_{BI} = \begin{bmatrix} 0 & 0 & 0 & K_1^a \\ 0 & 0 & 0 & 0 \\ 0 & 0 & 0 & 0 \\ 0 & 0 & 0 & K_2^a \end{bmatrix} \begin{bmatrix} z_1 \\ z_2 \\ z_3 \\ z_4 \end{bmatrix} \qquad (4.94)$$

and

$$\{s\}_{FE} = \begin{bmatrix} A_{aa}^a & A_{aI}^a & 0 & 0 \\ A_{Ia}^a & A_{II}^a & A_{Id}^a & 0 \\ 0 & A_{dI}^a & A_{dd}^a & 0 \\ B_{aa} & 0 & 0 & 0 \end{bmatrix} \begin{bmatrix} z_1 \\ z_2 \\ z_3 \\ z_4 \end{bmatrix} \qquad (4.95)$$

Again, the operation is performed such that only the resulting vector $\{s\}$ needs to be stored.

4.4 Scattered Field Computation

In this section the expressions for the scattered field and radar cross-section are developed for both the circular and ogival boundaries. The scattered field is com-

puted from the identity

$$\phi^s(\overline{p}) = -\oint_{\Gamma_a} \left\{ G(\overline{p}, \overline{p}_a) \left[\frac{\partial}{\partial n_a} \phi(\overline{p}_a) \right] - \phi(\overline{p}_a) \left[\frac{\partial}{\partial n_a} G(\overline{p}, \overline{p}_a) \right] \right\} d\Gamma_a \qquad (4.96)$$

from which the echowidth is calculated.

4.4.1 Circular Boundary

The scattered field expression (4.96) may be written as

$$\phi^s(\rho, \alpha) = -f_0(\rho, \alpha) + f_1(\rho, \alpha) \qquad (4.97)$$

where

$$f_0(\rho, \alpha) = -\frac{j}{4} \rho_a \int_0^{2\pi} \psi(\rho_a, \alpha_a) H_o^{(2)} \left(k_0 \sqrt{\rho^2 + \rho_a^2 - 2\rho\rho_a \cos(\alpha - \alpha_a)} \right) d\alpha_a \qquad (4.98)$$

and

$$f_1(\rho, \alpha) = \frac{j}{4} \rho_a k_0 \int_0^{2\pi} \phi(\rho_a, \alpha_a) \frac{H_1^{(2)} \left(k_0 \sqrt{\rho^2 + \rho_a^2 - 2\rho\rho_a \cos(\alpha - \alpha_a)} \right)}{\sqrt{\rho^2 + \rho_a^2 - 2\rho\rho_a \cos(\alpha - \alpha_a)}}$$
$$[\rho_a - \rho \cos(\alpha - \alpha_a)] \, d\alpha_a \qquad (4.99)$$

To evaluate the integrals in (4.98) and (4.99) we invoke the field expansions (4.42) and (4.51). We have

$$f_0(\rho, \alpha) = -\frac{j}{4} \rho_a \sum_{j=1}^{N_a} \psi_j \int_{\alpha_j - \frac{\Delta}{2}}^{\alpha_j + \frac{\Delta}{2}} H_o^{(2)} \left(k_0 \sqrt{\rho^2 + \rho_a^2 - 2\rho\rho_a \cos(\alpha - \alpha_a)} \right) d\alpha_a \qquad (4.100)$$

and

$$f_1(\rho, \alpha) = \frac{j}{4} k_0 \rho_a \sum_{j=1}^{N_a} \phi_j \int_{\alpha_j - \frac{\Delta}{2}}^{\alpha_j + \frac{\Delta}{2}} \frac{H_1^{(2)} \left(k_0 \sqrt{\rho^2 + \rho_a^2 - 2\rho\rho_a \cos(\alpha - \alpha_a)} \right)}{\sqrt{\rho^2 + \rho_a^2 - 2\rho\rho_a \cos(\alpha - \alpha_a)}}$$
$$[\rho_a - \rho \cos(\alpha - \alpha_a)] \, d\alpha_a \qquad (4.101)$$

where the remaining integrals over the subsections must be evaluated numerically for arbitrary observation. However, for far-field computations ($\rho \rightarrow \infty$), the Hankel

functions may be approximated as

$$H_n^{(2)}(k\rho) \sim \sqrt{\frac{2j}{\pi k\rho}} j^n e^{-jk\rho}$$ (4.102)

and since

$$\sqrt{\rho^2 + \rho_a^2 - 2\rho\rho_a \cos(\alpha - \alpha_a)} \simeq \begin{cases} \rho & \text{for amplitude} \\ \rho - \rho_a \cos(\alpha - \alpha_a) & \text{for phase terms} \end{cases}$$ (4.103)

(4.100) and (4.101) become

$$f_0(\rho, \alpha) = -j\frac{\rho_a \Delta}{4} \sqrt{\frac{2j}{\pi k_0 \rho}} e^{-jk_0\rho} \sum_{j=1}^{N_a} \psi_j e^{jk_0\rho_a \cos(\alpha - \alpha_j)}$$ (4.104)

and

$$f_1(\rho, \alpha) = \frac{\rho_a k_0 \Delta}{4} \sqrt{\frac{2j}{\pi k_0 \rho}} e^{-jk_0\rho} \sum_{j=1}^{N_a} \phi_j \cos(\alpha - \alpha_j) e^{jk_0\rho_a \cos(\alpha - \alpha_j)}$$ (4.105)

Substituting (4.104) and (4.105) into (4.97) we obtain

$$\phi_H^s(\rho, \alpha) = \frac{\rho_a \Delta}{4} \sqrt{\frac{2j}{\pi k_0 \rho}} e^{-jk_0\rho} \left[j \sum_{j=1}^{N_a} \psi_j e^{jk_0\rho_a \cos(\alpha - \alpha_j)} \right.$$
$$\left. + k_0 \sum_{j=1}^{N_a} \phi_j \cos(\alpha - \alpha_j) e^{jk_0\rho_a \cos(\alpha - \alpha_j)} \right]$$ (4.106)

and from (2.31) the echowidth is given by yields the echowidth

$$\sigma = \frac{(\rho_a \Delta)^2}{8\pi} \left| j \sum_{j=1}^{N_a} \psi_j e^{jk_0\rho_a \cos(\alpha - \alpha_j)} + k_0 \sum_{j=1}^{N_a} \phi_j \cos(\alpha - \alpha_j) e^{jk_0\rho_a \cos(\alpha - \alpha_j)} \right|^2$$ (4.107)

4.4.2 Ogival Boundary

Following the same discretization scheme used in Section 4.2.2, (4.96) may be written as

$$\phi^s(\rho, \alpha) = -\left\{ \sum_{j=1}^{N_{a_1}} \psi f_{11}(\rho, \alpha, \alpha_j) + \sum_{j=N_{a_1}+1}^{N_a} \psi f_{12}(\rho, \alpha, \alpha_j) \right.$$
$$\left. - \sum_{j=1}^{N_{a_1}} \phi f_{21}(\rho, \alpha, \alpha_j) - \sum_{j=N_{a_1}+1}^{N_a} \phi f_{22}(\rho, \alpha, \alpha_j) \right\}$$ (4.108)

where

$$f_{1p}(\rho, \alpha, \alpha_j) = \int_{\alpha_j}^{\alpha_j + \Delta_p} G_o(\rho, \rho_{a_p}, \alpha, \alpha_{a_p}) \rho_{a_p} d\alpha_{a_p} \tag{4.109}$$

$$f_{2p}(\rho, \alpha, \alpha_j) = \int_{\alpha_j}^{\alpha_j + \Delta_p} \frac{\partial}{\partial \rho_{a_p}} G_o(\rho, \rho_{a_p}, \alpha, \alpha_{a_p}) \rho_{a_p} d\alpha_{a_p} \tag{4.110}$$

$$\tag{4.111}$$

in which

$$G_o(\rho, \rho_{a_p}, \alpha, \alpha_{a_p})$$

$$= -\frac{j}{4} H_o^{(2)} \left(k_o \sqrt{\rho^2 + \rho_{a_p}^2 - 2\rho\rho_{a_p} \cos(\alpha - \alpha_{a_p}) + y_{c_p}^2 - 2y_{c_p}(\rho \sin \alpha - \rho_{a_p} \sin \alpha_{a_p})} \right)$$

$$\tag{4.112}$$

and

$$\frac{\partial}{\partial \rho_{a_p}} G_o(\rho, \rho_{a_p}, \alpha, \alpha_{a_p})$$

$$= \frac{jk_o}{4} \frac{H_1^{(2)} \left(k_o \sqrt{\rho^2 + \rho_{a_p}^2 - 2\rho\rho_{a_p} \cos(\alpha - \alpha_{a_p}) + y_{c_p}^2 - 2y_{c_p}(\rho \sin \alpha - \rho_{a_p} \sin \alpha_{a_p})} \right)}{\sqrt{\rho^2 + \rho_{a_p}^2 - 2\rho\rho_{a_p} \cos(\alpha - \alpha_{a_p}) + y_{c_p}^2 - 2y_{c_p}(\rho \sin \alpha - \rho_{a_p} \sin \alpha_{a_p})}}$$

$$\left[\rho_{a_p} - \rho \cos(\alpha - \alpha_{a_p}) + y_{c_p} \sin \alpha_{a_p} \right]$$

$$\tag{4.113}$$

and y_{c_p} are the corresponding y-coordinates of the arc Γ_{a_p}. Using the large argument

approximation for the Hankel function and the approximation

$$\sqrt{\rho + \rho_{a_p}^2 - 2\rho\rho_{a_p} \cos(\alpha - \alpha_{a_p}) + y_{c_p}^2 + 2y_{c_p}(\rho \sin \alpha - \rho_{a_p} \sin \alpha_{a_p})}$$

$$= \begin{cases} \rho & \text{for amplitude terms} \\ \rho - \rho_{a_p} \cos(\alpha - \alpha_{a_p}) + y_{c_p} \sin \alpha & \text{for phase terms} \end{cases} \tag{4.114}$$

for $\rho \to \infty$, the Hankel function simplifies to

$$H_0^{(2)}(\sqrt{\cdot y_{c_p} \cdot})) \sim \sqrt{\frac{2j}{\pi k_o \rho}} e^{-jk_o\rho} e^{-jk_o[-\rho_{a_p} \cos(\alpha - \alpha_{a_p}) - y_{c_p} \sin \alpha]} \tag{4.115}$$

78

Similarly,

$$\frac{H_1^{(2)}(\sqrt{\cdot y_{c_p}\cdot})}{\sqrt{\cdot y_{c_p}\cdot}}\left[\cdot y_{c_p}\cdot\right] \sim -j\sqrt{\frac{2j}{\pi k_o\rho}}e^{-jk_o\rho}e^{-jk_o\left[-\rho_{a_p}\cos(\alpha-\alpha_{a_p})-y_{c_p}\sin\alpha\right]}\cos(\alpha-\alpha_{a_p})$$

(4.116)

Substutiting these into (4.109) and (4.110) and performing midpoint integration yields

$$f_{1p}(\rho,\alpha,\alpha_j) = -j\frac{\Delta_p\rho_{a_p}}{4}\sqrt{\frac{2j}{\pi k_o\rho}}e^{-jk_o\rho}e^{-jk_o\left[-\rho_{a_p}\cos(\alpha-\alpha_j-\frac{\Delta_p}{2})-y_{c_p}\sin\alpha\right]}$$ (4.117)

$$f_{2p}(\rho,\alpha,\alpha_j) = k_o\frac{\Delta_p\rho_{a_p}}{4}\sqrt{\frac{2j}{\pi k_o\rho}}e^{-jk_o\rho}e^{-jk_o\left[-\rho_{a_p}\cos(\alpha-\alpha_j-\frac{\Delta_p}{2})-y_{c_p}\sin\alpha\right]}$$

$$\cos(\alpha_j+\frac{\Delta_p}{2}-\alpha_{a_p})$$ (4.118)

Thus, from (4.108)

$$\phi_H^s(\rho,\alpha) = \frac{1}{4}\sqrt{\frac{2j}{\pi k_o\rho}}e^{-jk_o\rho}$$

$$\left\{j\Delta_1\rho_{a_1}\sum_{j=1}^{N_{a_1}}\psi_{j+\frac{1}{2}}e^{-jk_o\left[-\rho_{a_1}\cos(\alpha-\alpha_j-\frac{\Delta_1}{2})-y_{c_1}\sin\alpha\right]}\right.$$

$$+\ j\Delta_2\rho_{a_2}\sum_{j=N_{a_1}+1}^{N_a}\psi_{j+\frac{1}{2}}e^{-jk_o\left[-\rho_{a_2}\cos(\alpha-\alpha_j-\frac{\Delta_2}{2})-y_{c_2}\sin\alpha\right]}$$

$$+\ k_o\Delta_1\rho_{a_1}\sum_{j=1}^{N_{a_1}}\phi_{j+\frac{1}{2}}e^{-jk_o\left[-\rho_{a_1}\cos(\alpha-\alpha_j-\frac{\Delta_1}{2})-y_{c_1}\sin\alpha\right]}\cos(\alpha-\alpha_j-\frac{\Delta_1}{2})$$

$$\left.+\ k_o\Delta_2\rho_{a_2}\sum_{j=N_{a_1}+1}^{N_a}\phi_{j+\frac{1}{2}}e^{-jk_o\left[-\rho_{a_2}\cos(\alpha-\alpha_j-\frac{\Delta_2}{2})-y_{c_2}\sin\alpha\right]}\cos(\alpha-\alpha_j-\frac{\Delta_2}{2})\right\}$$

(4.119)

the echowidth becomes

$$\sigma = \frac{1}{8\pi}\left|j\Delta_1\rho_{a_1}\sum_{j=1}^{N_{a_1}}\psi_{j+\frac{1}{2}}e^{-jk_o\left[-\rho_{a_1}\cos(\alpha-\alpha_j-\frac{\Delta_1}{2})-y_{c_1}\sin\alpha\right]}\right.$$

$$+\ j\Delta_2\rho_{a_2}\sum_{j=N_{a_1}+1}^{N_a}\psi_{j+\frac{1}{2}}e^{-jk_o\left[-\rho_{a_2}\cos(\alpha-\alpha_j-\frac{\Delta_2}{2})-y_{c_2}\sin\alpha\right]}$$

$$+\ k_o\Delta_1\rho_{a_1}\sum_{j=1}^{N_{a_1}}\phi_{j+\frac{1}{2}}e^{-jk_o\left[-\rho_{a_1}\cos(\alpha-\alpha_j-\frac{\Delta_1}{2})-y_{c_1}\sin\alpha\right]}\cos(\alpha_j+\frac{\Delta_1}{2}-\alpha_{a_1})$$

$$+ k_o \Delta_2 \rho_{a_2} \sum_{j=N_{a_1}+1}^{N_a} \phi_{j+\frac{1}{2}} e^{-jk_o \left[-\rho_{a_2} \cos(\alpha - \alpha_j - \frac{\Delta_2}{2}) - y_{c_2} \sin \alpha \right]} \cos(\alpha_j + \frac{\Delta_2}{2} - \alpha_{a_2}) \Big|^2$$

$$(4.120)$$

4.5 Results

The scattering patterns of several circular and ogival cylinders for both E- and H- polarization are shown in the figures to follow. Figs. 4.4-4.6 contain circular geometries both coated and uncoated, while Figs. 4.7-4.9 contain coated and uncoated ogival structures. The echowidth is computed for each structure and compared to the results of the series solution for the circular bodies and moment method [13, 14] for the ogival structures. As seen in all cases, the generated patterns via the FE–BI formulation are in excellent agreement with the corresponding data based on the Mie Series and Moment Method Solutions.

Perfectly Conducting Cylinder R=.5 λ (E-pol)

Perfectly Conducting Cylinder R=.5 λ (H-pol)
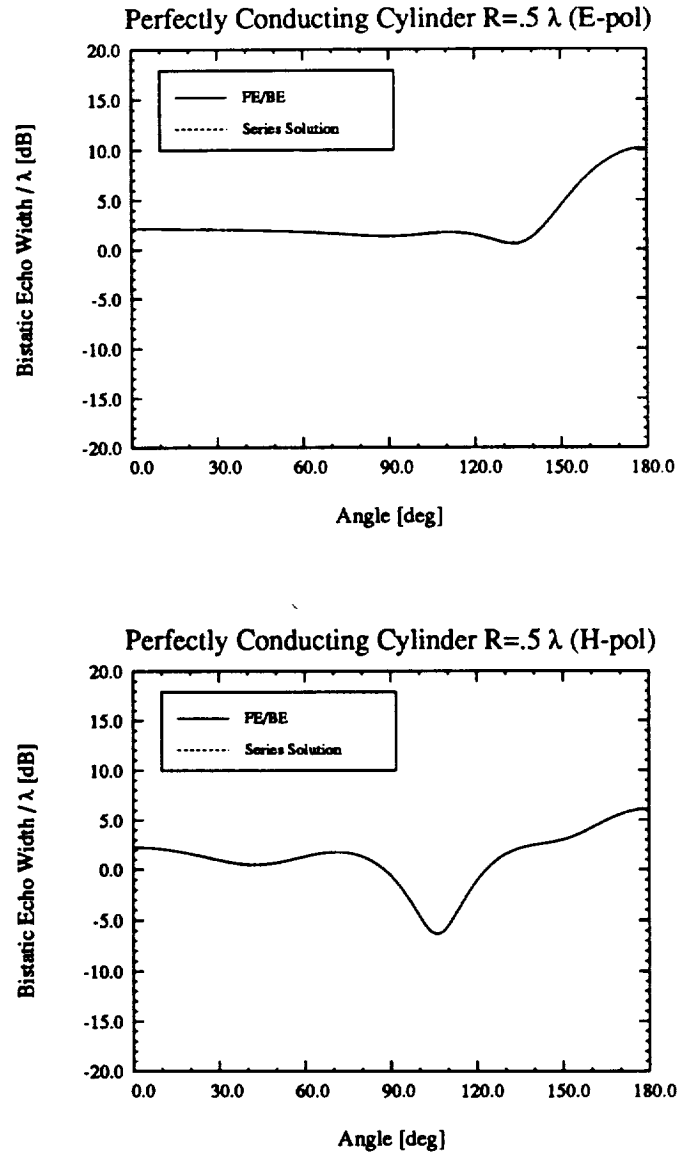
Figure 4.4: E_z and H_z bistatic echowidth of a perfectly conducting circular cylinder of radius 0.5λ
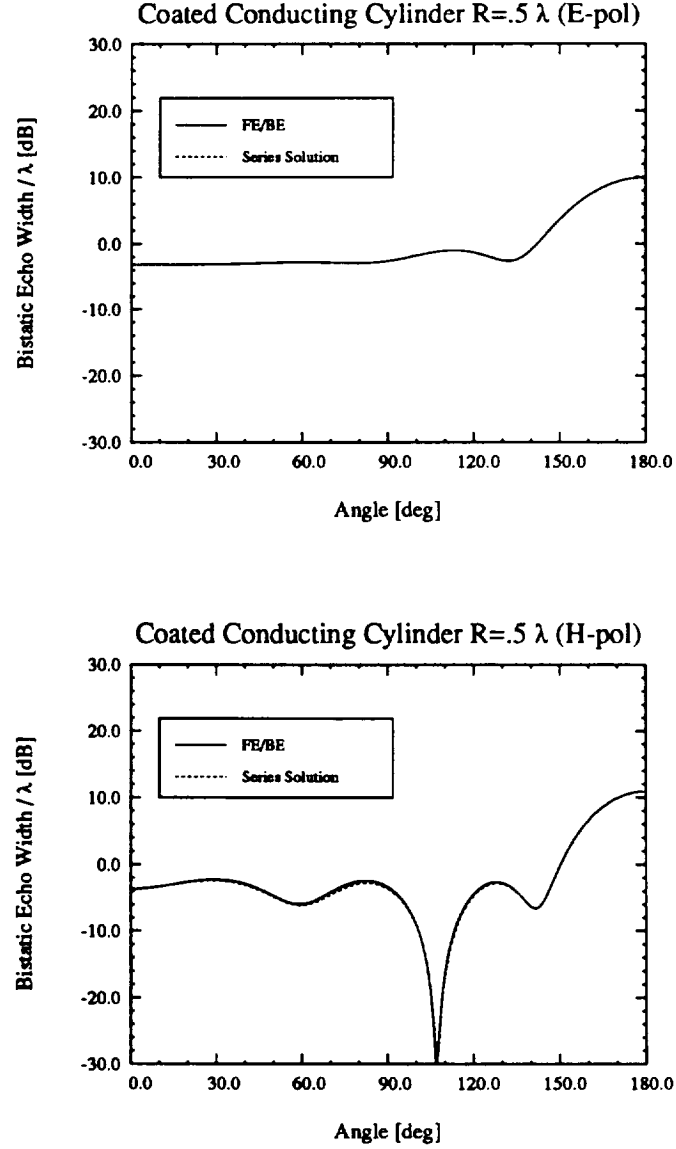
Figure 4.5: E_z and H_z bistatic echowidth of a perfectly conducting circular cylinder with a conductor radius of $.5\lambda$ and a coating thickness of $.05\lambda$ containing material properties $\epsilon_r = 5 - j5$, $\mu_r = 1.5 - j0.5$

Coated Conducting Cylinder R=3 λ (E-pol)

Coated Conducting Cylinder R=3 λ (H-pol)
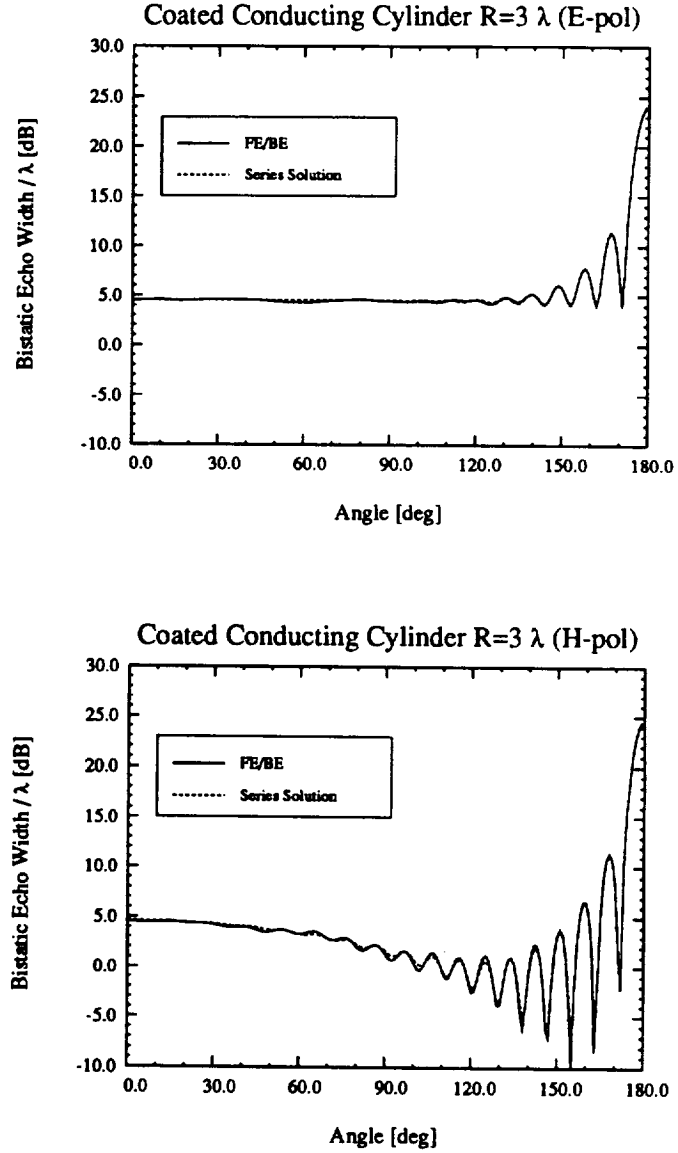
Figure 4.6: E_z and H_z bistatic echowidth of a coated circular cylinder with a conductor radius of 3λ and coating thickness of 0.05λ with material properties $\epsilon_r = 5 - j5$, $\mu_r = 1.5 - j0.5$

.5 x 1.λ PEC Ogive (E-pol)

.5 x 1.λ PEC Ogive (H-pol)
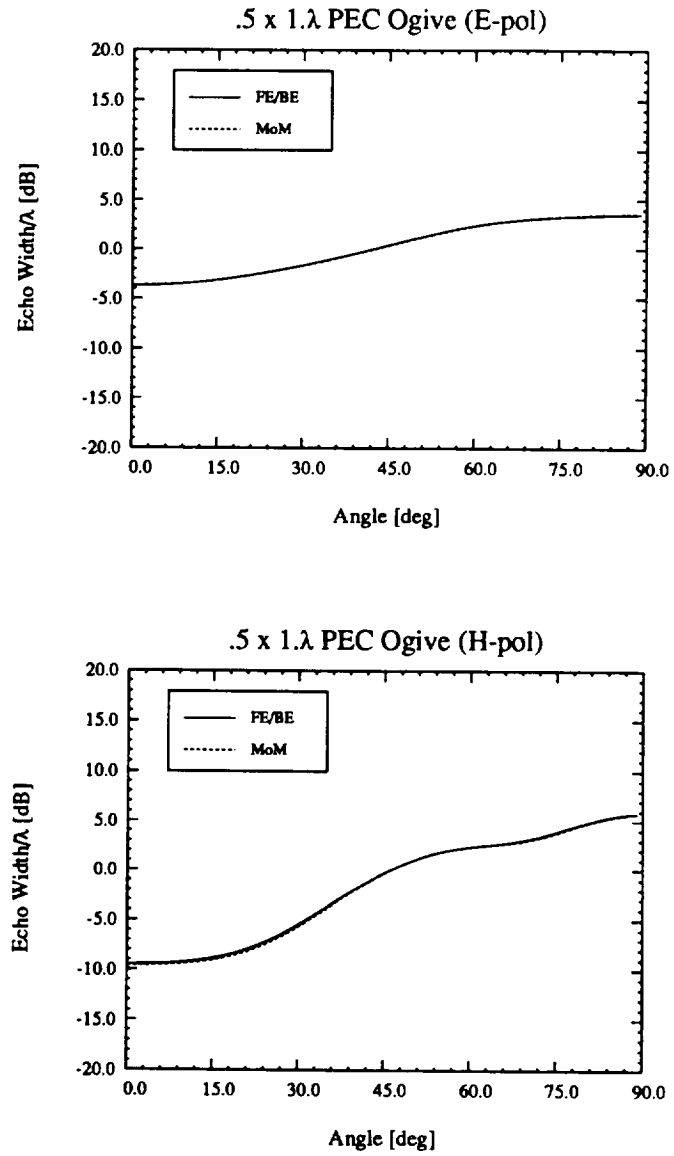
Figure 4.7: E_z and H_z backscatter echowidth of a $0.5 \times 1\lambda$ perfectly conducting ogive

.5 x 1λ Coated Conducting Ogive (E-pol)

.5 x 1λ Coated Conducting Ogive (H-pol)
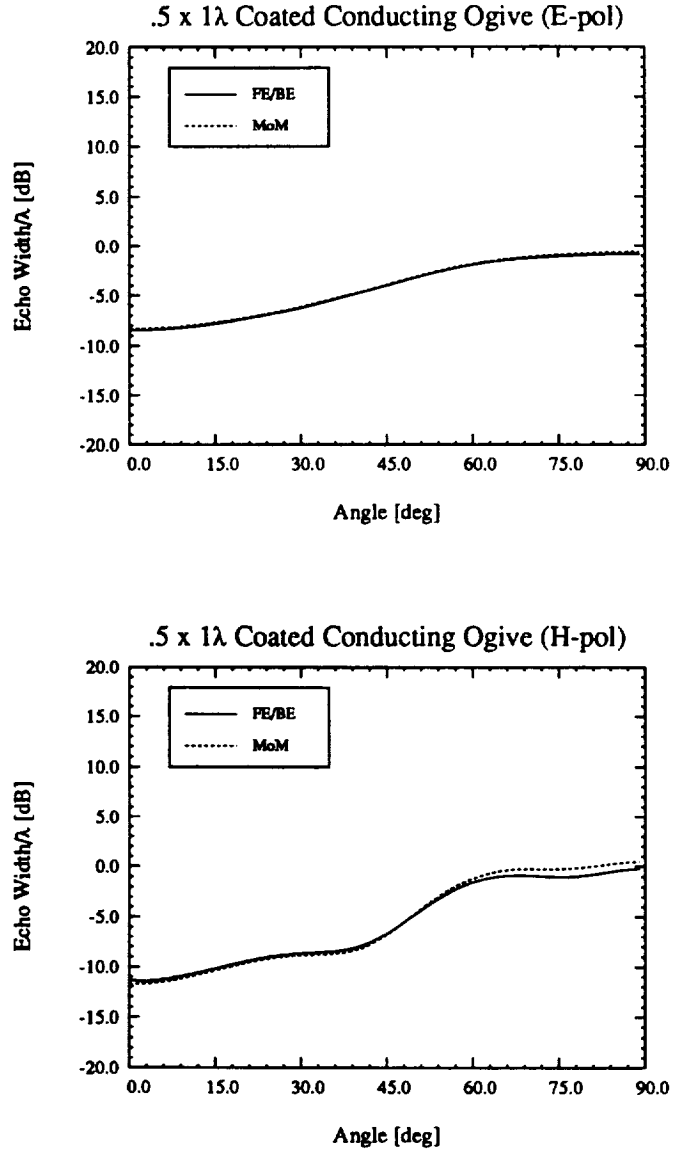
Figure 4.8: E_z and H_z backscatter echowidth of a .5 x 1λ perfectly conducting ogive with a 0.05λ thick material coating containing the properties $\epsilon_r = 3 - j5, \mu_r = 1.5 - j0.5$

1 x 4λ Coated Conducting Ogive (E-pol)

1 x 4λ Coated Conducting Ogive (H-pol)
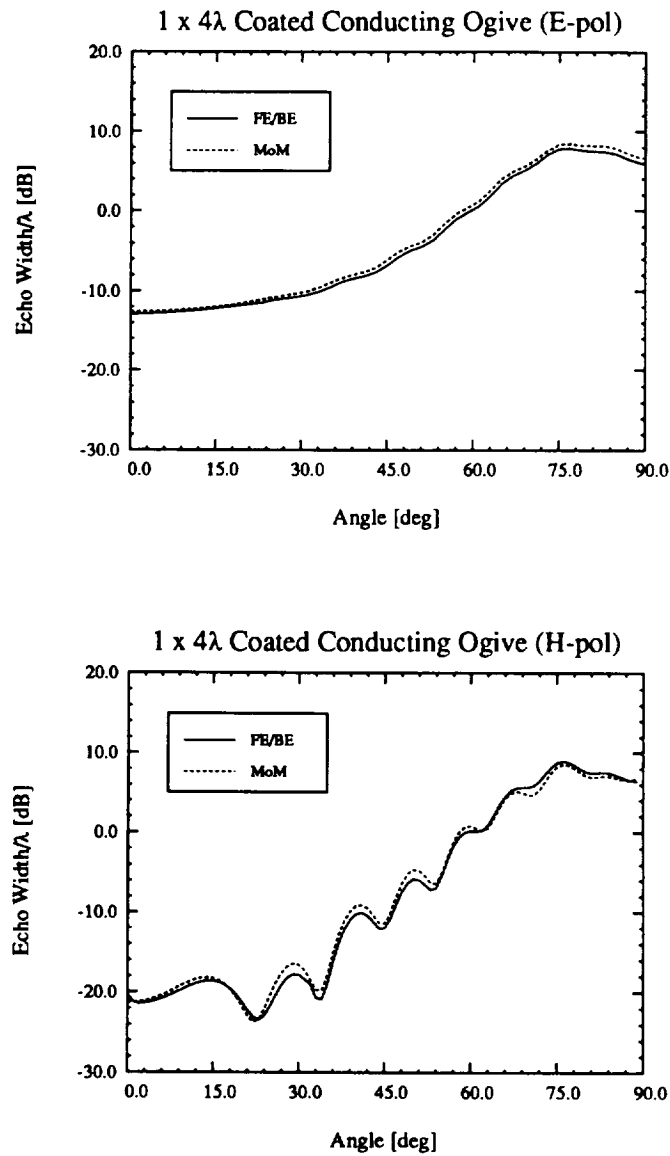
Figure 4.9: E_z and H_z backscatter echowidth of a $1 \times 4\lambda$ perfectly conducting ogive with a $.05\lambda$ thick material coating containing the properties $\epsilon_r = 3 - j5, \mu_r = 1.5 - j0.5$

C-2

4.6 Summary

The scattering from targets surrounded by ogival and circular boundaries has been presented. The finite element method produces the usual sparse sub-matrix, while a discrete version of the boundary integral results in a dense sub-matrix. The mathematical boundary enclosing the scattering structure may be judiciously chosen such that the boundary integrals are convolutional. As a result, they become amenable to evaluation via the FFT and leads to an $O(N)$ storage requirement. Among the circular and ogival boundaries considered, the circular boundary satisfies the above requirements. The ogival boundary results in convolutions only when the source and observation points are along the same arc, while the non-convolutional cross-terms must be stored efficiently to guarantee the required storage requirement. When considering circular and ogival structures, the associated circular and ogival boundaries are usually conformal to the structure, thus providing an additional reduction in the number of unknowns.

To validate the method and associated computer code, scattering patterns of several circular and ogival structures were given and compared with data generated by proven methods.

CHAPTER V

The Elimination of Boundary Integral Interior Resonances in Two-dimensional Finite Element – Boundary Integral Formulations

5.1 Introduction

The interior resonance corruption of boundary integral solutions for scattering computations is well known, and its treatment has been a subject of research for the last two decades. Methods based on the "complexification" of the wavenumber [15], the overspecification of the boundary conditions [16], [17], and the linear combinations of integral equations [18], [19] have been proposed, while others have focused on the solution technique rather than the system formulation [20]. Not surprisingly, when the boundary integral equation is used to terminate the finite element mesh, the interior resonance corruption persists and this has restricted the application of an otherwise promising method for large scale computations of highly inhomogeneous structures.

To demonstrate the seriousness of the problem, Fig. 5.1a shows the backscatter echo width of a circular conducting cylinder of radius a_c for TM plane wave incidence. The mesh is terminated on a circle of radius $a_o = 1.01a_c$ on which the boundary integral equation is applied. The results, displayed as a function of ka_o, were obtained

via the FE–BI described in chapter IV. The unknown in this implementation is the total field, and as seen the solution is severely corrupted, a difficulty which persists for other scatterers as well. (For reference, the locations of the interior resonant frequencies are displayed by the vertical lines at the bottom of the figure.) The corruption is further evidenced in the near zone scattered field plotted in Fig. 5.1b, obtained by subtracting the incident from the total field generated via the aforementioned FE–BI method at $ka_o = 23.586$. To render the FE–BI method robust at all frequencies, it is thus essential to remove the problem associated with the interior resonances. However, employing traditional methods such as those described in [2] – [6] requires either significant modifications to the original FE–BI formulation or substantial computing time, thus affecting the efficiency and performance of the method.

Further, for the "complexification" scheme proposed in [15] to be effective, we verified that three different computations are required for each incident angle when combined with the total field FE–BI system in (4.60). That is, the total field FE–BI solution must be repeated three times with different complex propagation constants, all slightly perturbed from the free space wavenumber. Fig. 5.2, the counterpart to Fig. 5.1, demonstrates how the amplitude of the field quantity varies for $\alpha = 1 - j0.001$ and $\alpha = 1 - j0.005$. In the following section we present a simple modification to the FE–BI formulation which renders it relatively immune to the resonance problem without the need to repeat the solution.

5.2 Method

The proposed approach for eliminating the failure of the FE–BI method at interior resonant frequencies is based on the observation that the specification of the

tangential electric or magnetic field excitation alone at the integration boundary is not sufficient to yield a unique solution [19]. Therefore, we move the excitation away from the integration boundary by employing the scattered field as the working variable. This is accomplished by first writing the total fields everywhere in space as a superposition of the incident field ϕ^i and the scattered field ϕ^s as

$$\phi = \phi^i + \phi^s \qquad (5.1)$$

The boundary integral in (4.5) may be expressed entirely in terms of the scattered field as

$$\phi^s(\overline{p}) = -\oint_{\Gamma_a} \left\{ G(\overline{p}, \overline{p}_a) \left[\frac{\partial}{\partial n_a} \phi^s(\overline{p}_a) \right] - \phi^s(\overline{p}_a) \left[\frac{\partial}{\partial n_a} G(\overline{p}, \overline{p}_a) \right] \right\} dl_a \qquad (5.2)$$

which differs in form from (4.5) by the incident field term. The excitation is instead associated with the finite element portion of the system on conduction surfaces and material interfaces. This becomes clear after substituting (5.1) into (4.10) to obtain

$$\iint_{S^e} \left\{ -u \left[\frac{\partial \phi^s}{\partial x} \frac{\partial W_i^e}{\partial x} + \frac{\partial \phi^s}{\partial y} \frac{\partial W_i^e}{\partial y} \right] + k_0^2 v \phi^s W_i^e \right\} d\Omega^e + \int_{\Gamma^e} W_i^e \psi d\Gamma^e$$

$$= -\iint_{S^e} \left\{ -u \left[\frac{\partial \phi^i}{\partial x} \frac{\partial W_i^e}{\partial x} + \frac{\partial \phi^i}{\partial y} \frac{\partial W_i^e}{\partial y} \right] + k_0^2 v \phi^i W_i^e \right\} d\Omega^e \qquad (5.3)$$

where the quantity ψ has been left in terms of the total field to ensure tangential field continuity between adjacent elements which may contain different materials.

The expressions for TM ($\phi^s = E_z^s$) and TE ($\phi^s = H_z^s$) differ by the application of the boundary condition on perfectly conducting surfaces. For TE incidence, $\psi = 0$ and the contour integral contribution on this portion of the path Γ^e disappears. For TM incidence, the condition $\phi^s = -\phi^i$ is applied after assembly, and this results in the elimination of the associated contour integral. Thus, in following the discretization procedure outlined in section 4.2.1, we obtain the system

$$\sum_{j=1}^{3} a_{ij}^e \{\phi^s\}_j^e - \sum_{k=1}^{3} \sum_{j=1}^{3} b_{ij}^e(k) \{\psi^s\}_j^e = -U_i^e \qquad (5.4)$$

where

$$U_i^e = \iint\limits_{S^e} \left\{ -u \left[\frac{\partial \phi^i}{\partial x} \frac{\partial N_i^e}{\partial x} + \frac{\partial \phi^i}{\partial y} \frac{\partial N_i^e}{\partial y} \right] + k_0^2 v \phi^i N_i^e \right\} d\Omega^e \qquad (5.5)$$

Note that a_{ij}^e and b_{ij}^e are unchanged.

Assembling the final system and applying the appropriate boundary conditions, we have

$$\begin{bmatrix} A_{aa} & A_{aI} & 0 & -B_{aa} \\ A_{Ia} & A_{II} & A_{Id} & 0 \\ 0 & A_{dI} & A_{dd} & 0 \\ M_{aa} & 0 & 0 & -L_{aa} \end{bmatrix} \begin{bmatrix} \phi_a^s \\ \phi_I^s \\ \phi_d^s \\ \psi_a^s \end{bmatrix} = \begin{bmatrix} -U_a \\ -U_I \\ -U_d \\ 0 \end{bmatrix} \qquad (5.6)$$

for TE and

$$\begin{bmatrix} A_{aa} & A_{aI} & 0 & -B_{aa} \\ A_{Ia} & A_{II} & A_{Id} & 0 \\ 0 & 0 & I & 0 \\ M_{aa} & 0 & 0 & -L_{aa} \end{bmatrix} \begin{bmatrix} \phi_a^s \\ \phi_I^s \\ \phi_d^s \\ \psi_a^s \end{bmatrix} = \begin{bmatrix} -U_a \\ -U_I \\ -\phi_d^i \\ 0 \end{bmatrix} \qquad (5.7)$$

for the TM case. Clearly, now, the excitation is present entirely in the FE region of the system, as opposed to the BI portion as was the case in the total field formulation of chapter IV.

The system is then solved with the introduction of a small loss in the propagation constant appearing in the Green's function in (5.2) accomplished by replacing k with αk, where $\alpha = 1 - j\delta$. This substantially improved the convergence of the employed biconjugate gradient solver for the cases considered. However, in contrast to the "complexification" scheme employed with the total field formulation, the scattered field solution in (5.6) and (5.7) is relatively insensitive to δ (provided, of course, δ is very small).

5.3 Results

To demonstrate the effectiveness, efficiency and accuracy of the proposed method, let us reconsider the problem of scattering by a circular cylinder via the scattered field FE–BI formulation. As seen in Fig. 5.3a, the far field is no longer corrupted by the fictitious interior resonances and the same holds for the near zone field as displayed in Fig. 5.3b. The results, shown for $\alpha = 1 - j0.001$ and $\alpha = 1 - j0.005$, are also seen not to deviate from the series solution, although the convergence rate of the solver varied significantly as a function of α. For example, the unperturbed (no complexification, i.e., $\alpha = 1$) scattered field formulation converged in approximately $0.15N$ iterations over the frequency band considered in Fig. 5.3a, where N denotes the unknown count. For $\alpha = 1 - j0.001$, the solution converged in $0.13N$ iterations whereas for $\alpha = 1 - j0.005$, convergence was achieved in approximately $0.08N$ iterations. Note that this fast convergence rate is due in part to the fact that the discrete boundary integral occupies a substantial portion of the total FE–BI system. For complex structures, this may not be the case and the affect is expected to be less pronounced.

Also, we consider the TM illumination of a $5.256\lambda \times 5.256\lambda$ metallic square cylinder. For the implementation of the scattered field FE–BI formulation, the boundary integral was enforced on a circle of radius $a_o = 3.754\lambda$ so that ka_o is the fifth zero of the Bessel function of order 6. With the incident field direction normal to one of rectangle's faces, Fig. 5.4 depicts the corresponding bistatic scattered field obtained via the total and scattered field FE–BI formulation with $\alpha = 1 - j0.005$. Clearly, the pattern based on the scattered field FE–BI formulation agrees everywhere with the moment method data. In contrast, the results based on the total field FE–BI formulation are substantially in error.
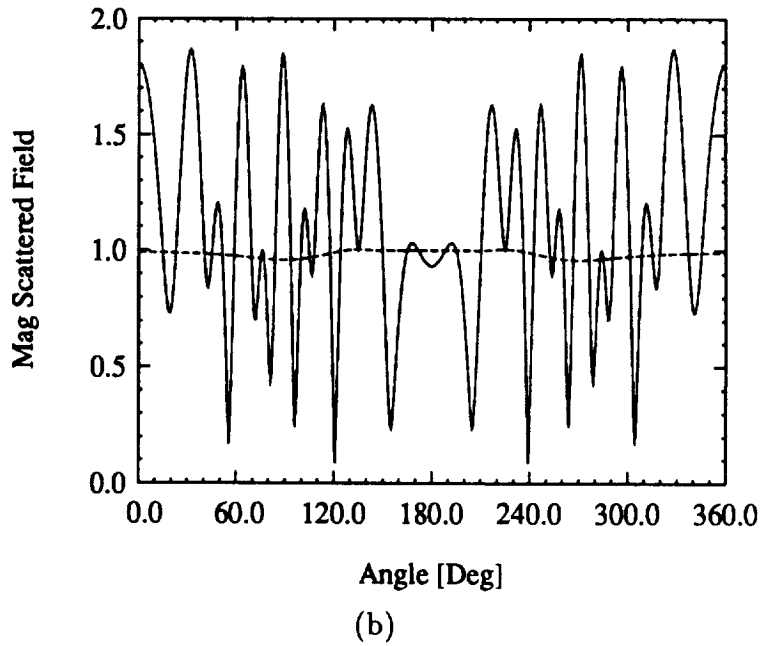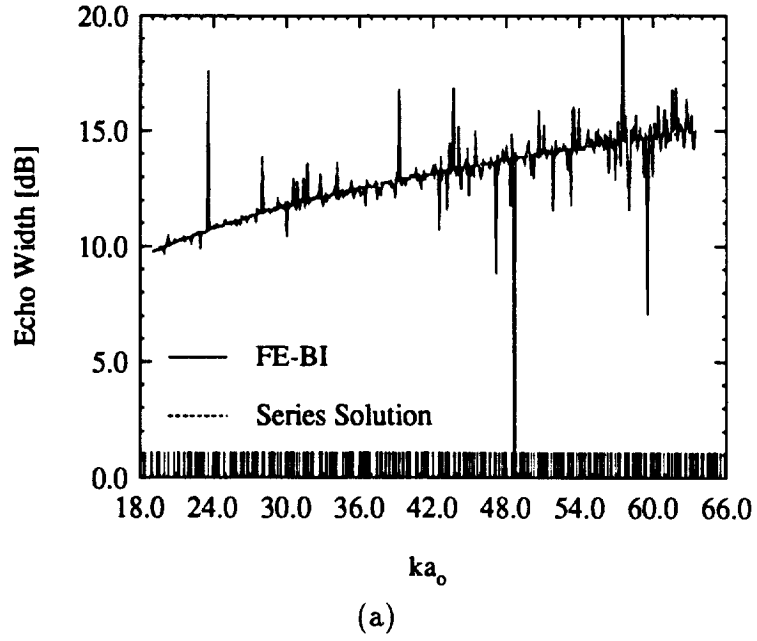
Figure 5.1: Comparison of the far zone and near zone fields for TM plane wave incidence on a circular metallic cylinder as computed by the total field FE–BI method and the eigenfunction series. (a) backscatter echo width vs. ka_o — the lines over the horizontal axis correspond to the eigenvalues of a circular conducting waveguide. (b) magnitude of the TM scattered field on the enclosure at the resonant frequency $ka_o = 23.586$
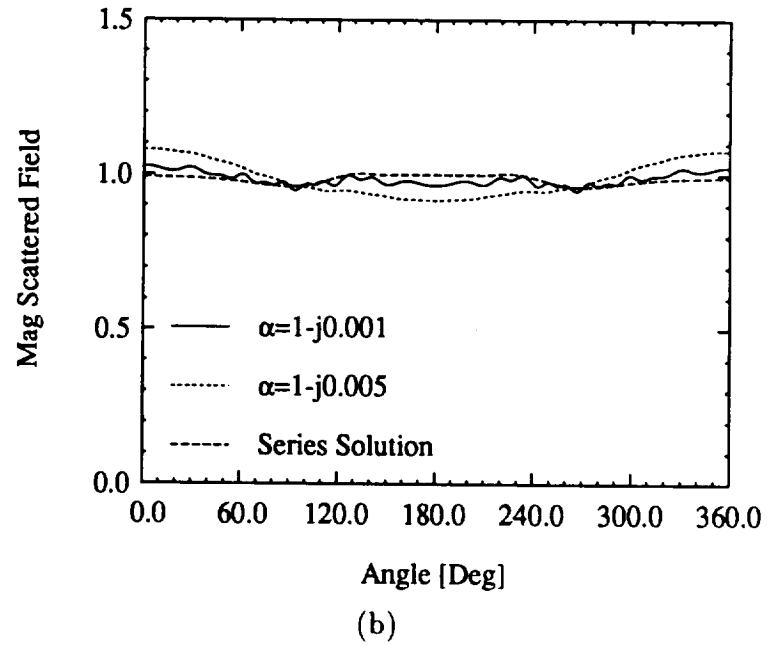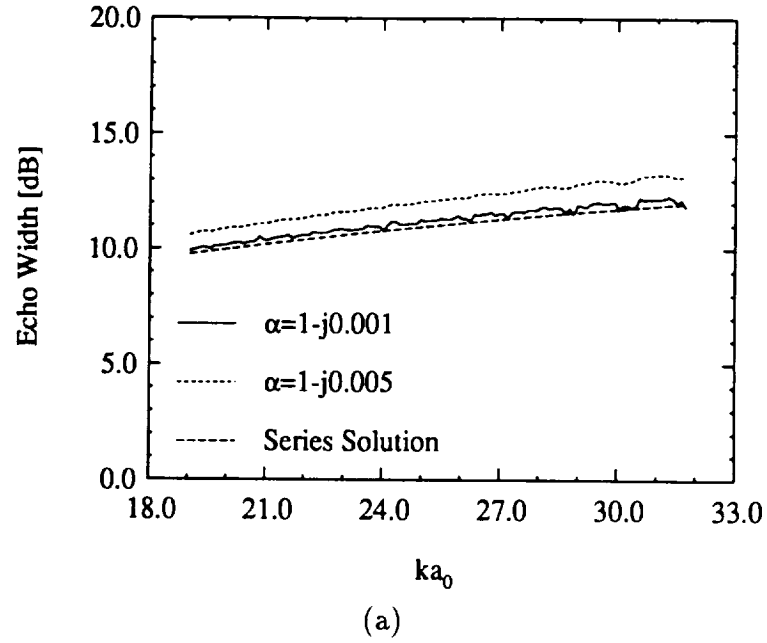
Figure 5.2: Far and near zone fields for TM plane wave incidence on a circular metallic cylinder as computed by the total field FE–BI method with k replaced by $k\alpha$ in the BI equation. (a) backscatter echo width vs. ka_o. (b) magnitude of the TM scattered field on the enclosure at the resonant frequency $ka_o = 23.586$

(a)

(b)
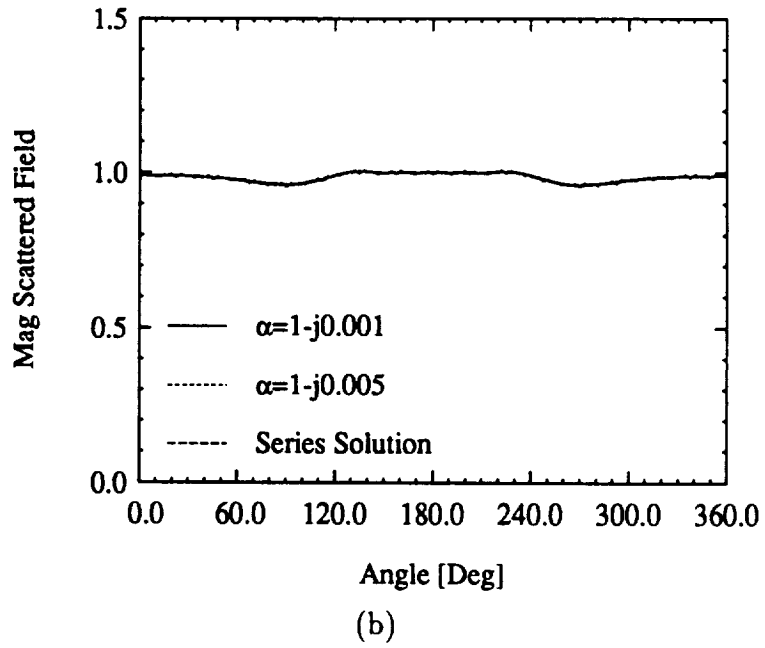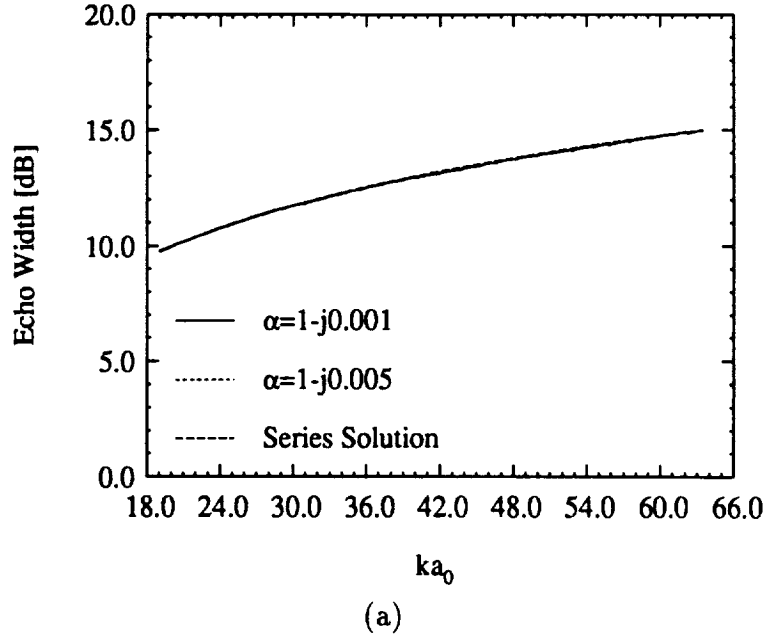
Figure 5.3: Far and near zone fields for TM plane wave incidence on a circular metallic cylinder as computed by the scattered field FE–BI method with k replaced by $k\alpha$ in the BI equation. (a) backscatter echo width vs. ka_o. (b) magnitude of the TM scattered field on the enclosure at the resonant frequency $ka_o = 23.586$
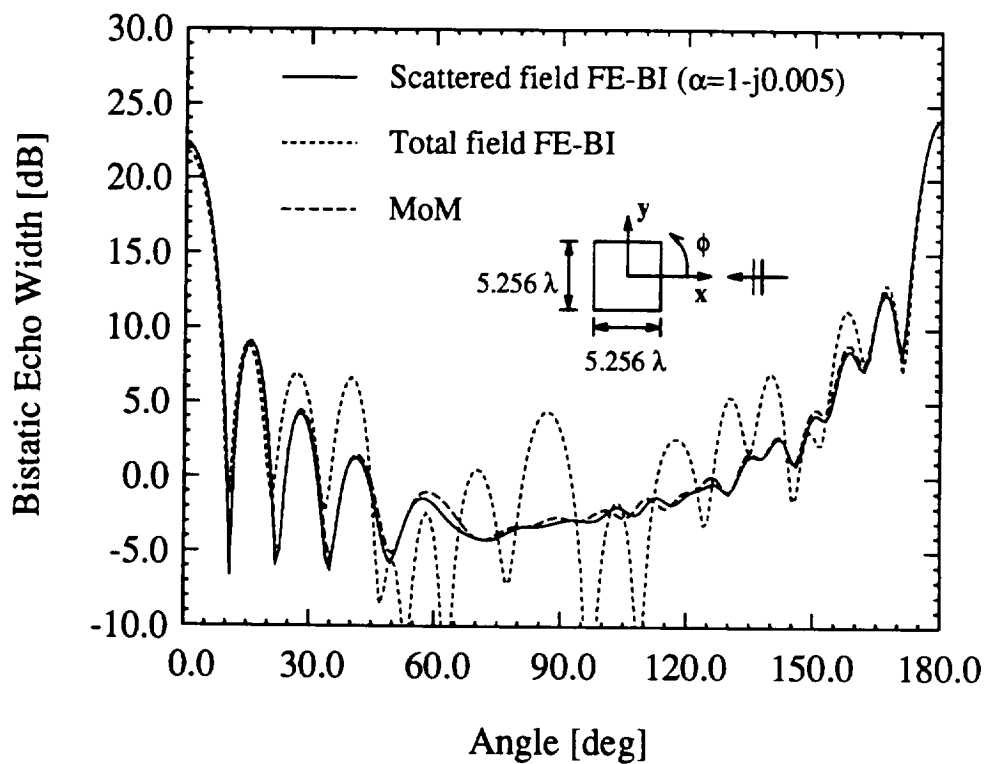
Figure 5.4: Bistatic echo width for TM plane wave incidence on a $5.256\lambda \times 5.256\lambda$ metallic square cylinder with the boundary integral place at a radius $a_o = 3.754\lambda$

5.4 Summary

A method was presented for the elimination of the interior resonance corruption of the boundary integral in the FE–BI formulation. By expressing the system in terms of the scattered field and employing a complex wavenumber in the boundary integral, the effect of resonances were removed. This implementation of the method was shown to be superior to that associated with the total field formulation presented in chapter IV in that only one sample per frequency was needed. Though the development was implemented for the two-dimensional FE–BI formulation, it is applicable to the three-dimensional one as well, as seen in chapter VI.

CHAPTER VI

A Finite Element – Boundary Integral Formulation for Axially Symmetric Structures

6.1 Introduction

A finite element – boundary integral approach is applied to the case of axially symmetric structures. The method follows the same procedure outlined in section 2.2. In this implementation, the coupled potential equations [21] are discretized via the usual finite element method, and the resulting system is augmented by a discrete form of the Stratton-Chu equations [22]. The storage reduction associated with the boundary integral is achieved by exploiting matrix symmetries and the final system is computed by employing a conjugate gradient solver.

In this chapter, the formulation for the FE–BI is described for axially symmetric scatterers. The results presented demonstrates the accuracy of the method along with showing its limitations.

6.2 Finite Element Formulation

In this section, we derive the analytical coupled azimuth potential (CAP) equations [23] which are then discretized via the finite element method. A consequence of the formulation is a line singularity, which tends to corrupt the computed fields
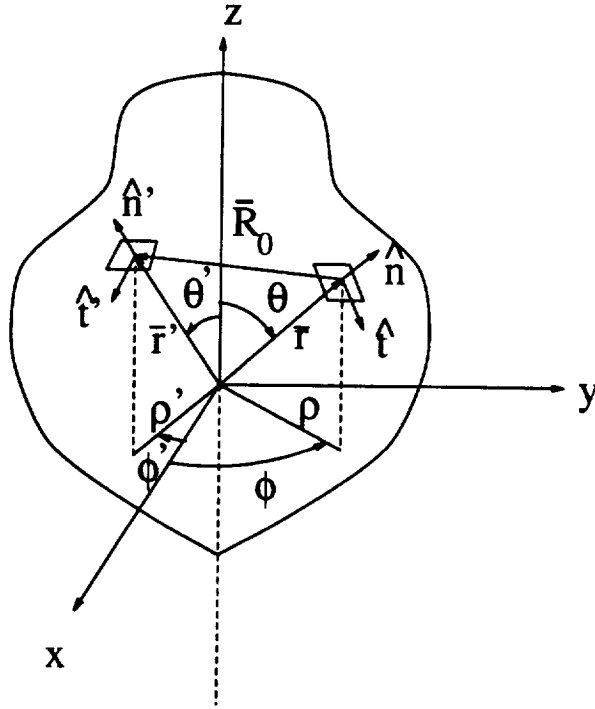
Figure 6.1: The general axially symmetric surface with source (primed) and observation (unprimed) points and the corresponding unit vectors

for scattering domains incorporating lossless media. A regularization approach is suggested for its removal.

6.2.1 Analytic CAP Formulation

Maxwell's equations in a source free region are given by [12]

$$\nabla \times \overline{E}(\overline{r}) = -j\omega\mu\overline{H} \tag{6.1}$$

$$\nabla \times \overline{H}(\overline{r}) = j\omega\epsilon\overline{E} \tag{6.2}$$

$$\nabla \cdot \overline{D}(\overline{r}) = 0 \tag{6.3}$$

$$\nabla \cdot \overline{B}(\overline{r}) = 0 \tag{6.4}$$

For axially symmetric media such as that indicated in Fig. 6.1, the fields may be represented by a Fourier series in the cylindrical coordinate ϕ as

$$\overline{E}(\overline{r}) = \sum_{m=-\infty}^{\infty} \overline{e}_m(\rho, z)e^{jm\phi} \tag{6.5}$$

$$\eta\overline{H}(\overline{r}) = \sum_{m=-\infty}^{\infty} \overline{h}_m(\rho, z)e^{jm\phi} \tag{6.6}$$

where

$$\overline{e}_m(\rho, z) = \frac{1}{2\pi} \int_0^{2\pi} \overline{E}(\overline{r})e^{-jm\phi}d\phi \tag{6.7}$$

$$\overline{h}_m(\rho, z) = \frac{1}{2\pi} \int_0^{2\pi} \eta\overline{H}(\overline{r})e^{-jm\phi}d\phi \tag{6.8}$$

Up substituting (6.5) and (6.6) into (6.1) and (6.2), we obtain

$$\frac{1}{R}\left[jmh_{mz} - \frac{\partial}{\partial Z}(Rh_{m\phi})\right] = j\epsilon_r e_{m\rho} \tag{6.9}$$

$$\frac{1}{R}\left[jme_{mz} - \frac{\partial}{\partial Z}(Re_{m\phi})\right] = -j\mu_r h_{m\rho} \tag{6.10}$$

$$R\left[\frac{\partial}{\partial Z}h_{m\rho} - \frac{\partial}{\partial R}h_{mz}\right] = j\epsilon_r(Re_{m\phi}) \tag{6.11}$$

$$R\left[\frac{\partial}{\partial Z}e_{m\rho} - \frac{\partial}{\partial R}e_{mz}\right] = -j\mu_r(Rh_{m\phi}) \tag{6.12}$$

$$\frac{1}{R}\left[jmh_{m\rho} - \frac{\partial}{\partial R}(Rh_{m\phi})\right] = -j\epsilon_r e_{mz} \tag{6.13}$$

$$\frac{1}{R}\left[jme_{m\rho} - \frac{\partial}{\partial R}(Re_{m\phi})\right] = j\mu_r h_{mz} \tag{6.14}$$

with

$$R = k_0\rho, \quad Z = k_0 z \tag{6.15}$$

to be referred to as normalized coordinates. Substituting h_{mz} of (6.14) into (6.9) gives

$$e_{m\rho} = jf_m\left[m\frac{\partial}{\partial R}(Re_{m\phi}) + R\mu_r\frac{\partial}{\partial Z}(Rh_{m\phi})\right] \tag{6.16}$$

where

$$f_m = \left[R^2\kappa^2 - m^2\right]^{-1} \tag{6.17}$$

and

$$\kappa^2 = \mu_r \epsilon_r \tag{6.18}$$

Analogously, substituting $e_{m\rho}$ of (6.9) into (6.14) yields

$$h_{mz} = jf_m \left[m\frac{\partial}{\partial Z}(Rh_{m\phi}) + R\epsilon_r\frac{\partial}{\partial R}(Re_{m\phi}) \right] \tag{6.19}$$

while a similar procedure for combining (6.10) and (6.13) yields the pair

$$e_{mz} = jf_m \left[m\frac{\partial}{\partial Z}(Re_{m\phi}) - R\mu_r\frac{\partial}{\partial R}(Rh_{m\phi}) \right] \tag{6.20}$$

$$h_{m\rho} = jf_m \left[m\frac{\partial}{\partial R}(Rh_{m\phi}) - R\epsilon_r\frac{\partial}{\partial Z}(Re_{m\phi}) \right] \tag{6.21}$$

Equations (6.16) through (6.21) may be expressed in compact form as

$$\hat{\phi} \times \overline{e}_m(R, Z) = jf_m \left[m\hat{\phi} \times \nabla_t\psi_e - \mu_r R\nabla_t\psi_h \right] \tag{6.22}$$

$$\hat{\phi} \times \overline{h}_m(R, Z) = jf_m \left[m\hat{\phi} \times \nabla_t\psi_h + \epsilon_r R\nabla_t\psi_e \right] \tag{6.23}$$

$$\hat{\phi} \cdot \overline{e}_m(R, Z) = \psi_e/R \tag{6.24}$$

$$\hat{\phi} \cdot \overline{h}_m(R, Z) = \psi_h/R \tag{6.25}$$

where

$$\nabla_t = \hat{\rho}\frac{\partial}{\partial R} + \hat{z}\frac{\partial}{\partial Z} \tag{6.26}$$

and ψ_e and ψ_h are herein referred to as the azimuthal potentials. Rewriting (6.11) and (6.12) as

$$R\nabla_t \cdot (\hat{\phi} \times \overline{h}_m) = -j\epsilon_r\psi_e \tag{6.27}$$

$$R\nabla_t \cdot (\hat{\phi} \times \overline{e}_m) = j\mu_r\psi_h \tag{6.28}$$

and then substituting (6.22) and (6.23) into them produces the CAP equations

$$\nabla_t \cdot \left[f_m(\epsilon_r R\nabla_t\psi_e + m\hat{\phi} \times \nabla_t\psi_h) \right] + \frac{\epsilon_r\psi_e}{R} = 0 \tag{6.29}$$

$$\nabla_t \cdot \left[f_m(\mu_r R\nabla_t\psi_h - m\hat{\phi} \times \nabla_t\psi_e) \right] + \frac{\mu_r\psi_h}{R} = 0. \tag{6.30}$$

This system may be written in operator form as

$$L\psi = 0 \tag{6.31}$$

where

$$L = \begin{bmatrix} \nabla_t \cdot [f_m \epsilon_r R \nabla_t] + \frac{\epsilon_r}{R} & m\nabla_t \cdot [f_m \hat{\phi} \times \nabla_t] \\ -m\nabla_t \cdot [f_m \hat{\phi} \times \nabla_t] & \nabla_t \cdot [f_m \mu_r R \nabla_t] + \frac{\mu_r}{R} \end{bmatrix} \tag{6.32}$$

and

$$\psi = [\psi_e \quad \psi_h]^T \tag{6.33}$$

The three dimensional axially symmetric problem has, thus, been cast into a two-dimensional one and its discrete representation is formulated in the following section.

6.2.2 Discretization of the CAP Equations

To discretize (6.31), we first enclose the generating contours of BOR in a fictitious boundary Γ ($= \Gamma_a + \Gamma_c + \Gamma_z$) as shown in Fig. 6.2. The region interior to Γ is divided into N_e triangular elements and within each element the corresponding weighted residual expression is

$$\iint_{S^e} N_i^e(R, Z) \ L\psi \ dS^e = 0 \tag{6.34}$$

where N_i^e is the usual shape function [5], so chosen to satisfy the Dirichlet boundary condition of ψ_e and ψ_h on Γ_z. Substituting the first of (6.31) into (6.34) gives

$$\iint_{S^e} N_i^e \left\{ \nabla_t \cdot \left[f_m(\epsilon_r R \nabla_t \psi_e + m\hat{\phi} \times \nabla_t \psi_h] + \frac{\epsilon_r \psi_e}{R} \right\} dS^e = 0 \tag{6.35}$$

and upon employing the identity

$$N_i^e \nabla_t \cdot \overline{A}^s = \nabla_t \cdot (N_i^e \overline{A}^s) - \overline{A}^s \cdot \nabla_t N_i^e \tag{6.36}$$
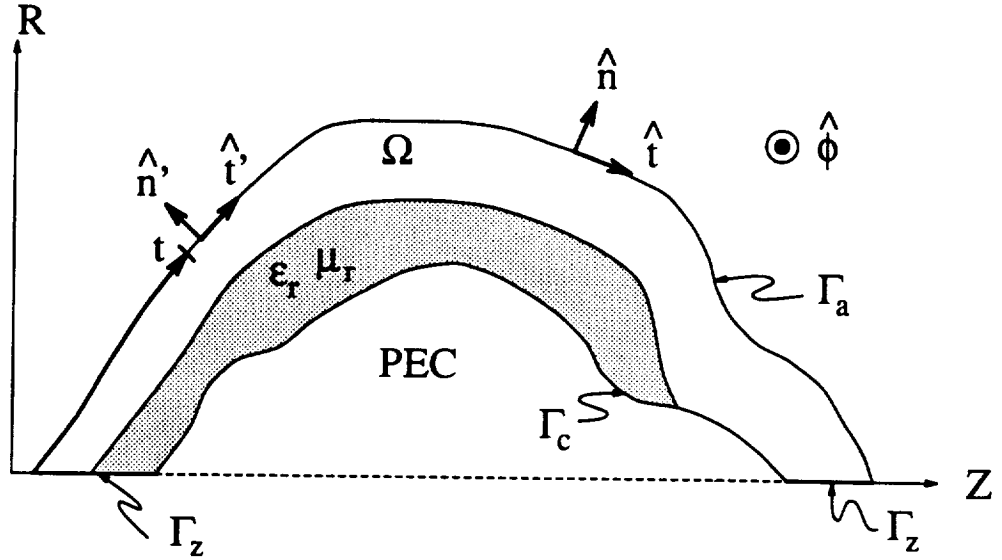
Figure 6.2: Cross section of a generating surface enclosed by the fictitious boundary Γ

gives the expression

$$\iint_{S^e} \left[\nabla_t \cdot \left\{ N_i^e f_m \left(\epsilon_r R \nabla_t \psi_e + m\hat{\phi} \times \nabla_t \psi_h \right) \right\} \right.$$
$$\left. - f_m \left(\epsilon_r R \nabla_t \psi_e + m\hat{\phi} \times \nabla_t \psi_h \right) + \frac{\epsilon_r \psi_e N_i^e}{R} \cdot \nabla_t N_i^e \right] dS^e = 0 \quad (6.37)$$

Furthermore, by invoking the divergence theorem, (6.37) may be written

$$\iint_{S^e} \left\{ \left[-f_m \left(\epsilon_r R \nabla_t \psi_e + m\hat{\phi} \times \nabla_t \psi_h \right) \right] \cdot \nabla_t N_i^e + \frac{\epsilon_r \psi_e N_i^e}{R} \right\} dS^e$$
$$+ \oint_{C^e} \hat{n} \cdot \left[N_i^e f_m \left(\epsilon_r R \nabla_t \psi_e + m\hat{\phi} \times \nabla_t \psi_h \right) \right] dl^e = 0 \quad (6.38)$$

where $\hat{n}$ is the outward normal along the boundary C^e of the eth element. Finally, on using (6.22) these may be simplified, yielding

$$\iint_{S^e} \left\{ \left[-f_m \left(\epsilon_r R \nabla_t \psi_e + m\hat{\phi} \times \nabla_t \psi_h \right) \right] \cdot \nabla_t N_i^e + \frac{\epsilon_r \psi_e N_i^e}{R} \right\} dS^e$$
$$- \oint_{C^e} N_i^e (j h_{mt}) dl^e = 0 \quad (6.39)$$

where

$$h_{mt} = \hat{t} \cdot \overline{h}_m \qquad (6.40)$$

with

$$\hat{t} = \hat{n} \times \hat{\phi} \qquad (6.41)$$

Equation (6.39) and its dual constitute a weak form of (6.31) over the eth element.

The development thus far has employed the total potential as the working variable, but may also be expressed in terms of the scattered potential as well. To this end, any function ψ satisfying Maxwell's equations may be written as a superposition of the incident and scattered potentials, i.e.,

$$\psi_e = \psi_e^i + \psi_e^s \qquad (6.42)$$

$$\psi_h = \psi_h^i + \psi_h^s \qquad (6.43)$$

where the superscript s denotes the scattered potential and i denotes the incident potential (i.e., that potential present in the absence of the scatter). Substituting these into (6.39), the corresponding expression in terms of the scattered potential is

$$\iint\limits_{S^e} \left\{ \left[-f_m \left(\epsilon_r R \nabla_t \psi_e^s + m\hat{\phi} \times \nabla_t \psi_h^s \right) \right] \cdot \nabla_t N_i^e + \frac{\epsilon_r \psi_e^s N_i^e}{R} \right\} dS^e$$

$$- \oint_{C^e} N_i^e (j h_{mt}) dl^e =$$

$$- \iint\limits_{S^e} \left\{ \left[-f_m \left(\epsilon_r R \nabla_t \psi_e^i + m\hat{\phi} \times \nabla_t \psi_h^i \right) \right] \cdot \nabla_t N_i^e + \frac{\epsilon_r \psi_e^i N_i^e}{R} \right\} dS^e \qquad (6.44)$$

where the contour integral has been left in terms of the total field until the final system assembly (of equations) is performed.

To form a discrete system of equations, the potentials in the e element are expressed as

$$\psi_e^s(R, Z) = \sum_{j=1}^{3} N_j^e(R, Z) \{\psi_e^s\}_j^e \qquad (6.45)$$

$$\psi_h^s(R,Z) = \sum_{j=1}^{3} N_j^e(R,Z) \, \{\psi_h^s\}_j^e \tag{6.46}$$

and upon substituting these into (6.44) gives

$$\sum_{j=1}^{3} \left[\iint_{S^e} \left\{ \left[-f_m \epsilon_r R \nabla_t N_i^e \cdot \nabla_t N_j^e + \epsilon_r \frac{N_i^e N_j^e}{R} \right] \{\psi_e^s\}_j^e \right. \right.$$
$$\left. \left. -m f_m \hat{\phi} \times \nabla_t N_j^e \cdot \nabla_t N_i^e \{\psi_h^s\}_j^e \right\} dS^e \right]$$
$$- \oint_{C^e} N_i^e (j h_{mt}) dl^e = \{U\}_i^e \tag{6.47}$$

where $\{U\}_i^e$ is given below. Assuming ϵ_r and μ_r are constant within the element, (6.47) may be written as

$$\sum_{j=1}^{3} \left[\epsilon_r^e \, [a]_{ij}^e \, \{\psi_e^s\}_j^e - [b]_{ij}^e \, \{\psi_h^s\}_j^e \right] = \oint_{C^e} N_i^e \, (j h_{mt}) dl^e + \{U\}_i^e \tag{6.48}$$

where

$$[a]_{ij}^e = \iint_{S^e} \left[-f_m \, R \, \nabla_t N_i^e \cdot \nabla_t N_j^e + \frac{N_i^e N_j^e}{R} \right] dS^e \tag{6.49}$$

$$[b]_{ij}^e = \iint_{S^e} m f_m \hat{\phi} \times \nabla_t N_j^e \cdot \nabla_t N_i^e \, dS^e \tag{6.50}$$

$$\{U\}_i^e = -\iint_{S^e} \left\{ \left[-f_m \left(\epsilon_r \, R \, \nabla_t \psi_e^i + m \hat{\phi} \times \nabla_t \psi_h^i \right) \right] \cdot \nabla_t N_i^e + \frac{\epsilon_r \psi_e^i N_i^e}{R} \right\} dS^e \tag{6.51}$$

These constitute the equations for the eth element, and the final system is assembled by summing over all elements in the discrete model.

Before pursuing the step of system assembly, explicit expressions for (6.49) and (6.50) may be developed by first writing them as

$$[a]_{ij}^e = -\frac{(\beta_i^e \beta_j^e + \gamma_i^e \gamma_j^e)}{(2\Omega^e)^2} I_1 + \iint_{S^e} \frac{N_i^e N_j^e}{R} dS^e \tag{6.52}$$

and

$$[b]_{ij}^e = -m \frac{(\beta_i^e \gamma_j^e - \beta_j^e \gamma_i^e)}{(2\Omega^e)^2} I_0 \tag{6.53}$$

where the linear shape function and its coefficients are given by

$$N_i^e(R, Z) = \frac{\alpha_i^e + \beta_i^e Z + \gamma_i^e R}{2\Omega^e} \tag{6.54}$$

$$\alpha_i^e = Z_{i+1}^e R_{i+2}^e - Z_{i+2}^e R_{i+1}^e \tag{6.55}$$

$$\beta_i^e = R_{i+1}^e - R_{i+2}^e \tag{6.56}$$

$$\gamma_i^e = Z_{i+2}^e - Z_{i+1}^e \tag{6.57}$$

and

$$I_1 = \iint_{S^e} \frac{R}{\kappa^2 R^2 - m^2} dS^e \tag{6.58}$$

$$I_0 = \iint_{S^e} \frac{1}{\kappa^2 R^2 - m^2} dS^e \tag{6.59}$$

Evaluating (6.58) and (6.59) over a triangular element yields

$$I_1 = -\frac{\Omega^e}{\kappa} \sum_{i=1}^{3} [\mathcal{I}_i^e(m) + \mathcal{I}_i^e(-m)] \tag{6.60}$$

$$I_0 = \frac{\Omega^e}{m} \sum_{i=1}^{3} [\mathcal{I}_i^e(m) - \mathcal{I}_i^e(-m)] \tag{6.61}$$

with

$$\mathcal{I}_i^e(m) = \frac{(\kappa R_i^e + m) \log(\kappa R_i^e + m)}{\beta_{i+1}^e \beta_{i+2}^e} \tag{6.62}$$

The second integral in $[a]_{ij}^e$ may be computed numerically via gaussian integration. The sums appearing in I_0 and I_1, however, experience problems when an element edge is parallel or nearly parallel to the axis of revolution (i.e., element d in Fig. 6.3). In this case, two of the three terms have denominators which are nearly zero, resulting in cancellation errors upon their summation. To avoid such errors, the sum of two consecutive terms, i.e., $\mathcal{I}_i^e + \mathcal{I}_{i+1}^e$, is carried out by first expanding the numerator of either term $\mathcal{I}$ and then performing the addition analytically. In this way the offending term is canceled and the final result is well behaved.
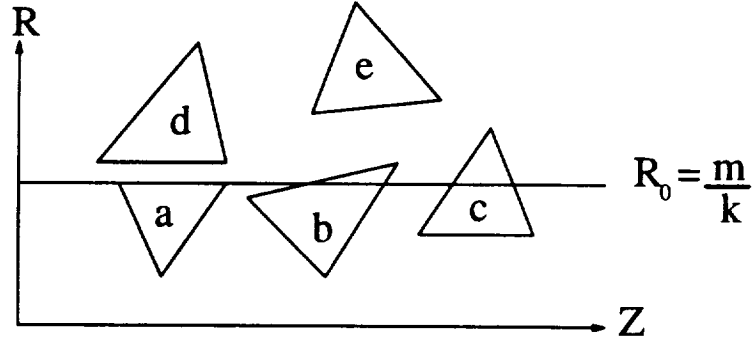
Figure 6.3: Typical triangular elements in the vicinity of the line singularity at $R_0 = \frac{m}{\kappa}$ for real κ

Proceeding then, we note that the Taylor series expansion of $x \ln x$ about x_0 is

$$x \ln x = x \ln x_0 + (x - x_0) \left[1 + S(\frac{x - x_0}{x_0}) \right] \tag{6.63}$$

where

$$S(y) = \sum_{n=1}^{\infty} \frac{(-1)^{n+1}}{n(n+1)} \, y^n \tag{6.64}$$

and the sum converges when $|x - x_0| < \mathcal{R}$, where $\mathcal{R}$ is the radius of a circle centered at x_0 in the complex x-plane for which $x \ln x$ is analytic [24]. The series may be truncated in N terms when the error, given by the ratio of the Nth term to the first term in the series is less than some tolerance ϵ, or more explicitly when

$$\left| \frac{2y^{N-1}}{N(N+1)} \right| < \epsilon \tag{6.65}$$

For $\epsilon = 10^{-7}$, a fit to the nonlinear function in (6.65) for $|y| \in [0.1, 0.7]$ is

$$N(y) = \text{Round}(e^{|y|}(9.97633e^{|y|} - 5.94387)) \tag{6.66}$$

Once N is known, the series is evaluated efficiently using Horner's rule.

Employing the expansion (6.63) to the partial sum $\mathcal{I}_i(m) + \mathcal{I}_{i+1}(m)$ yields

$$\mathcal{I}_i(m) + \mathcal{I}_{i+1}(m) = \begin{cases} \frac{1}{\kappa \beta_{i+1}^e} \left[\frac{(\kappa R_{i+2} + m) \ln(\kappa R_{i+1} + m)}{\kappa \beta_i^e} - 1 - S(\frac{\kappa \beta_{i+2}^e}{\kappa R_{i+1} + m}) \right] & \text{form 1} \\ \frac{1}{\kappa \beta_i^e} \left[\frac{(\kappa R_{i+2} + m) \ln(\kappa R_i + m)}{\kappa \beta_{i+1}^e} + 1 + S(\frac{-\kappa \beta_{i+2}^e}{\kappa R_i + m}) \right] & \text{form 2} \end{cases} \tag{6.67}$$

where form 1 was obtained by expanding the numerator of $\mathcal{I}_i(m)$ about R_{i+1}, while form 2 results by expanding the numerator of $\mathcal{I}_{i+1}(m)$ about R_i. For elements well away from the line singularity, either form is valid. However, as $\kappa R + m \to 0$, the radius of convergence $\mathcal{R}$ is reduced to zero due the branch point of $(\kappa R + m)\ln(\kappa R + m)$. The method for choosing the appropriate form may be done numerically by computing the value argument of S in (6.67) for each form. The one which gives the smallest value $y \in [0.1, 0.7]$ in $S(y)$ is chosen for computation, since the series will converge the fastest for it. If y falls in the range $0.7 < y < 1$, the series (6.64) will still converge, but very slowly as y approaches 1. If $|y| > 1$, the series will not converge and the associated form (1 or 2, or both) will be invalid. Note that neither of them is valid if both points lie along the line singularity (in which an infinite result is obtained) or if one lies above it and the other below (as in element b of Fig. 6.3). In the latter case, (6.60) and (6.61) must be evaluated directly, but a new mesh may be necessary for the former. An approach for bypassing this difficulty is discussed in the following section.

Summing over all elements to obtain a solution for the entire computational domain Ω, our system becomes

$$\sum_{e=1}^{N_e}\sum_{j=1}^{3}\left[\epsilon_r^e \, a_{ij}^e \, \{\psi_e^s\}_j^e - b_{ij}^e \, \{\psi_h^s\}_j^e\right] = \sum_{e=1}^{N_e}\int_{\Gamma_a} N_i^e \, (jh_{mt})dl + \sum_{e=1}^{N_e}\int_{\Gamma_z} N_i^e \, (jh_{mt})dl$$
$$+ \sum_{e=1}^{N_e}\int_{\Gamma_c} N_i^e \, (jh_{mt})dl + \sum_{e=1}^{N_e}\{U\}_j^e \qquad (6.68)$$

Note that since N_i^e and h_{mt} are individually continuous between adjacent elements (and the same is true for their product), the contour integrals cancel everywhere except on the domain boundary Γ. Accounting for $N_i^e = 0$ along the z-axis, this

system combined with its dual may be written in block matrix form as

$$
\begin{bmatrix}
A^\epsilon_{aa} & 0 & A^\epsilon_{aI} & -B_{aa} & 0 & -B_{aI} \\
0 & A^\epsilon_{cc} & A^\epsilon_{cI} & 0 & -B_{cc} & -B_{cI} \\
A^\epsilon_{Ia} & A^\epsilon_{Ic} & A^\epsilon_{II} & -B_{Ia} & -B_{Ic} & -B_{II} \\
B_{aa} & 0 & B_{aI} & A^\mu_{aa} & 0 & A^\mu_{aI} \\
0 & B_{cc} & B_{cI} & 0 & A^\mu_{cc} & A^\mu_{cI} \\
B_{Ia} & B_{Ic} & B_{II} & A^\mu_{Ia} & A^\mu_{Ic} & A^\mu_{II}
\end{bmatrix}
\begin{bmatrix}
\{\psi^s_e\}_a \\
\{\psi^s_e\}_c \\
\{\psi^s_e\}_I \\
\{\psi^s_h\}_a \\
\{\psi^s_h\}_c \\
\{\psi^s_h\}_I
\end{bmatrix}
=
\begin{bmatrix}
\{U\}_a \\
\{U\}_c \\
\{U\}_I \\
\{V\}_a \\
\{V\}_c \\
\{V\}_I
\end{bmatrix}
$$

$$
+ \left[\sum_{e=1}^{N_e} \int_{\Gamma_a} j N^e_i \, h_{mt} \, dl \quad 0 \quad 0 \quad -\sum_{e=1}^{N_e} \int_{\Gamma_a} j N^e_i \, e_{mt} \, dl \quad 0 \quad 0 \right]^T
$$

$$
+ \left[0 \quad \sum_{e=1}^{N_e} \int_{\Gamma_c} j N^e_i \, h_{mt} \, dl \quad 0 \quad 0 \quad -\sum_{e=1}^{N_e} \int_{\Gamma_c} j N^e_i \, e_{mt} \, dl \quad 0 \right]^T
$$

$$
(6.69)
$$

where

$$
[A^\epsilon]_{kl} = \sum_{e=1}^{N_e} \epsilon^e_r \, [a]^e_{kl} \tag{6.70}
$$

$$
[A^\mu]_{kl} = \sum_{e=1}^{N_e} \mu^e_r \, [a]^e_{kl} \tag{6.71}
$$

$$
[B]_{kl} = \sum_{e=1}^{N_e} [b]^e_{kl} \tag{6.72}
$$

$$
U_k = \sum_{e=1}^{N_e} \{U\}^e_k \tag{6.73}
$$

where the ijth member of the eth local element matrix is related to the klth member of the global matrix by a node-element connectivity transformation function p as

$$
k = p(e, i) \tag{6.74}
$$

$$
l = p(e, j) \tag{6.75}
$$

In (6.69) the subscript I refers to group of nodes in region the Ω excluding Γ, and the subscripts on $A^{\epsilon,\mu}$, B, U and V refer to the various regions of Ω and its boundary.

For example, A_{Ic} refers to the matrix resulting from the interactions between nodes in region Ω and on Γ_c, whereas A_{cc} refers to the matrix resulting from the interaction of the nodes on Γ_c. Each matrix is sparse, having nonzero elements when the nodes share a common element. Note also that V is the dual of U, which was defined in (6.51).

Two options exist at this point for evaluating the contour integrals. They may either remain on the excitation side and the tangential modal fields expressed in terms of a condition on Γ_a, or the tangential fields may be expressed as unknown scattered potentials and moved into the matrix. The second is required for the FE–BI formulation and is given by

$$
\begin{bmatrix}
A_{aa}^\epsilon & 0 & A_{aI}^\epsilon & -B_{aa} & 0 & -B_{aI} & 0 & -C_{aa} \\
0 & I & 0 & 0 & 0 & 0 & C_{aa} & 0 \\
A_{Ia}^\epsilon & A_{Ic}^\epsilon & A_{II}^\epsilon & -B_{Ia} & -B_{Ic} & -B_{II} & 0 & 0 \\
B_{aa} & 0 & B_{aI} & A_{aa}^\mu & 0 & A_{aI}^\mu & 0 & 0 \\
0 & B_{cc} & B_{cI} & 0 & A_{cc}^\mu & A_{cI}^\mu & 0 & 0 \\
B_{Ia} & B_{Ic} & B_{II} & A_{Ia}^\mu & A_{Ic}^\mu & A_{II}^\mu & 0 & 0
\end{bmatrix}
\begin{bmatrix}
\{\psi_e^s\}_a \\
\{\psi_e^s\}_c \\
\{\psi_e^s\}_I \\
\{\psi_h^s\}_a \\
\{\psi_h^s\}_c \\
\{\psi_h^s\}_I \\
\{\psi_{et}^s\}_a \\
\{\psi_{ht}^s\}_c
\end{bmatrix}
=
\begin{bmatrix}
\{U\}_a \\
-\{\psi_e^i\}_c \\
\{U\}_I \\
\{V\}_a \\
\{V\}_c \\
\{V\}_I
\end{bmatrix}
$$

$$
+ \begin{bmatrix} \sum_{e=1}^{N_e} \int_{\Gamma_a} N_i^e (j h_{mt}^i) dl & 0 & 0 & -\sum_{e=1}^{N_e} \int_{\Gamma_a} N_i^e (j e_{mt}^i) dl & 0 & 0 \end{bmatrix}^T
$$

$$(6.76)$$

where the boundary conditions $\psi_e = 0$ and $e_{mt} = 0$ on Γ_c were also enforced. Additionally,

$$
[C]_{kl} = \sum_{e=1}^{N_e} \int_{\Gamma_a} \frac{N_k^e N_l^e}{R} dl^e
$$

$$(6.77)$$

and

$$\psi_{et}^{s} = jRe_{mt}^{s} = \sum_{j=1}^{3} N_j^e \{\psi_{et}^{s}\}_j^e \tag{6.78}$$

$$\psi_{ht}^{s} = jRh_{mt}^{s} = \sum_{j=1}^{3} N_j^e \{\psi_{ht}^{s}\}_j^e \tag{6.79}$$

This form is now suited to augmentation by either a discrete form of a boundary integral equation explored in section 6.3.

6.2.3 An Improvement to the Finite Element Formulation

The integrand of each of $[a]_{ij}^e$ and $[b]_{ij}^e$ in (6.49) and (6.50), respectively, becomes singular when $R = \pm\frac{m}{\kappa}$ for real κ. Since we are only concerned about solutions for which $m \geq 0$ (those for $m \leq 0$ are found via symmetry considerations), only the positive sign is considered, or $R_0 = \frac{m}{\kappa}$. The location of the singularity is independent of Z and is hereafter termed "line singularity." The line singularity intersects any element e containing the radius R_0 (as seen in Fig. 6.3 for a homogeneous medium), or is near an element if $Min(|R_0 - R_i^e|)$ is small (not defined now) for the normalized radii of element e, R_i^e for $i \in [1,3]$. The origin of this singularity has been discussed previously in [23] for the CAP equations.

For elements containing R_0, $[a]_{ij}^e$ and $[b]_{ij}^e$ gain an additional residue contribution, automatically included by the use of the logarithm of (6.62) in the sums (6.60) and (6.61). However, for elements oriented nearly parallel to the line singularity, as in element b in Fig. 6.3, the contribution to (6.60) and (6.61), and consequently $[a]_{ij}^e$ and $[b]_{ij}^e$, become large. In the case of element a in Fig. 6.3, they become infinite. Large matrix elements are associated with the slow convergence of the conjugate gradient solver and inaccuracies in the resulting solution. Presented here is a way to avoid this problem.

To understand the nature of the problem, we recall (6.23)

$$\hat{\phi} \times \overline{h}_m(R,Z) = jf_m \left[m\hat{\phi} \times \nabla_t \psi_h + \epsilon_r R \nabla_t \psi_e \right] \tag{6.80}$$

the right hand side of which appears in (6.44) and ultimately in $[a]_{ij}^e$ and $[b]_{ij}^e$ after discretization. Since $\hat{\phi} \times \overline{h}_m$ must remain bounded everywhere in space (barring edges of perfect conductors), the right hand side of (6.80) must also. Clearly then, the bracketed terms involving ψ_e and ψ_h must combine to cancel with the singularity in $f_m = \frac{1}{(\kappa R + m)(\kappa R - m)}$. The finite element discretization, however, separates these two terms and each will individually become large when an element edge is nearly coincident with the line singularity.

To regularize $[a]_{ij}^e$ and $[b]_{ij}^e$, we first define the integral

$$I = \iint_{S^e} f_m \left(\epsilon_r R \nabla_t \psi_e^s \right) \cdot \nabla_t N_i^e dS^e + \iint_{S^e} f_m \left(m\hat{\phi} \times \nabla_t \psi_h^s \right) \cdot \nabla_t N_i^e dS^e \tag{6.81}$$

which appears in a portion of (6.44). Each of the integrals in (6.81) must be regularized, and in doing this we must subtract and add a term from each of the form

$$\frac{h(Z, R_0)}{\kappa R - m} \tag{6.82}$$

where $h(Z, R_0)$ is the factor of the integrand which is well behaved at $R = R_0$. Applying this technique to (6.81) gives

$$I = \iint_{S^e} \frac{1}{\kappa R - m} \left[\frac{\epsilon_r R \nabla_t \psi_e^s}{\kappa R + m} \cdot \nabla_t N_i^e - \frac{\epsilon_r(Z, R_0) R_0 \nabla_t \psi_e^s(Z, R_0)}{\kappa R_0 + m} \cdot \nabla_t N_i^e(Z, R_0) \right] dS^e$$

$$+ \iint_{S^e} \frac{m}{\kappa R - m} \left[\frac{\hat{\phi} \times \nabla_t \psi_h^s}{\kappa R + m} \cdot \nabla_t N_i^e - \frac{\hat{\phi} \times \nabla_t \psi_h^s(Z, R_0)}{\kappa R_0 + m} \cdot \nabla_t N_i^e(Z, R_0) \right] dS^e$$

$$+ \iint_{S^e} \frac{1}{\kappa R - m} \left[\frac{\epsilon_r(Z, R_0) R_0 \nabla_t \psi_e^s(Z, R_0) + m\hat{\phi} \times \nabla_t \psi_h^s(Z, R_0)}{\kappa R_0 + m} \right] \cdot \nabla_t N_i^e(Z, R_0) dS^e$$

$$\tag{6.83}$$

where $h(Z, R_0)$ for each integral is clear by the argument (Z, R_0). Where not explicitly shown, all functions exhibit a (Z, R) dependency.

The key to implementing this method is the elimination of the third integral in (6.83). Note that the numerator in the integral of this terms is simply the bracketed factor in (6.80) evaluated at $R = R_0$. As mentioned before, $\hat{\phi} \times \bar{h}_m(R_0, Z)$ must be finite, the bracketed term is zero at $R = R_0$. Thus,

$$m\hat{\phi} \times \nabla_t \psi_h(Z, R_0) = -\epsilon_r(Z, R_0) R_0 \nabla_t \psi_e(Z, R_0) \qquad (6.84)$$

The third integral of (6.83) vanishes when the expression is substituted into its integrand.

After following the usual discretization of the azimuthal potentials, (6.83) may be written in discrete form as

$$
\begin{aligned}
I = \sum_{j=1}^{3} \{\psi_e^s\}_j^e \iint_{S^e} \frac{1}{\kappa R - m} & \left[\frac{\epsilon_r R \nabla_t N_j^e}{\kappa R + m} \cdot \nabla_t N_i^e \right. \\
& \left. - \frac{\epsilon_r(Z, R_0) R_0 \nabla_t N_j^e(Z, R_0)}{\kappa R_0 + m} \cdot \nabla_t N_i^e(Z, R_0) \right] dS^e \\
+ \sum_{j=1}^{3} \{\psi_h^s\}_j^e \iint_{S^e} \frac{m}{\kappa R - m} & \left[\frac{\hat{\phi} \times \nabla_t N_j^e}{\kappa R + m} \cdot \nabla_t N_i^e \right. \\
& \left. - \frac{\hat{\phi} \times \nabla_t N_j^e(Z, R_0)}{\kappa R_0 + m} \cdot \nabla_t N_i^e(Z, R_0) \right] dS^e
\end{aligned}
$$

$$(6.85)$$

For linear shape functions, the gradients are constant (as well as ϵ_r) and are factored out to yield

$$
\begin{aligned}
I = \sum_{j=1}^{3} \{\psi_e^s\}_j^e \epsilon_r \iint_{S^e} \frac{1}{2\kappa(\kappa R + m)} \nabla N_j^e \cdot \nabla_t N_i^e dS^e \\
+ \sum_{j=1}^{3} \{\psi_h^s\}_j^e \iint_{S^e} \frac{m}{2m(\kappa R + m)} \hat{\phi} \times \nabla_t N_j^e \cdot \nabla_t N_i^e dS^e
\end{aligned}
$$

$$(6.86)$$

which are clearly regular when $R = \frac{m}{\kappa}$. Thus, the matrix elements in (6.49) and

(6.50), may now be written

$$[a]_{ij}^e = \iint\limits_{S^e} \left[-\frac{1}{2\kappa(\kappa R + m)} \nabla N_j^e \cdot \nabla_t N_i^e + \frac{N_i^e N_j^e}{R} \right] dS^e \qquad (6.87)$$

$$[b]_{ij}^e = \iint\limits_{S^e} \frac{1}{2(\kappa R + m)} \hat{\phi} \times \nabla_t N_j^e \cdot \nabla_t N_i^e dS^e \qquad (6.88)$$

These were implemented, but did not work very well. Note that since the potentials $\psi_e^s(Z, R_0)$ and $\psi_h^s(Z, R_0)$ were expanded in terms of linear functions, their respective gradients are are constant everywhere in the element independent of R and consequently independent of R_0. Since the derivatives $\nabla \psi_e$ and $\nabla \psi_h$ are constant over the element, this approach to regularization is of low order. To improve the accuracy, the functional dependency of this on R must be increased and for the existing discretization scheme, this may be done by refining the mesh in the vicinity of the singularity. This, however, is not a realistic option for frequency sweeps for scatterers containing lossless materials. Using higher order shape functions or employing the modal field as the working variable (i.e., $\nabla \psi_e = \nabla(Re_{m\phi}) = R\nabla e_{m\phi} + e_{m\phi}\nabla R$) would alleviate this problem. It is interesting to note that given $\psi_e = Re_{m\phi}$, a linear variation in Z of $e_{m\phi}$ corresponds to the same in ψ_e. However, a linear variation of $e_{m\phi}$ in R corresponds to a *quadratic* variation of the same in ψ_e. But since ψ_e is expressed in terms of linear shape functions here, the radial behavior is lost.

In summary, then, we have developed a method by which to alleviate the problem associated the line singularity at $R_0 = \frac{m}{\kappa}$ for real κ. This not only eliminates the need for a residue contribution to $[a]_{ij}^e$ and $[b]_{ij}^e$, but also prevents them from ever becoming infinite. In addition, a direct consequence is that these element matrices are now purely real for scatterers containing lossless materials, which is not the case for the traditional formulation presented in section 6.2.2.

6.3   Boundary Integral Formulation

In the previous section, a weak form of the wave equation was developed for scattering bodies in Ω and bounded by $\Gamma = \Gamma_a + \Gamma_c + \Gamma_z$. The boundary conditions on Γ_c and Γ_z have already been included in the system (6.76). The resulting discrete system remains incomplete, however, since the boundary conditions (which provide a relationship between the tangential $\overline{E}$ and $\overline{H}$ fields) on the exterior boundary Γ_a remain unspecified. The Stratton-Chu integral equation (S-C) provides the necessary relationship for source and integration points along Γ_a, when the integral equation is expressed in terms of fields tangent to the surface of revolution. By employing a Fourier series expansion of the S-C and thereafter discretizing it on Γ_a, the resulting system provides the needed equations for solving (6.76).

As a preliminary step , the electric and magnetic fields in the unbounded region are represented by

$$\overline{E}(\bar{r}) = \overline{E}^s(\bar{r}) + \overline{E}^i(\bar{r}) \tag{6.89}$$

$$\overline{H}(\bar{r}) = \overline{H}^s(\bar{r}) + \overline{H}^i(\bar{r}) \tag{6.90}$$

where $\overline{E}^i(\bar{r})$ and $\overline{H}^i(\bar{r})$ are the incident fields and the scattered fields are given by the Stratton-Chu equations [22]

$$\overline{E}^s(\bar{r}) = \iint\limits_{S'} \left\{ -jk_0 \left[\hat{n}' \times \eta_0 \overline{H}^s(\bar{r}') \right] g(\bar{r},\bar{r}') + \frac{1}{jk_0} \left[\hat{n}' \cdot \nabla' \times \eta_0 \overline{H}^s(\bar{r}') \right] \nabla' g(\bar{r},\bar{r}') \right.$$
$$\left. + \left[\hat{n}' \times \overline{E}^s(\bar{r}') \right] \times \nabla' g(\bar{r},\bar{r}') \right\} dS' \tag{6.91}$$

$$\eta_0 \overline{H}^s(\bar{r}) = \iint\limits_{S'} \left\{ jk_0 \left[\hat{n}' \times \overline{E}^s(\bar{r}') \right] g(\bar{r},\bar{r}') - \frac{1}{jk_0} \left[\hat{n}' \cdot \nabla \times \overline{E}^s(\bar{r}') \right] \nabla' g(\bar{r},\bar{r}') \right.$$
$$\left. + \left[\hat{n}' \times \eta_0 \overline{H}^s(\bar{r}') \right] \times \nabla' g(\bar{r},\bar{r}') \right\} dS' \tag{6.92}$$

where $\bar{r}'$ and $\bar{r}$ are the source and observation points, respectively and

$$g(\bar{r}, \bar{r}') = \frac{e^{-jk_0|\bar{r}-\bar{r}'|}}{4\pi|\bar{r}-\bar{r}'|} \tag{6.93}$$

is the free space Green's function. In this form, all field quantities are tangent to S'. Since in the development of the discrete boundary integral system the source and field points reside on the surface S', it is convenient to remove the singularity at $\bar{r} = \bar{r}'$ by expressing the integrals in (6.91) and (6.92) in terms of their respective principal values as

$$\frac{1}{2}\overline{E}^s(\bar{r}) = \oiint_{S'} \left\{ -jk_0 \left[\hat{n}' \times \eta_0 \overline{H}^s(\bar{r}')\right] g(\bar{r}, \bar{r}') + \frac{1}{jk_0} \left[\hat{n}' \cdot \nabla' \times \eta_0 \overline{H}^s(\bar{r}')\right] \nabla' g(\bar{r}, \bar{r}') \right.$$
$$\left. + \left[\hat{n}' \times \overline{E}^s(\bar{r}')\right] \times \nabla' g(\bar{r}, \bar{r}') \right\} dS' \tag{6.94}$$

$$\frac{1}{2}\eta_0 \overline{H}^s(\bar{r}) = \oiint_{S'} \left\{ jk_0 \left[\hat{n}' \times \overline{E}^s(\bar{r}')\right] g(\bar{r}, \bar{r}') - \frac{1}{jk_0} \left[\hat{n}' \cdot \nabla \times \overline{E}^s(\bar{r}')\right] \nabla' g(\bar{r}, \bar{r}') \right.$$
$$\left. + \left[\hat{n}' \times \eta_0 \overline{H}^s(\bar{r}')\right] \times \nabla' g(\bar{r}, \bar{r}') \right\} dS' \tag{6.95}$$

Looking back to (6.76), it is clear that two additional equations relating the unknown potentials ψ_e^s, ψ_h^s, ψ_{et}^s and ψ_{ht}^s are necessary to form a complete system. This may be achieved, for example, by using the $\hat{t}$ component of the modal form of (6.94) and the $\hat{\phi}$ component of the modal form of (6.95). In fact, many combinations are possible but for simplicity and symmetry, the $\hat{\phi}$ component of (6.94) and (6.95) is considered below.

6.3.1 Derivation of the Modal Boundary Integral Equation

In a fashion analogous to the finite element formulation, the development is provided explicitly for (6.94) and duality is employed to obtain the corresponding expression for (6.95). First, consider the general surface of revolution indicated in Fig. 6.1 whose tangential unit vectors are denoted by $\hat{\phi}$ and $\hat{t}$. The unit vector $\hat{t}$ subtends

an angle v with the z-axis, and $\hat{t}'$ subtends an angle v' with the z-axis. With reference to Fig. 6.1, the various unit vectors are given by

$$\hat{n} = \hat{x}\cos v\cos\phi + \hat{y}\cos v\sin\phi - \hat{z}\sin v \qquad (6.96)$$

$$\hat{\phi} = -\hat{x}\sin\phi + \hat{y}\cos\phi \qquad (6.97)$$

$$\hat{t} = \hat{x}\sin v\cos\phi + \hat{y}\sin v\sin\phi + \hat{z}\cos v \qquad (6.98)$$

$$\hat{x} = \hat{t}\sin v\cos\phi + \hat{n}\cos v\cos\phi - \hat{\phi}\sin\phi \qquad (6.99)$$

$$\hat{y} = \hat{t}\sin v\sin\phi + \hat{n}\cos v\sin\phi + \hat{\phi}\cos\phi \qquad (6.100)$$

$$\hat{z} = \hat{t}\cos v - \hat{n}\sin v \qquad (6.101)$$

Expressing the primed unit vectors in terms of the ones results in

$$\hat{t} = \hat{t}'\left[\sin v'\sin v\cos(\phi - \phi') + \cos v\cos v'\right]$$
$$+ \hat{n}'\left[\cos v'\sin v\cos(\phi - \phi') - \cos v\sin v'\right] + \hat{\phi}'\left[\sin v\sin(\phi - \phi')\right] \quad (6.102)$$

$$\hat{n} = \hat{t}'\left[\sin v'\cos v\cos(\phi - \phi') - \sin v\cos v'\right]$$
$$+ \hat{n}'\left[\cos v'\cos v\cos(\phi - \phi') + \sin v\sin v'\right] + \hat{\phi}'\left[\cos v\sin(\phi - \phi')\right] \quad (6.103)$$

$$\hat{\phi} = -\hat{\rho}'\sin(\phi - \phi') + \hat{\phi}'\cos(\phi - \phi') \qquad (6.104)$$

which clearly reveal the dependency of the unit vectors on the azimuthal variation $\phi - \phi'$. Further, the following identities can be shown to hold:

$$\hat{\phi} \cdot \nabla'g = -\hat{\phi} \cdot \nabla g \qquad (6.105)$$

$$\hat{\phi} \cdot (\hat{n}' \times \eta_0\overline{H}^s) = -\eta_0 H_\phi^s \sin v'\sin(\phi - \phi') - \eta_0 H_t^s \cos(\phi - \phi') \quad (6.106)$$

$$\hat{n}' \cdot (\nabla' \times \eta_0\overline{H}^s) = \frac{1}{\rho'}\left[-\frac{\partial}{\partial t'}(\rho'\eta_0 H_\phi^s) + \frac{\partial}{\partial\phi'}(\eta_0 H_t^s)\right] \qquad (6.107)$$

$$\hat{\phi} \cdot \left[(\hat{n}' \times \overline{E}^s) \times \nabla'g\right] = \left[\hat{z}'E_t^s\sin(\phi - \phi') + \hat{n}'E_\phi^s\cos(\phi - \phi')\right.$$
$$\left. + \hat{\phi}'E_\phi^s\cos v'\sin(\phi - \phi')\right] \cdot \nabla'g \qquad (6.108)$$

Using these in (6.94) gives

$$\tfrac{1}{2}E_\phi^s(\bar{r}) = \oint_{\Gamma_a} \int_0^{2\pi} \left\{ jk_0\left[\eta_0 H_\phi^s \sin v' \sin(\phi - \phi') + \eta_0 H_t^s \cos(\phi - \phi')\right] g(\bar{r},\bar{r}') \right.$$

$$- \frac{1}{jk_0\rho'}\left[-\tfrac{\partial}{\partial t'}(\rho'\eta_0 H_\phi^s) + \tfrac{\partial}{\partial \phi'}(\eta_0 H_t^s)\right]\hat{\phi}\cdot\nabla g(\bar{r},\bar{r}') + \left[\hat{z}'E_t^s \sin(\phi - \phi')\right.$$

$$\left.\left. + \hat{n}'E_\phi^s \cos(\phi - \phi') + \hat{\phi}'E_\phi^s \cos v' \sin(\phi - \phi')\right]\cdot\nabla'g\right\}\rho'd\phi'dt'$$

$$(6.109)$$

and by carrying out the derivatives of the Green's functions, we find

$$\tfrac{1}{2}E_\phi^s(\bar{r}) = \oint_{\Gamma_a} \int_0^{2\pi} \left\{ jk_0\left[\eta_0 H_\phi^s \sin v' \sin(\phi - \phi') + \eta_0 H_t^s \cos(\phi - \phi')\right] g(\bar{r},\bar{r}') \right.$$

$$- \frac{1}{jk_0}\left[-\tfrac{\partial}{\partial t'}(\rho'\eta_0 H_\phi^s) + \tfrac{\partial}{\partial \phi'}(\eta_0 H_t^s)\right]\sin(\phi - \phi')\frac{1}{R_0}\frac{dg}{dR_0}$$

$$+ \left(-E_t^s(z - z')\sin(\phi - \phi') + E_\phi^s\left\{\cos(\phi - \phi')[(z - z')\sin v' - (\rho - \rho')\cos v']\right.\right.$$

$$\left.\left.\left. - 2\rho\cos v' \sin^2(\tfrac{\phi - \phi'}{2})\right\}\right)\frac{1}{R_0}\frac{dg}{dR_0}\right\}\rho'd\phi'dt' \qquad (6.110)$$

in which

$$R_0 = \sqrt{\rho^2 + \rho'^2 - 2\rho\rho'\cos(\phi - \phi') + (z - z')^2} \qquad (6.111)$$

The integrand of (6.110) is expressed explicitly in terms of ϕ and ϕ' and is now suitable for harmonic decomposition.

To generate the corresponding modal integral equations in terms of the Fourier coefficients, the fields and Green's function may be expanded as

$$\bar{E}^s(\bar{r}) = \sum_{m=-\infty}^{\infty} \bar{e}_m^s(\rho, z)e^{jm\phi} \qquad (6.112)$$

$$\eta_0\bar{H}^s(\bar{r}) = \sum_{m=-\infty}^{\infty} \bar{h}_m^s(\rho, z)e^{jm\phi} \qquad (6.113)$$

$$g^{(k)}(\bar{r},\bar{r}') = \sum_{n=-\infty}^{\infty} g_n^{(k)}(\rho, \rho', z, z')e^{jn(\phi - \phi')} \qquad (6.114)$$

where

$$\bar{e}_m^s(\rho, z) = \frac{1}{2\pi}\int_{-\pi}^{\pi} \bar{E}^s(\rho, u, z)e^{-jmu}du \qquad (6.115)$$

$$\bar{h}^s_m(\rho, z) = \frac{\eta_0}{2\pi} \int_{-\pi}^{\pi} \bar{H}^s(\rho, u, z) e^{-jmu} du \qquad (6.116)$$

$$g_n^{(0)}(\rho, \rho', z, z') = \frac{1}{\pi} \int_0^{\pi} \frac{e^{-jk_0 \tilde{R}}}{4\pi \tilde{R}} \cos(nu) du \qquad (6.117)$$

$$g_n^{(1)}(\rho, \rho', z, z') = \frac{1}{\pi} \int_0^{\pi} \cos u \frac{e^{-jk_0 \tilde{R}}}{4\pi \tilde{R}} \cos(nu) du \qquad (6.118)$$

$$g_n^{(2)}(\rho, \rho', z, z') = -\frac{j}{\pi} \int_0^{\pi} \sin u \frac{e^{-jk_0 \tilde{R}}}{4\pi \tilde{R}} \sin(nu) du \qquad (6.119)$$

$$g_n^{(0)'}(\rho, \rho', z, z') = \frac{1}{\pi k_0^2} \int_0^{\pi} \frac{1}{\tilde{R}} \frac{dg}{d\tilde{R}} \cos(nu) du \qquad (6.120)$$

$$g_n^{(1)'}(\rho, \rho', z, z') = \frac{1}{\pi k_0^2} \int_0^{\pi} \cos u \frac{1}{\tilde{R}} \frac{dg}{d\tilde{R}} \cos(nu) du \qquad (6.121)$$

$$g_n^{(2)'}(\rho, \rho', z, z') = -\frac{j}{\pi k_0^2} \int_0^{\pi} \sin u \frac{1}{\tilde{R}} \frac{dg}{d\tilde{R}} \sin(nu) du \qquad (6.122)$$

in which

$$\tilde{R} = \sqrt{\rho^2 + \rho'^2 - 2\rho\rho' \cos u + (z - z')^2} \qquad (6.123)$$

Substituting these into (6.110) yields

$$\frac{1}{2} \sum_{n=-\infty}^{\infty} e^s_{n\phi}(\rho, z) e^{jn\phi} = \sum_{n=-\infty}^{\infty} \sum_{m=-\infty}^{\infty} e^{jn\phi} \oint_{\Gamma_a} \int_0^{2\pi} \left\{ jk_0 \left[h^s_{m\phi} \sin v' g_n^{(2)} + h^s_{mt} g_n^{(1)} \right] \right.$$
$$- \frac{1}{jk_0} \left[-\frac{\partial}{\partial t'}(\rho' h^s_{m\phi}) + jm h^s_{mt} \right] k_0^2 g_n^{(2)'}$$
$$- e^s_{mt}(z - z') k_0^2 g_n^{(2)'} + e^s_{m\phi} k_0^2 (\rho' \cos v' g_n^{(1)'}$$
$$\left. - \rho \cos v' g_n' + (z - z') \sin v' g_n^{(1)'}) \right\} e^{j(m-n)\phi'} \rho' d\phi' dt' \qquad (6.124)$$

where t' is the parameter along the contour Γ_a and increases in the clockwise direction as shown in Fig. 6.2. Further, upon multiplying each side by $e^{-jp\phi}$ and integrating over $(0, 2\pi)$ to extract the mth harmonic equation gives

$$\frac{1}{2} e^s_{m\phi}(\rho, z) = 2\pi \oint_{\Gamma_a} \left\{ j h^s_{m\phi} \sin v' g_m^{(2)} - j \frac{\partial}{\partial t'}(\rho' h^s_{m\phi}) g_m^{(2)'} + (j h^s_{mt}) \left[g_m^{(1)} + jm g_m^{(2)'} \right] \right.$$
$$+ e^s_{m\phi} k_0 (\rho' \cos v' g_m^{(1)'} - \rho \cos v' g_m' + (z - z') \sin v' g_m^{(1)'})$$
$$\left. - e^s_{mt}(z - z') k_0 g_m^{(2)'} \right\} k_0 \rho' dt' \qquad (6.125)$$

after also combining similar terms and where we have used the identity

$$\int_0^{2\pi} e^{j(m-n)\phi'} d\phi' = \begin{cases} 2\pi & m = n \\ 0 & \text{otherwise} \end{cases} \tag{6.126}$$

Introducing the normalized coordinates

$$R = k_0 \rho \quad R' = k_0 \rho'$$

$$Z = k_0 z \quad Z' = k_0 z'$$

$$\frac{\partial}{\partial t'} = k_0 \frac{\partial}{\partial \tau'} \tag{6.127}$$

in (6.125) and replacing the field quantities with the azimuthal potentials yields

$$\frac{1}{2R}\psi_e^s = \frac{2\pi}{k_0} \oint_{\Gamma_a} \left\{ \psi_h^s \left[j \sin v' g_m^{(2)} \right] - \left(\frac{\partial}{\partial \tau'}\psi_h^s \right) \left[j R' g_m^{(2)'} \right] + \psi_{ht}^s \left[g_m^{(1)} + jm g_m^{(2)'} \right] \right.$$

$$+ \psi_e^s \left[R' \cos v' g_m^{(1)'} - R \cos v' g_m' + (Z - Z') \sin v' g_m^{(1)'} \right]$$

$$\left. + \psi_{et}^s \left[j(Z - Z') g_m^{(2)'} \right] \right\} d\tau' \tag{6.128}$$

This equation and its dual form a pair of integral equations to be imposed at the mesh termination boundary. Their discretization is considered next.

6.3.2 Discretization of the Modal Boundary Integral Equation

In discretizing the modal boundary integral in (6.128), the contour Γ_a is first divided into N_a elements each of length Δ^e. Within the eth observation element, the parametric representation

$$R = R_1^e + \tau \sin v^e \tag{6.129}$$

$$Z = Z_1^e + \tau \cos v^e \tag{6.130}$$

is adopted as shown in Fig. 6.4 and is consistent with the required counterclockwise path traversal of Γ_a. Likewise, within the source element e', the parametric
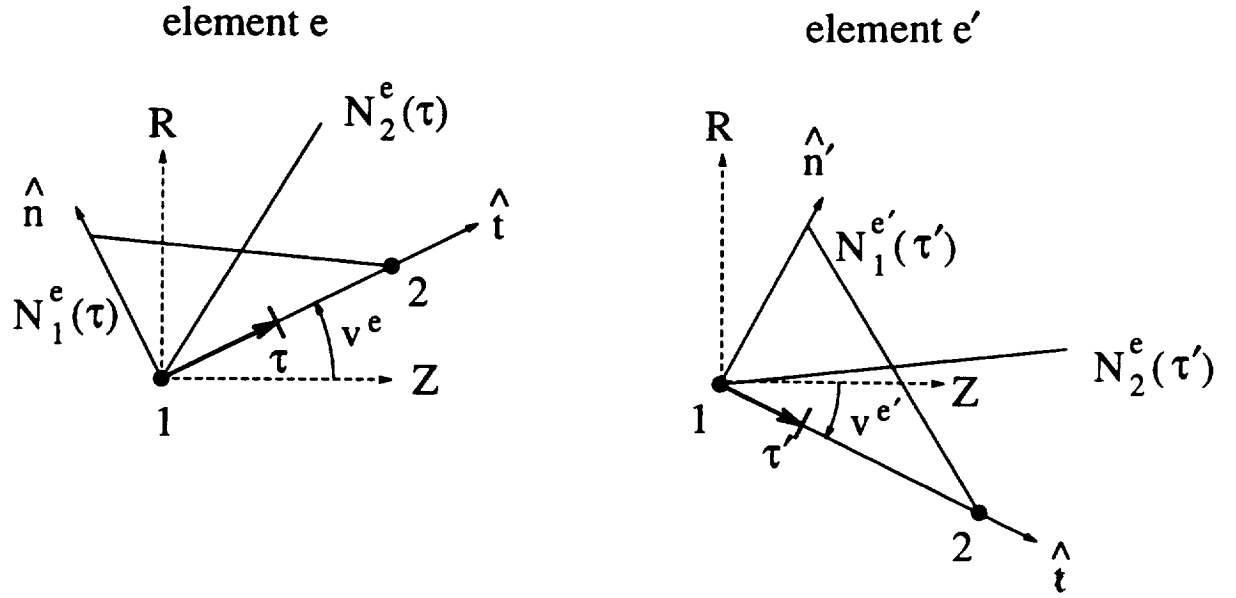
element e

element e′

Figure 6.4: A typical pair of source (e′) and observation (e) elements associated with the discretization of the boundary integral equation

representation

$$R' = R_1^{e'} + \tau' \sin v^{e'} \tag{6.131}$$

$$Z' = Z_1^{e'} + \tau' \cos v^{e'} \tag{6.132}$$

is employed. In terms of the parameter τ', potentials within each boundary element are represented as

$$u(\tau') = \sum_{e'=1}^{N_a} \sum_{j=1}^{2} N_j^{e'}(\tau') \, \{u\}_j^{e'} \tag{6.133}$$

where u represents any one of ψ_e^s, ψ_h^s, ψ_{et}^s or ψ_{ht}^s and

$$N_1^{e'}(\tau') = \frac{1 - \tau'}{\Delta^{e'}} \tag{6.134}$$

$$N_2^{e'}(\tau') = \frac{\tau'}{\Delta^{e'}} \tag{6.135}$$

are linear parameterized functions of τ'. (Note that the linear basis functions are employed in the finite element discretization.) Employing the method of weighted

residuals over the eth observation element and Galerkin's technique to (6.128) gives

$$-\frac{1}{2}\sum_{e'=1}^{N_a}\sum_{j=1}^{2}\{\psi_e^s\}_j^{e'}\int_0^{\Delta^e}\frac{N_i^e N_j^e}{R}d\tau + \frac{2\pi}{k_0}\sum_{e'=1}^{N_a}\sum_{j=1}^{2}\int_0^{\Delta^e}\!\!\int_0^{\Delta^{e'}}\left\{\{\psi_h^s\}_j^{e'}\ N_i^e N_j^{e'}\left[j\sin v' g_m^{(2)}\right]\right.$$

$$-\{\psi_h^s\}_j^{e'}N_i^e(\tfrac{\partial}{\partial\tau'}N_j^{e'})\left[jR'g_m^{(2)'}\right] + \{\psi_{ht}^s\}_j^{e'}\ N_i^e N_j^{e'}\left[g_m^{(1)} + jm g_m^{(2)'}\right]$$

$$+ \{\psi_e^s\}_j^{e'}\ N_i^e N_j^{e'}\left[R'\cos v' g_m^{(1)'} - R\cos v' g_m' + (Z-Z')\sin v' g_m^{(1)'}\right]$$

$$+ \{\psi_{et}^s\}_j^{e'}\ N_i^e N_j^{e'}\left[j(Z-Z')g_m^{(2)'}\right]\right\}d\tau'd\tau = 0 \qquad (6.136)$$

In deriving the first term in equation (6.136), it is useful to note that $\psi_e^s(\tau)$ may be written

$$\psi_e^s(\tau) = \int_{\Gamma_a}\psi_e^s(\tau')\delta(\tau - \tau')d\tau' \qquad (6.137)$$

where δ is the Dirac delta function. Substituting (6.133) into (6.137) yields

$$\psi_e^s(\tau) = \sum_{e'=1}^{N_a}\sum_{j=1}^{2}\{\psi_e^s\}_j^{e'}\int_{\Gamma_a} N_j^{e'}(\tau')\delta(\tau - \tau')d\tau'$$

$$= \sum_{e'=1}^{N_a}\sum_{j=1}^{2}\{\psi_e^s\}_j^{e'}N_j^{e'}(\tau) \qquad (6.138)$$

Taking the inner product of (6.138) with $\frac{N_i^e(\tau)}{R}$ yields

$$\int_{\Gamma_a}\frac{N_i^e(\tau)}{R}\psi_e^s(\tau)d\tau = \sum_{e'=1}^{N_a}\sum_{j=1}^{2}\{\psi_e^s\}_j^{e'}\int_{\Gamma_a}\frac{N_i^e(\tau)N_j^{e'}(\tau)}{R}d\tau \qquad (6.139)$$

as expected.

The system (6.136) may be written in compact matrix notation

$$\sum_{e'=1}^{N_a}\sum_{j=1}^{2}\left[\ [L_\phi]_{ij}^{ee'}\{\psi_e^s\}_j^{e'} + [M_\phi]_{ij}^{ee'}\{\psi_h^s\}_j^{e'} + [L_t]_{ij}^{ee'}\{\psi_{et}^s\}_j^{e'} + [M_t]_{ij}^{ee'}\{\psi_{ht}^s\}_j^{e'}\ \right] = 0 \qquad (6.140)$$

where we easily see that

$$[L_\phi]_{ij}^{ee'} = -\frac{1}{2}\int_0^{\Delta^e}\frac{N_i^e N_j^{e'}}{R}d\tau + \frac{2\pi}{k_0}\int_0^{\Delta^e}\!\!\int_0^{\Delta^{e'}} N_i^e N_j^{e'}\left[R'\cos v' g_m^{(1)'} - R\cos v' g_m'\right.$$

$$\left. +(Z-Z')\sin v' g_m^{(1)'}\right]d\tau'd\tau \qquad (6.141)$$

$$[M_\phi]_{ij}^{ee'} = \frac{2\pi}{k_0} \int_0^{\Delta^e} \int_0^{\Delta^{e'}} \left\{ N_i^e N_j^{e'} \left[j \sin v' g_m^{(2)} \right] - N_i^e \left(\tfrac{\partial}{\partial \tau'} N_j^{e'} \right) \left[j R' g_m^{(2)'} \right] \right\} d\tau' d\tau \quad (6.142)$$

$$[L_t]_{ij}^{ee'} = \frac{2\pi}{k_0} \int_0^{\Delta^e} \int_0^{\Delta^{e'}} N_i^e N_j^{e'} \left[j(Z - Z') g_m^{(2)'} \right] d\tau' d\tau \quad (6.143)$$

$$[M_t]_{ij}^{ee'} = \frac{2\pi}{k_0} \int_0^{\Delta^e} \int_0^{\Delta^{e'}} N_i^e N_j^{e'} \left[g_m^{(1)} + j m g_m^{(2)'} \right] d\tau' d\tau \quad (6.144)$$

Each matrix of the form $[A_\phi]_{ij}^{ee'}$ can be termed "element interaction matrix" (after the finite element term "element matrix" for the case $e = e'$), since it represents the interaction between the source element e' and the observation element e for $i, j \in 1, 2$ of the local weighting and expansion functions, respectively. The numerical evaluation of the integrals in (6.141) – (6.144) is performed by breaking the integral into two integrals with continuous integrands and performing midpoint integration for each of them. This applies to the integration in τ' as well as for τ. When the source and observation points coincide, an average value is computed by moving the observation point $\frac{\Delta^e}{4}$ away from the sub-cell center. This has been shown to work well in [25], and avoids the need for elaborate self-cell evaluation techniques. In all cases, Gaussian quadrature is employed for the ϕ' integration in (6.117) – (6.122).

The local "interaction element matrices' may be assembled to form a global boundary integral system in a fashion analogous to the finite element method by first summing (6.140) over all observation elements e as

$$\sum_{e=1}^{N_a} \sum_{e'=1}^{N_a} \sum_{j=1}^{2} \left[[L_\phi]_{kl}^{ee'} \{\psi_e^s\}_l^{e'} + [M_\phi]_{kl}^{ee'} \{\psi_h^s\}_l^{e'} + [L_t]_{kl}^{ee'} \{\psi_{et}^s\}_l^{e'} + [M_t]_{kl}^{ee'} \{\psi_{ht}^s\}_l^{e'} \right] = 0$$

$$(6.145)$$

where the local element subscripts i, j have been replaced by their global counterparts k, l and are related by the node–element connectivity transformation function q as

$$k = q(e, i) \quad (6.146)$$

$$l = q(e', j) \quad (6.147)$$

$$A(k,l) = 0 \quad k,l \in \{1, N_a\}$$

$$\text{Do } e = 1 \text{ to } N_a$$

$$\text{Do } e' = 1 \text{ to } N_a$$

$$\text{Do } i=1 \text{ to } 2$$

$$\text{Do } j=1 \text{ to } 2$$

$$k = q(e,i)$$

$$l = q(e',j)$$

$$\text{Form } [A]_{ij}^{e'}$$

$$A(k,l) = A(k,l) + [A]_{ij}^{ee'}$$

$$\text{End Do}$$

$$\text{End Do}$$

$$\text{End Do}$$

$$\text{End Do}$$

Table 6.1: An algorithm for the boundary integral system assembly for a generic element interaction matrix $[A]_{ij}^{ee'}$

In Table 6.1 is illustrated an algorithm where a generic matrix $[A_\phi]_{ij}^{ee'}$ (where A represents any of L_ϕ, M_ϕ, L_t or M_t) is assembled to form a global system. This algorithm differs from that of the finite element method, in that the loop in e' is eliminated.

The final FE–BI system is formed by augmenting finite element system with

(6.145) and its dual giving

$$
\begin{bmatrix}
A_{aa}^{\epsilon} & 0 & A_{aI}^{\epsilon} & -B_{aa} & 0 & -B_{aI} & 0 & -C_{aa} \\
0 & I & 0 & 0 & 0 & 0 & C_{aa} & 0 \\
A_{Ia}^{\epsilon} & A_{Ic}^{\epsilon} & A_{II}^{\epsilon} & -B_{Ia} & -B_{Ic} & -B_{II} & 0 & 0 \\
B_{aa} & 0 & B_{aI} & A_{aa}^{\mu} & 0 & A_{aI}^{\mu} & 0 & 0 \\
0 & B_{cc} & B_{cI} & 0 & A_{cc}^{\mu} & A_{cI}^{\mu} & 0 & 0 \\
B_{Ia} & B_{Ic} & B_{II} & A_{Ia}^{\mu} & A_{Ic}^{\mu} & A_{II}^{\mu} & 0 & 0 \\
L_{\phi} & M_{\phi} & 0 & 0 & 0 & 0 & L_t & M_t \\
-M_{\phi} & L_{\phi} & 0 & 0 & 0 & 0 & -M_t & L_t
\end{bmatrix}
\begin{bmatrix}
\{\psi_e^s\}_a \\
\{\psi_e^s\}_c \\
\{\psi_e^s\}_I \\
\{\psi_h^s\}_a \\
\{\psi_h^s\}_c \\
\{\psi_h^s\}_I \\
\{\psi_{et}^s\}_a \\
\{\psi_{ht}^s\}_c
\end{bmatrix}
=
\begin{bmatrix}
\{U\}_a \\
-\{\psi_e^i\}_c \\
\{U\}_I \\
\{V\}_a \\
\{V\}_c \\
\{V\}_I \\
0 \\
0
\end{bmatrix}
$$

$$
+ \left[\; \sum_{e=1}^{N_e} \int_{\Gamma_a} N_i^e (j h_{mt}^i) dl \quad 0 \quad 0 \quad -\sum_{e=1}^{N_e} \int_{\Gamma_a} N_i^e (j e_{mt}^i) dl \quad 0 \quad 0 \; \right]^T
$$

(6.148)

which can be solved by the conjugate gradient method. Before considering different solutions of this system, we must develop the harmonic coefficients of various sources of excitation. This is considered next.

6.4 Sources of Electromagnetic Radiation

The modal forms for a plane wave excitation and an electric dipole source are developed in this section. The former is employed for scattering problems while the latter may be used for both scattering and radiation. For both cases being considered, the resulting expressions for the azimuthal potentials are used in the expressions developed in section 6.2.

6.4.1   A Plane Wave Excitation

A plane wave incident at angles (θ^i, ϕ^i) and observed at $\bar{r} = (r, \phi, z)$ (see Fig. 6.1) has the form

$$\bar{u}_\phi(\theta^i, \phi^i; \rho, \phi, z) = \hat{\phi}^i e^{-j\bar{k}_0 \cdot \bar{r}} \tag{6.149}$$

$$\bar{u}_\theta(\theta^i, \phi^i; \rho, \phi, z) = \hat{\theta}^i e^{-j\bar{k}_0 \cdot \bar{r}} \tag{6.150}$$

where $\hat{\phi}^i$ is perpendicular to the plane of incidence and $\hat{\theta}^i$ is in the plane of incidence. Expressions (6.149) and (6.150) may be written as explicit functions of ϕ by first writing the argument of the exponential function as

$$\bar{k}_0 \cdot \bar{r} = k_0 r(-\hat{z}' \cdot \hat{r})$$

$$= -k_0 \left[\rho \sin \theta^i \cos(\phi - \phi^i) + z \cos \theta^i \right] \tag{6.151}$$

since

$$\hat{r} = \hat{x} \sin \theta \cos \phi + \hat{y} \sin \theta \sin \phi + \hat{z} \cos \theta \tag{6.152}$$

$$\hat{z}' = \hat{x} \sin \theta^i \cos \phi^i + \hat{y} \sin \theta^i \sin \phi^i + \hat{z} \cos \theta^i \tag{6.153}$$

Also, making use of the unit vector transformations

$$\hat{\phi}^i = -\hat{x} \sin \theta^i + \hat{y} \cos \theta^i \tag{6.154}$$

$$\hat{\theta}^i = \hat{x} \cos \theta^i \cos \phi^i + \hat{y} \cos \theta^i \sin \phi^i - \hat{z} \sin \theta^i \tag{6.155}$$

$$\hat{x} = \hat{\rho} \cos \phi - \hat{\phi} \sin \phi \tag{6.156}$$

$$\hat{y} = \hat{\rho} \sin \phi + \hat{\phi} \cos \phi \tag{6.157}$$

$$\hat{z} = \hat{z} \tag{6.158}$$

(6.149) and (6.150) can be rewritten as

$$\bar{u}_\phi(\theta^i; \rho, \phi - \phi^i, z) = \left[\hat{\rho} \sin(\phi - \phi^i) + \hat{\phi} \cos(\phi - \phi^i) \right] e^{jk_0 [\rho \sin \theta^i \cos(\phi - \phi^i) + z \cos \theta^i]}$$

$$(6.159)$$

$$\overline{u}_\theta(\theta^i; \rho, \phi - \phi^i, z) = \left[\hat{\rho} \cos \theta^i \cos(\phi - \phi^i) - \hat{\phi} \cos \theta^i \sin(\phi - \phi^i) - \hat{z} \sin \theta^i \right]$$

$$e^{jk_0 [\rho \sin \theta^i \cos(\phi - \phi^i) + z \cos \theta^i]} \qquad (6.160)$$

These may be expanded into a Fourier series in the parameter $(\phi - \phi^i)$ by first writing (6.149) and (6.150) as

$$\overline{u}_\phi(\theta^i; \rho, \phi - \phi^i, z) = \sum_{m=-\infty}^{\infty} \overline{u}_{m\phi}(\theta^i; \rho, z) e^{jm(\phi - \phi^i)} \qquad (6.161)$$

$$\overline{u}_\theta(\theta^i; \rho, \phi - \phi^i, z) = \sum_{m=-\infty}^{\infty} \overline{u}_{m\theta}(\theta^i; \rho, z) e^{jm(\phi - \phi^i)} \qquad (6.162)$$

Each component of (6.159) and (6.160) may be expressed in terms of one of the functions

$$f(\theta^i; \rho, \phi - \phi^i) = e^{jk_0 \rho \sin \theta^i \cos(\phi - \phi^i)} \qquad (6.163)$$

$$f_c(\theta^i; \rho, \phi - \phi^i) = \cos(\phi - \phi^i) f(\theta^i; \rho, \phi - \phi^i) \qquad (6.164)$$

$$f_s(\theta^i; \rho, \phi - \phi^i) = \sin(\phi - \phi^i) f(\theta^i; \rho, \phi - \phi^i) \qquad (6.165)$$

Expanding each of these into a Fourier series in $(\phi - \phi^i)$ and using the even/odd properties

$$\begin{aligned} s(\phi) = s(-\phi) &\Longleftrightarrow s_m(u) = s_{-m}(u) \quad \text{for } f, f_c \\ s(\phi) = -s(-\phi) &\Longleftrightarrow s_m(u) = -s_{-m}(u) \quad \text{for } f_s \end{aligned} \qquad (6.166)$$

of the functions f in (6.163) – (6.165) may be expanded as

$$f(\theta^i; \rho, \phi - \phi^i) = f_0(\theta^i, \rho) + 2 \sum_{m=1}^{\infty} f_m(\theta^i, \rho) \cos[m(\phi - \phi^i)] \qquad (6.167)$$

$$f_c(\theta^i; \rho, \phi - \phi^i) = f_{c0}(\theta^i, \rho) + 2 \sum_{m=1}^{\infty} f_{cm}(\theta^i, \rho) \cos[m(\phi - \phi^i)] \qquad (6.168)$$

$$f_s(\theta^i; \rho, \phi - \phi^i) = 2j \sum_{m=1}^{\infty} f_{sm}(\theta^i, \rho) \sin[m(\phi - \phi^i)] \qquad (6.169)$$

with the corresponding Fourier coefficients

$$f_m(\theta^i, \rho) = \frac{1}{\pi} \int_0^\pi e^{jk_0\rho \sin \theta^i \cos u} \cos(mu) du \tag{6.170}$$

$$f_{cm}(\theta^i, \rho) = \frac{1}{\pi} \int_0^\pi \cos u e^{jk_0\rho \sin \theta^i \cos u} \cos(mu) du \tag{6.171}$$

$$f_{sm}(\theta^i, \rho) = -\frac{j}{\pi} \int_0^\pi \sin u e^{jk_0\rho \sin \theta^i \cos u} \sin(mu) du \tag{6.172}$$

Comparing these to the Bessel function identities

$$j^m J_m(\beta) = \frac{1}{\pi} \int_0^\pi e^{j\beta \cos x} \cos(mx) dx \tag{6.173}$$

$$j^{m-1} J_m'(\beta) = \frac{1}{\pi} \int_0^\pi \cos x e^{j\beta \cos x} \cos(mx) dx \tag{6.174}$$

$$-\frac{m}{\beta} j^m J_m(\beta) = -\frac{j}{\pi} \int_0^\pi \sin x e^{j\beta \cos x} \sin(mx) dx \tag{6.175}$$

where the last two are derived from the first by differentiation with respect to β and integration by parts respectively, we conclude that

$$f_m(\theta^i, \rho) = j^m J_m(k_0\rho \sin \theta^i) \tag{6.176}$$

$$f_{cm}(\theta^i, \rho) = j^{m-1} J_m'(k_0\rho \sin \theta^i) \tag{6.177}$$

$$f_{sm}(\theta^i, \rho) = -\frac{m}{k_0\rho \sin \theta^i} f_m(\theta^i, \rho) \tag{6.178}$$

Using these, along with (6.163) – (6.165) in (6.159) and (6.160), the Fourier coefficients of (6.161) and (6.162) are found to be

$$\overline{u}_{m\phi}(\theta^i; \rho, z) = e^{jk_0 z \cos \theta^i} \left[\hat{\rho} f_{sm}(\theta^i, \rho) + \hat{\phi} f_{cm}(\theta^i, \rho) \right] \tag{6.179}$$

$$\overline{u}_{m\theta}(\theta^i; \rho, z) = e^{jk_0 z \cos \theta^i} \left[\hat{\rho} f_{cm}(\theta^i, \rho) \cos \theta^i - \hat{\phi} f_{sm}(\theta^i, \rho) \cos \theta^i - \hat{z} f_m(\theta^i, \rho) \sin \theta^i \right] \tag{6.180}$$

or, using (6.166),

$$\overline{u}_\phi(\theta^i; \rho, \phi - \phi^i, z) = e^{jk_0 z \cos \theta^i} \left[\hat{\rho} 2j \sum_{m=1}^\infty f_{sm}(\theta^i, \rho) \sin[m(\phi - \phi^i)] \right.$$

$$+ \hat{\phi} f_{c0}(\theta^i, \rho) + \hat{\phi} 2 \sum_{m=1}^{\infty} f_{cm}(\theta^i, \rho) \cos[m(\phi - \phi^i)] \Big] \qquad (6.181)$$

$$\overline{u}_\theta(\theta^i; \rho, \phi - \phi^i, z) = e^{jk_0 z \cos \theta^i}$$

$$\Big\{ \hat{\rho} \cos \theta^i \Big[f_{c0}(\theta^i, \rho) + 2 \sum_{m=1}^{\infty} f_{cm}(\theta^i, \rho) \cos[m(\phi - \phi^i)] \Big]$$

$$- \hat{\phi} \cos \theta^i \Big[2j \sum_{m=1}^{\infty} f_{sm}(\theta^i, \rho) \sin[m(\phi - \phi^i)] \Big] \qquad (6.182)$$

$$- \hat{z} \sin \theta^i \Big[f_0(\theta^i, \rho) + 2 \sum_{m=1}^{\infty} f_m(\theta^i, \rho) \cos[m(\phi - \phi^i)] \Big] \Big\}$$

The modal coefficients $\overline{u}_{m\theta}$ and $\overline{u}_{m\phi}$ can now be used for determining the harmonic coefficients of the incident and magnetic fields. For TE_z incidence, we have

$$\overline{e}_m^i = \overline{u}_{m\phi} \qquad (6.183)$$

$$\overline{h}_m^i = \overline{u}_{m\theta} \qquad (6.184)$$

and for TM_z incidence

$$\overline{e}_m^i = -\overline{u}_{m\theta} \qquad (6.185)$$

$$\overline{h}_m^i = \overline{u}_{m\phi} \qquad (6.186)$$

More explicitly and in component form

$$e_{m\phi}^i = f_{cm}(\theta^i, \rho)\, e^{jk_0 z \cos \theta^i} \qquad (6.187)$$

$$h_{m\phi}^i = f_{sm}(\theta^i, \rho) \cos \theta^i\, e^{jk_0 z \cos \theta^i} \qquad (6.188)$$

$$e_{mt}^i = f_{sm}(\theta^i, \rho) \sin v\, e^{jk_0 z \cos \theta^i} \qquad (6.189)$$

$$h_{mt}^i = \Big[f_m(\theta^i, \rho) \sin \theta^i \cos v - f_{cm}(\theta^i, \rho) \cos \theta^i \sin v \Big] e^{jk_0 z \cos \theta^i} \qquad (6.190)$$

for TE_z polarization and

$$e_{m\phi}^i = -f_{sm}(\theta^i, \rho) \cos \theta^i\, e^{jk_0 z \cos \theta^i} \qquad (6.191)$$

$$h_{m\phi}^i = f_{cm}(\theta^i, \rho)\, e^{jk_0 z \cos \theta^i} \qquad (6.192)$$

$$e^i_{mt} = \left[f_{cm}(\theta^i, \rho) \cos \theta^i \sin v - f_m(\theta^i, \rho) \sin \theta^i \cos v \right] e^{jk_0 z \cos \theta^i} \qquad (6.193)$$

$$h^i_{mt} = f_{sm}(\theta^i, \rho) \sin v \; e^{jk_0 z \cos \theta^i} \qquad (6.194)$$

for TM_z polarization, where v is the angle between the z-axis and the vector $\hat{t}$ in the $\rho - z$ plane. The corresponding potential forms are obtained by multiplying the previous expressions by $R = k_0 \rho$.

6.4.2 An Electric Dipole Source

An $\hat{x}$-directed electric dipole of moment $\hat{x} 4\pi\epsilon/k^3$ located at a point z_0 on the z-axis is given by [26]

$$E_r = \frac{e^{-jR_0}}{R_0} \left[\frac{kr(kr - kz_0 \cos\theta)}{R_0^2} \left(\frac{3}{R_0^2} + \frac{3j}{R_0} - 1 \right) - \frac{j}{R_0} - \frac{1}{R_0^2} + 1 \right] \sin\theta \cos\phi \quad (6.195)$$

$$E_\theta = \frac{e^{-jR_0}}{R_0} \left[\frac{krkz_0 \sin^2\theta}{R_0^2} \left(\frac{3}{R_0^2} + \frac{3j}{R_0} - 1 \right) - \left(\frac{j}{R_0} + \frac{1}{R_0^2} - 1 \right) \cos\theta \right] \cos\phi \qquad (6.196)$$

$$E_\phi = \frac{e^{-jR_0}}{R_0} \left[\frac{j}{R_0} + \frac{1}{R_0^2} - 1 \right] \sin\phi \qquad (6.197)$$

$$\eta H_r = j\frac{e^{-jR_0}}{R_0} \left[\frac{j}{R_0} + \frac{1}{R_0^2} \right] kz_0 \sin\theta \sin\phi \qquad (6.198)$$

$$\eta H_\theta = j\frac{e^{-jR_0}}{R_0} \left[\frac{j}{R_0} + \frac{1}{R_0^2} \right] (kr - kz_0 \cos\theta) \sin\phi \qquad (6.199)$$

$$\eta H_\phi = j\frac{e^{-jR_0}}{R_0} \left[\frac{j}{R_0} + \frac{1}{R_0^2} \right] (kr \cos\theta - kz_0) \cos\phi \qquad (6.200)$$

where

$$R_0 = k\sqrt{r^2 \sin^2\theta + (r\cos\theta - z_0)^2} \qquad (6.201)$$

When using this source in connection with the current implementation, the harmonic coefficients of the fields must first be determined. This may be done rather trivially by noting the identities

$$\sin\phi = \frac{e^{j\phi} - e^{-j\phi}}{2j} \qquad (6.202)$$

$$\cos\phi = \frac{e^{j\phi} + e^{-j\phi}}{2} \qquad (6.203)$$

Introducing these into (6.195) - (6.200) and comparing with (6.161) and (6.162) we find (on setting $\phi^i = 0$) that

$$e_{mr} = \frac{e^{-jR_0}}{2R_0}\left[\frac{kr(kr - kz_0\cos\theta)}{R_0^2}\left(\frac{3}{R_0^2} + \frac{3j}{R_0} - 1\right) - \frac{j}{R_0} - \frac{1}{R_0^2} + 1\right]\sin\theta \quad (6.204)$$

$$e_{m\theta} = \frac{e^{-jR_0}}{2R_0}\left[\frac{krkz_0\sin^2\theta}{R_0^2}\left(\frac{3}{R_0^2} + \frac{3j}{R_0} - 1\right) - \left(\frac{j}{R_0} + \frac{1}{R_0^2} - 1\right)\cos\theta\right] \quad (6.205)$$

$$e_{m\phi} = -j\frac{e^{-jR_0}}{2R_0}\left[\frac{j}{R_0} + \frac{1}{R_0^2} - 1\right] \quad (6.206)$$

$$h_{mr} = \frac{e^{-jR_0}}{2R_0}\left[\frac{j}{R_0} + \frac{1}{R_0^2}\right]kz_0\sin\theta \quad (6.207)$$

$$h_{m\theta} = \frac{e^{-jR_0}}{2R_0}\left[\frac{j}{R_0} + \frac{1}{R_0^2}\right](kr - kz_0\cos\theta) \quad (6.208)$$

$$h_{m\phi} = j\frac{e^{-jR_0}}{2R_0}\left[\frac{j}{R_0} + \frac{1}{R_0^2}\right](kr\cos\theta - kz_0) \quad (6.209)$$

where $m = \pm 1$. For all other m, the coefficients are zero. Additional field components needed in the finite element portion of the system are e_{mt} and h_{mt} and are given by

$$e_{mt} = e_{mr}\cos(\theta - v) - e_{m\theta}\sin(\theta - v) \quad (6.210)$$

$$h_{mt} = h_{mr}\cos(\theta - v) - h_{m\theta}\sin(\theta - v) \quad (6.211)$$

where the identities

$$\hat{r} = \hat{t}\cos(\theta - v) + \hat{n}\sin(\theta - v) \quad (6.212)$$

$$\hat{\theta} = -\hat{t}\sin(\theta - v) + \hat{t}\cos(\theta - v) \quad (6.213)$$

have been involved in deriving (6.210) and (6.211).

6.5   Scattered Field Computation

Once the modal coefficients are determined from the solution of (6.76), the goal is to proceed with the determination of the scattered or radiated field. In the following, the evaluation of these from a knowledge of the modal scattered field coefficients is discussed.

The scattered fields in the far zone are given by

$$\overline{E}^s(\overline{r}) = E_\phi(\overline{r})\hat{\phi} + \eta_0 H_\phi(\overline{r})\hat{\theta} \tag{6.214}$$

$$\eta_0 \overline{H}^s(\overline{r}) = \eta_0 H_\phi(\overline{r})\hat{\phi} - E_\phi(\overline{r})\hat{\theta} \tag{6.215}$$

These involve the ϕ components of the electric and magnetic fields and these are related to the modal field components via the Fourier series as

$$E_\phi^s(r,\theta,\phi) = 2j \sum_{m=1}^{M} e_{m\phi}^s(r,\theta) \sin(m\phi) \tag{6.216}$$

$$\eta_0 H_\phi^s(r,\theta,\phi) = h_0^s(r,\theta) + 2 \sum_{m=1}^{M} h_{m\phi}^s(r,\theta) \cos(m\phi) \tag{6.217}$$

and that for the θ-polarized receiver, and by the series

$$E_\phi^s(r,\theta,\phi) = e_0^s(r,\theta) + 2 \sum_{m=1}^{M} e_{m\phi}^s(r,\theta) \cos(m\phi) \tag{6.218}$$

$$\eta_0 H_\phi^s(r,\theta,\phi) = 2j \sum_{m=1}^{M} h_{m\phi}^s(r,\theta) \sin(m\phi) \tag{6.219}$$

for the ϕ-polarized receiver. For a unity amplitude incident field, these imply the radar cross section formulae (2.33)

$$\sigma_{\phi\phi} = \lim_{r \to \infty} \frac{1}{4\pi} \left| \tilde{e}_{0\phi}^s + 2 \sum_{m=1}^{M} \tilde{e}_{m\phi}^s(r,\theta) \cos(m\phi) \right|^2 \tag{6.220}$$

$$\sigma_{\phi\theta} = \lim_{r \to \infty} \frac{1}{4\pi} \left| \tilde{h}_{0\phi}^s + 2 \sum_{m=1}^{M} \tilde{h}_{m\phi}^s(r,\theta) \cos(m\phi) \right|^2 \tag{6.221}$$

$$\sigma_{\theta\phi} = \lim_{r \to \infty} \frac{1}{4\pi} \left| 2 \sum_{m=1}^{M} \tilde{h}_{m\phi}^s(r,\theta) \sin(m\phi) \right|^2 \tag{6.222}$$

$$\sigma_{\theta\theta} = \lim_{r \to \infty} \frac{1}{4\pi} \left| 2 \sum_{m=1}^{M} \tilde{e}_{m\phi}^s(r,\theta) \sin(m\phi) \right|^2 \tag{6.223}$$

where

$$\tilde{e}_{m\phi}^s = 4\pi r \; e_{m\phi}^s \tag{6.224}$$

$$\tilde{h}_{m\phi}^s = 4\pi r \; h_{m\phi}^s \tag{6.225}$$

The evaluation of $e^s_{m\phi}$ and $h^s_{m\phi}$ in the far zone using the near field values.

The Stratton-Chu integral equation used for calculating the scattered fields was discretized in section 6.3.2. For the potential distribution computed by solving the system (6.76), and these values are known on any path Γ_f passing through the solution region Ω and which encloses the scatterer. By subdividing Γ_f into N_f contour (boundary) elements, the scattered field may be expressed in a form similar to (6.136) as

$$e^s_{m\phi} = \begin{bmatrix} P_\phi & P_t & Q_\phi & Q_t \end{bmatrix} \begin{bmatrix} \psi^s_e \\ \psi^s_{et} \\ \psi_h \\ \psi^s_{ht} \end{bmatrix} \qquad (6.226)$$

where

$$P_\phi = \sum_{e'=1}^{N_f} \sum_{j=1}^{2} \{P_\phi\}_j^{e'} \qquad (6.227)$$

$$Q_\phi = \sum_{e'=1}^{N_f} \sum_{j=1}^{2} \{Q_\phi\}_j^{e'} \qquad (6.228)$$

$$P_t = \sum_{e'=1}^{N_f} \sum_{j=1}^{2} \{P_t\}_j^{e'} \qquad (6.229)$$

$$Q_t = \sum_{e'=1}^{N_f} \sum_{j=1}^{2} \{Q_t\}_j^{e'} \qquad (6.230)$$

and in which

$$\{P_\phi\}_j^{e'} = \frac{2\pi}{k_0} \int_0^{\Delta^{e'}} N_j^{e'} \left[R' \cos v' g_m^{(1)'} - R \cos v' g_m + (Z - Z') \sin v' g_m^{(1)'} \right] d\tau' \qquad (6.231)$$

$$\{Q_\phi\}_j^{e'} = \frac{2\pi}{k_0} \int_0^{\Delta^{e'}} \left\{ N_j^{e'} \left[j \sin v' g_m^{(2)} \right] - (\tfrac{\partial}{\partial \tau'} N_j^{e'}) \left[j R' g_m^{(2)'} \right] \right\} d\tau' \qquad (6.232)$$

$$\{P_t\}_j^{e'} = \frac{2\pi}{k_0} \int_0^{\Delta^{e'}} N_j^{e'} \left[j(Z - Z') g_m^{(2)'} \right] d\tau' \qquad (6.233)$$

$$\{Q_t\}_j^{e'} = \frac{2\pi}{k_0} \int_0^{\Delta^{e'}} N_j^{e'} \left[g_m^{(1)} + jm g_m^{(2)'} \right] d\tau' \qquad (6.234)$$

which must be specialized for far zone ($r \to \infty$) computations. In deriving expressions for the far fields, the argument of the Green's function is replaced by its usual far zone approximation

$$\tilde{R} = \sqrt{R^2 + R'^2 - 2RR'\cos u + (Z - Z')^2} \sim k_0 r - Z'\cos\theta - R'\cos u \sin\theta \quad (6.235)$$

where

$$Z = k_0 r \cos\theta \quad (6.236)$$

$$R = k_0 r \sin\theta \quad (6.237)$$

The Green's function and its derivative may then be written as

$$g \sim \frac{e^{-jk_0 r}}{4\pi r} e^{j(Z'\cos\theta + R'\cos u \sin\theta)} \quad (6.238)$$

$$\frac{1}{\tilde{R}}\frac{\partial g}{\partial \tilde{R}} \sim -\frac{j}{k_0 r}g \quad (6.239)$$

and when these are used in (6.118) – (6.122), we obtain

$$g_m^{(1)} \sim \frac{e^{-jk_0 r}}{4\pi r} f_{cm}(\theta, R') \, e^{jZ'\cos\theta} \quad (6.240)$$

$$g_m^{(2)} \sim \frac{e^{-jk_0 r}}{4\pi r} f_{sm}(\theta, R') \, e^{jZ'\cos\theta} \quad (6.241)$$

$$g_m' \sim -\frac{j}{k_0 r}\frac{e^{-jk_0 r}}{4\pi r} f_m(\theta, R') \, e^{jZ'\cos\theta} \quad (6.242)$$

$$g_m^{(1)'} \sim -\frac{j}{k_0 r}\frac{e^{-jk_0 r}}{4\pi r} f_{cm}(\theta, R') \, e^{jZ'\cos\theta} \quad (6.243)$$

$$g_m^{(2)'} \sim -\frac{1}{k_0 r}\frac{e^{-jk_0 r}}{4\pi r} f_{sm}(\theta, R') \, e^{jZ'\cos\theta} \quad (6.244)$$

where

$$f_m(\theta, R') = j^m J_m(R'\sin\theta) \quad (6.245)$$

$$f_{cm}(\theta, R') = j^{m-1} J_m'(R'\sin\theta) \quad (6.246)$$

$$f_{sm}(\theta, R') = -\frac{m}{R'\sin\theta} f_m(\theta, R') \quad (6.247)$$
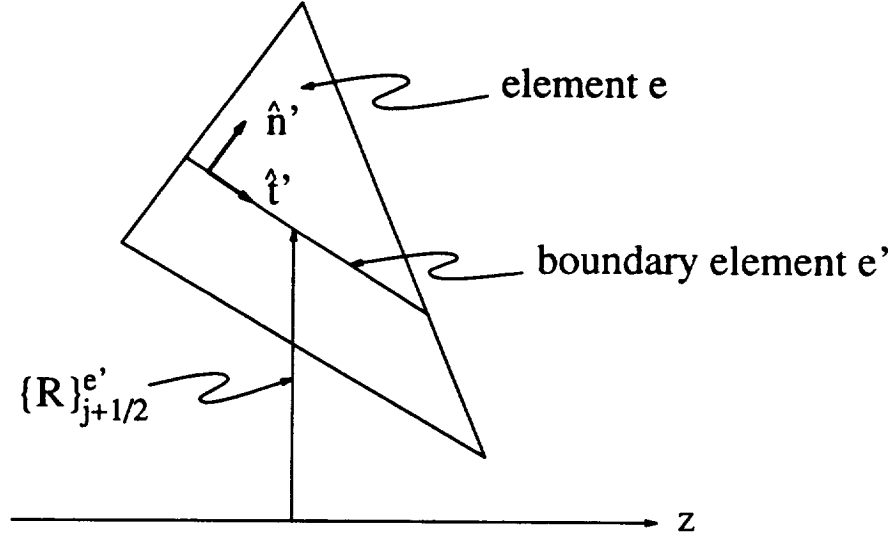
Figure 6.5: The configuration of a typical boundary element e' passing through triangular element e

Furthermore, substituting (6.236) and (6.237) into (6.231) – (6.234) yields

$$\{P_\phi\}_j^{e'} \sim -j\frac{e^{-jk_0r}}{2k_0r} \int_0^{\Delta_{e'}} N_j^{e'}(\tau')[\cos\theta\sin v'f_{cm} - \sin\theta\cos v'f_m]\, e^{jZ'\cos\theta}d\tau' \quad (6.248)$$

$$\{Q_\phi\}_j^{e'} \sim j\frac{e^{-jk_0r}}{2k_0r} \int_0^{\Delta_{e'}} N_j^{e'}(\tau')\sin v'f_{sm}\, e^{jZ'\cos\theta}d\tau' \quad (6.249)$$

$$\{P_t\}_j^{e'} \sim -j\frac{e^{-jk_0r}}{2k_0r} \int_0^{\Delta_{e'}} N_j^{e'}(\tau')\cos\theta f_{sm}\, e^{jZ'\cos\theta}d\tau' \quad (6.250)$$

$$\{Q_t\}_j^{e'} \sim \frac{e^{-jk_0r}}{2k_0r} \int_0^{\Delta_{e'}} N_j^{e'}(\tau')f_{cm}\, e^{jZ'\cos\theta}d\tau' \quad (6.251)$$

If e_{mt}^s and h_{mt}^s are not known on Γ_f, then they must be computed by numerically differentiating the potentials for each triangular element traversed by Γ_f. For convenience, it is assumed that the e'th boundary element passes through the eth triangular as indicated in Fig. 6.5 (i.e., the boundary element must begin at one edge of the triangle and end on another). In this case, e_{mt}^s is found by first taking the dot product of $\hat{n}'$ (the outward normal of Γ_f) with (6.22) to obtain

$$je_{mt}^s = -f_m[m\,\hat{t}\cdot\nabla_t\psi_e^s - R\,\hat{n}\cdot\nabla\psi_h^s] \quad (6.252)$$

Since in the eth triangular element

$$\{\psi_e^s\}^e = \sum_{j=1}^{3} N_j^e \{\psi_e^s\}_j^e \qquad (6.253)$$

we have

$$\nabla_t \{\psi_e^s\}^e = \sum_{j=1}^{3} \nabla_t N_j^e \{\psi_e^s\}_j^e \qquad (6.254)$$

where

$$N_j^e = \frac{\alpha_j^e + \beta_j^e Z + \gamma_j^e R}{2\Omega^e} \qquad (6.255)$$

$$\nabla_t N_j^e = \frac{\beta_j^e \hat{z} + \gamma_j^e \hat{\rho}}{2\Omega^e} \qquad (6.256)$$

Further, on noting the identities

$$
\begin{aligned}
\hat{t}' \cdot \hat{z}' &= \cos v' & \hat{t}' \cdot \hat{\rho}' &= \sin v' \\
\hat{n}' \cdot \hat{z}' &= -\sin v' & \hat{n}' \cdot \hat{\rho}' &= \cos v'
\end{aligned}
\qquad (6.257)
$$

the derivatives can be written more explicitly as

$$\hat{n}' \cdot \nabla_t \{\psi_e^s\}^e = \sum_{j=1}^{3} \frac{-\beta_j^e \sin v' + \gamma_j^e \cos v'}{2\Omega^e} \{\psi_e^s\}_j^e \qquad (6.258)$$

$$\hat{t}' \cdot \nabla_t \{\psi_e^s\}^e = \sum_{j=1}^{3} \frac{\beta_j^e \cos v' + \gamma_j^e \sin v'}{2\Omega^e} \{\psi_e^s\}_j^e \qquad (6.259)$$

A similar procedure is used for $\hat{n}' \cdot \nabla_t \{\psi_h^s\}^e$ and $\hat{t}' \cdot \nabla_t \{\psi_h^s\}^e$ and substituting these into (6.252) gives

$$\{R\}_{j+\frac{1}{2}}^{e'} \{je_{mt}^s\}_{j+\frac{1}{2}}^{e'} = -\frac{\{R\}_{j+\frac{1}{2}}^{e'}}{[\{R\}_{j+\frac{1}{2}}^{e'}]^2 - m^2} \left[m\hat{t}' \cdot \nabla_t \psi_e^s - \{R\}_{j+\frac{1}{2}}^{e'} \hat{n}' \cdot \nabla \psi_h^s \right] \quad (6.260)$$

$$\{R\}_{j+\frac{1}{2}}^{e'} \{jh_{mt}^s\}_{j+\frac{1}{2}}^{e'} = -\frac{\{R\}_{j+\frac{1}{2}}^{e'}}{[\{R\}_{j+\frac{1}{2}}^{e'}]^2 - m^2} \left[m\hat{t}' \cdot \nabla_t \psi_h^s + \{R\}_{j+\frac{1}{2}}^{e'} \hat{n}' \cdot \nabla \psi_e^s \right] \quad (6.261)$$

where $\{R_{j+\frac{1}{2}}^{e'}\}$ is introduced to express the left hand side as an azimuthal potential. The second of these is derived by a similar procedure, or via duality. For the special case of Γ_f coinciding with Γ_a, then the e_{mt}^s and h_{mt}^s are computed during the system solution. Then the need to compute the $\hat{t}-$ components is unnecessary.

6.6 Code Validation and Performance

In this section, the numerical implementation of the FE–BI method is evaluated in terms of storage and computational efficiency and accuracy. Also, the method for eliminating the boundary integral resonances presented in chapter V is tested here for spherical enclosures. Finally, the scattering from several structures is presented for validation purposes.

6.6.1 Storage Efficiency

This implementation of the FE–BI method discussed in this chapter differs from the two-dimensional FE–BI formulation discussed earlier in that arbitrarily shaped mesh terminations are allowed. As a result, an increased storage efficiency is not obtained from the convolutional properties of the boundary integral operator, but is instead realized by exploiting matrix symmetries. It is, nevertheless, understood that the controlling factor in the storage of large FE–BI systems is the dense boundary integral subsystem, which grows as $O(n^2)$ for n unknowns on the boundary, while the interior FE system grows as $O(N)$ for N unknowns in the interior region.

It is possible, however, to choose an enclosure on which some of the integrals are convolutional. The Green's function in (6.93) appearing in the integrand of the integral equations (6.91) is a function of the distance between the source and field points, which when expressed in cylindrical coordinates takes the form

$$|\bar{r} - \bar{r}'| = \sqrt{\rho^2 + \rho'^2 - 2\rho\rho' \cos(\phi - \phi') + (z - z')^2} \qquad (6.262)$$

After employing the Fourier series expansion of the field quantities and Green's functions, the azimuthal dependency is removed and the result is given by (6.128). This expression is a convolution only on contours parallel to the z-axis. Consequently,

a suitable enclosure is rectangular in shape, generating a right circular cylinder in three-dimensional space. Though analogous to the two-dimensional rectangular enclosure explored in chapter III, the integrals are in the form of convolutions only when source and observation points lie on the portion of Γ_a which is parallel to the z-axis. All remaining terms are considered "cross terms" and must be stored efficiently, relying on symmetry to achieve this goal.

The discrete version of a typical boundary integral equation block matrix (of L_t, say) has the form

$$\begin{bmatrix} a_{11} & a_{12} & a_{13} \\ a_{21} & a_{22} & a_{23} \\ a_{31} & a_{32} & a_{33} \end{bmatrix} \tag{6.263}$$

where the subscripts of a_{pq} denote the observation on side p and source on side q of the rectangular boundary (the z-axis is not applicable to the boundary integral). As a consequence of the convolution, a_{22} is Toeplitz in form and, effectively, only the first row need be stored when an FFT is employed to evaluate the associated matrix-vector products. For a_{22} to dominate the storage requirement of the BI system, the enclosure must be long with respect to its radius. For scatterers not satisfying this requirement, the reduction of a_{22} is not substantial. Consequently, the method was abandoned in favor of a general conformal boundary.

To determine the storage requirement for a general boundary, it is first noted that each matrix in the BI subsystem of (6.148) need only be stored once. Additionally, after examining (6.141) – (6.144) M_t and L_t are the only symmetric matrices. Thus, for n nodes on the boundary the storage for the each of the symmetric matrices is $n(n + 1)/2$ and that for the unsymmetric matrices is n^2. The overall storage requirement of the BI matrix is then $n(3n - 1)$. Though this continues to be $O(n^2)$,

the constant in front is reduced from 8 to approximately 3. For the particular case of a purely smooth metallic scatterer, the full storage requirement of the standard surface integral equation (SIE) for BOR structures is $4n^2$, slightly less than that of the FE–BI system. However, for structures such as a corrugated cylinder, n becomes very large for the SIE but in the case of the FE–BI method, the termination boundary may be chosen to occupy a minimum path and thereby minimizing the associated storage requirement.

In passing we note that it is possible to optimize the storage by choosing the termination boundary far enough from the scatterer so as to reduce the sampling the requirement of the boundary integral (which grows as $O(n^2)$), but without substantially increasing the storage associated with the additional elements required in the finite element region (which grows as $O(N)$). This is particularly useful for structures containing very thin high contrast material layers, in which case a strictly conformal boundary would result in a large number of unknowns on the boundary.

For a given amount of data storage space, S [bytes], the maximum allowable length l of the termination boundary depends on the uniform sampling rate Δ as

$$l = n\Delta \tag{6.264}$$

The single precision (8 bytes) storage requirement for the discrete boundary integral thus becomes

$$S = 24 \left(\frac{l}{\Delta} \right)^2 \tag{6.265}$$

and then solving for the length,

$$l = \Delta \sqrt{\frac{S}{24}} \tag{6.266}$$

Thus, if $S = 10$ megabytes and $\Delta = \lambda/20$

$$l \simeq 32\lambda \tag{6.267}$$

This represents an upper limit on l given the memory and sampling rate without regard to the finite element storage nor the overhead associated with the geometry and solution storage, which mutually grow as $O(N)$. Consequently in practice, $n = \frac{l}{\Delta}$ must be reduced until the storage of the entire model is accomodated, a requirement which depends on the scattering body.

6.6.2 Computational Efficiency and Accuracy

The FE–BI system given by (6.148) is solved via the conjugate gradient method. It is well known that the rate of convergence is proportional to κ^2, where κ is the condition number of the matrix. Clearly, those factors which influence κ must be examined, since in part, cpu time of the solver and subsequently the accuracy of the solution depends on this.

Since the FE–BI system is comprised of two incomplete subsystems, it is expected that the weakness from each portion contributes to a reduction in κ. Among those due to the finite element subsystem, are the shape and size of the element, and also the lines of singularity at $R_0 = \frac{m}{\kappa}$ for real κ, discussed previously. Elongated elements yield larger matrix values than an equilateral triangle of the same area, and the line singularities produce matrix values roughly two orders of magnitude larger than the average matrix value. The combination of large and small matrix elements can undermine the condition of the matrix.

Those factors influencing the BI portion are the element size and the total number of boundary elements. Elements which are very small ($< 0.01\lambda$) result in subsequent rows which are nearly equal and give the appearance of a singular matrix. Large dense systems are known to have a smaller κ simply because of the number of matrix elements.
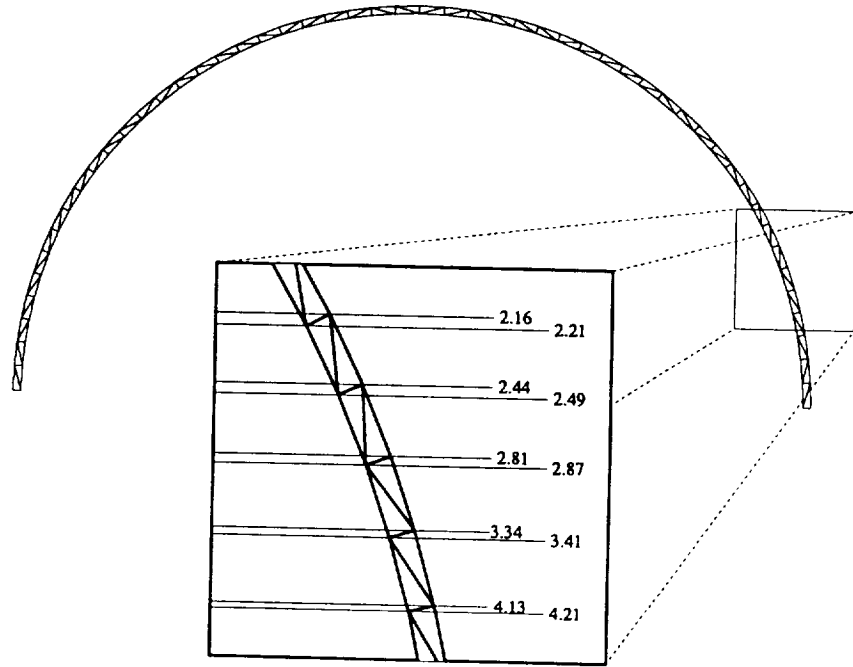
(a)
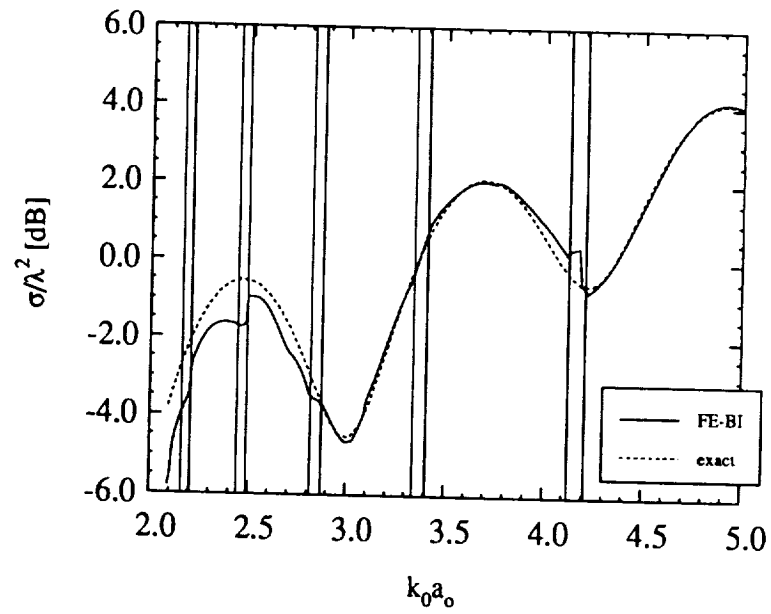
(b)

Figure 6.6: The mesh used for the frequency sweep of a conducting sphere is shown in (a) and the expanded region shows the values of ka at which the line singularity intersects the nodes. The frequency sweep in (b) demonstrates the inaccuracies associated with the line singularities
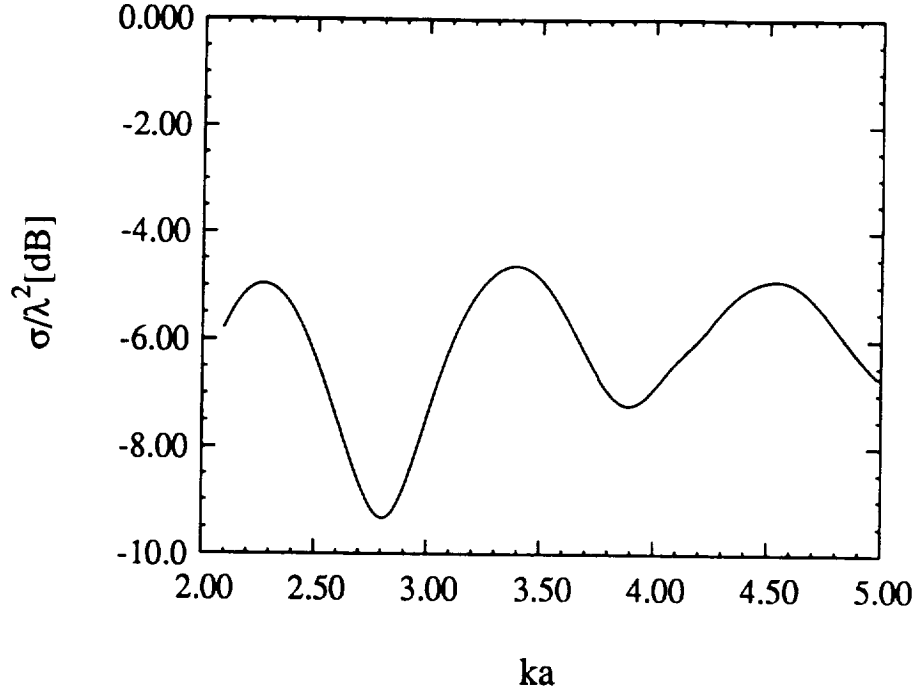
Figure 6.7: A sphere coated with $\mu_r = \epsilon_r = 1 - j5$ is swept in frequency

The issue of accuracy, which is closely tied to the issue of system condition, is examined as a function of frequency for two spheres. Each is comprised of a conductor of radius a with a mesh termination at $a_o = 1.02a$. The second sphere contains dielectric material with $\epsilon_r = \mu_r = 1 - j5$ in the finite element region. As seen in Fig. 6.6, there are locations where the solution has a large error with respect to the exact result [27], plotted as a function of the outer radius normalized to the free space wavenumber k_0. The vertical lines denote the regions of greatest change, and from (a), it is clear that the edge of an element is nearly parallel to this line. This problem, discussed previously in section 6.2.3, is due to the fact the matrix elements are becoming large and the sensitive cancellation required is not occurring accurately. When a lossy coating is introduced, the line-singularity is no longer present, and as shown in Fig. 6.7, the results follow quite well with the moment method data.

6.6.3 Elimination of the Internal Resonance Corruption of the Boundary Integral

The corruption of the solution due to interior resonances of the boundary integral perseveres in the three-dimensional case. The approach taken in chapter 3 is also employed here. It is again shown that for the coated sphere test structure, the "complexification" of the wavenumber in conjunction with the scattered field FE–BI formulation successfully removes the resonances. Since the theory surrounding the method was previously presented, it will not be repeated here.

Consider the conducting sphere of radius a enclosed in a boundary of radius $a_o = 1.02a$ and $\epsilon_r = 2 - j4$. Shown in Fig. 6.8 is σ as a function of ka_o of the outer boundary for axial incidence and observation (thus requiring the solution for the $m = 1$ mode). Clearly, the expected resonances indicated by the vertical lines are present and are evident in the solution for $\alpha = 1$ by the spiked behavior, except at $k_0 a_o \simeq 10.6$ at which the resonance is shifted due to numerical errors. These are eliminated by setting $k = \alpha k_0$ and the results for $\alpha = 0.005$, $\alpha = .007$ and $\alpha = .01$ are presented in the same figure. As seen by these it is clear that the solution is relatively insensitive to α.

6.6.4 Scattering from Various Test Bodies

To validate the code, bistatic scattering patterns are considered in the four various sample targets. In each case the radar cross section in (2.33) is computed and the results are compared to a moment method solution [25, 19]. Most of the cases considered involve axial incidence (along the z-axis) and in this case TE_z and TM_z no longer have meaning. Planes defined by the electric field vector and the z-axis form the E-plane, and the magnetic field vector and the z-axis form the H-plane.
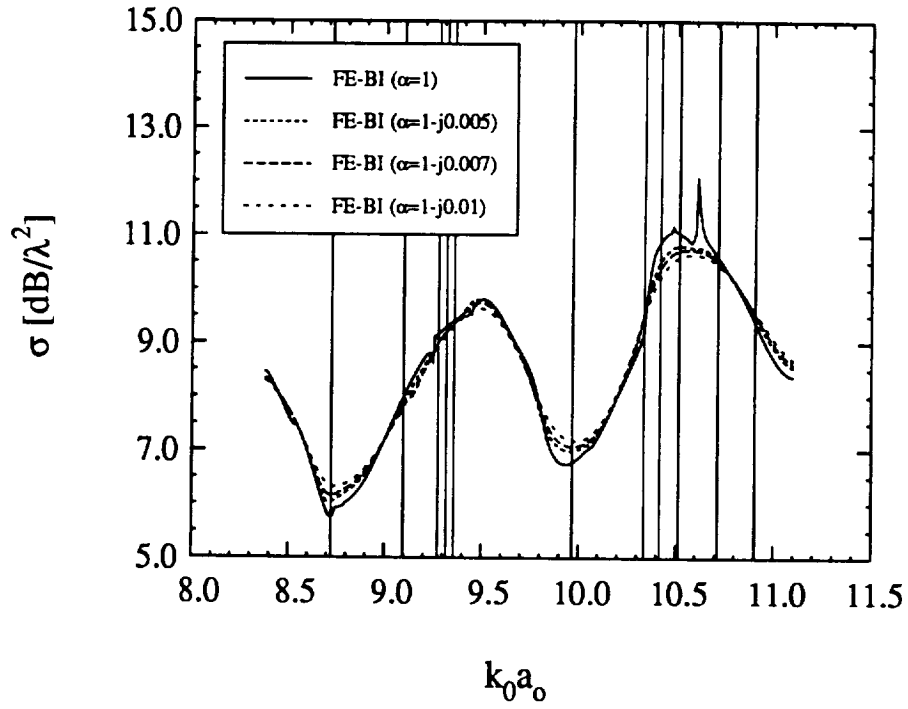
Figure 6.8: The axial backscatter cross section is displayed as a function of normalized radius $k_0 a_o$. The structure is a conducting sphere of radius a coated with a dielectric with $\epsilon_r = 2 - j4$ has an outer radius of $a_o = 1.02$. Employing a complex wavenumber $k = k_0 \alpha$, the resonance behavior is removed for the complex values in comparison to the $\alpha = 1$ case

The patterns shown are computed in these planes.

First we consider the scattering from a coated conducting sphere of radius $0.098m$ with a $0.02m$ coating with $\epsilon_r = 2 - j4$. Fig. 6.9a demonstrates the convergence of the solution as more Fourier harmonics are summed together, and shown are the partial sums up to m=10. Fig. 6.9b shows the final converged result of the (a) (plotted on a scale shifted by -60 degrees to coincide with the pattern due to axial incidence) along with the axial incident result (requiring only m=1). Only the E-plane patterns were computed. A comparison to a method of moments result demonstrates agreement.

Next we consider the scattering from a perfectly conducting sphere of radius 1λ as indicated in Fig. 6.10. Both E-plane and H-plane patterns are included and the comparison with moment method results is favorable.

In Fig. 6.11 is shown the patterns for a $2\lambda \times 0.176\lambda$ perfectly conducting ogive with a dielectric coating of thickness 0.05λ with $\epsilon_r = 2 - j2$, shown for an axially incident plane wave. Both E-plane (TE_z) and H-plane (TM_z) are shown along with data generated via the moment method.

Next we consider the case of a coated sphere-capped cone frustum, the mesh of which is indicated in Fig. 6.12. The structure is 4λ in length, the spheres are of radii 1λ and $\frac{\lambda}{2}$ and the coating thickness $\frac{\lambda}{20}$. Additionally, the material is dielectric with $\epsilon_r = 4 - j5$. The bistatic cross section computed for this structure for an axially incident plane wave is indicated for TE_z (or E-plane) and TM_z (or H-Plane) incidence in Fig. 6.13. Reference data provided indicates a good agreement.
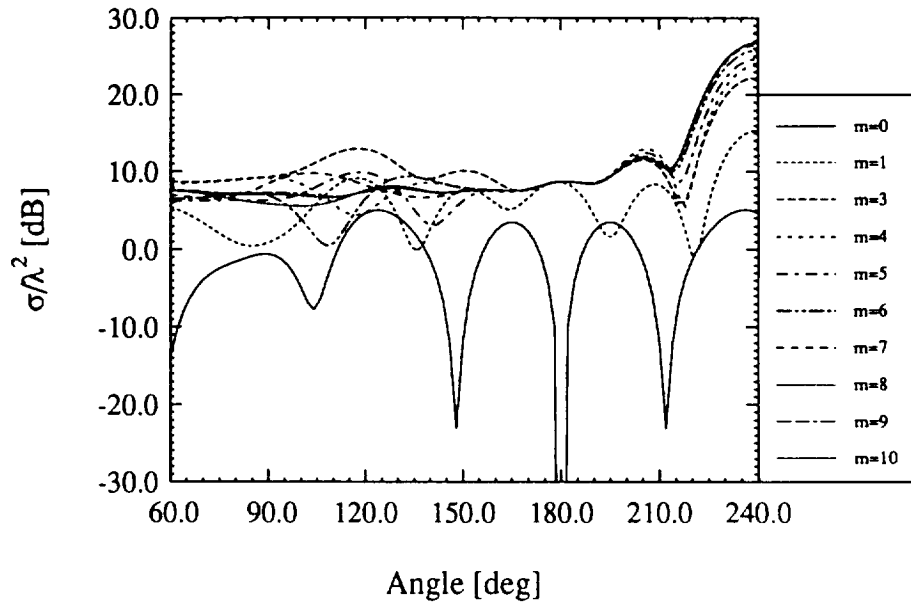
(a)
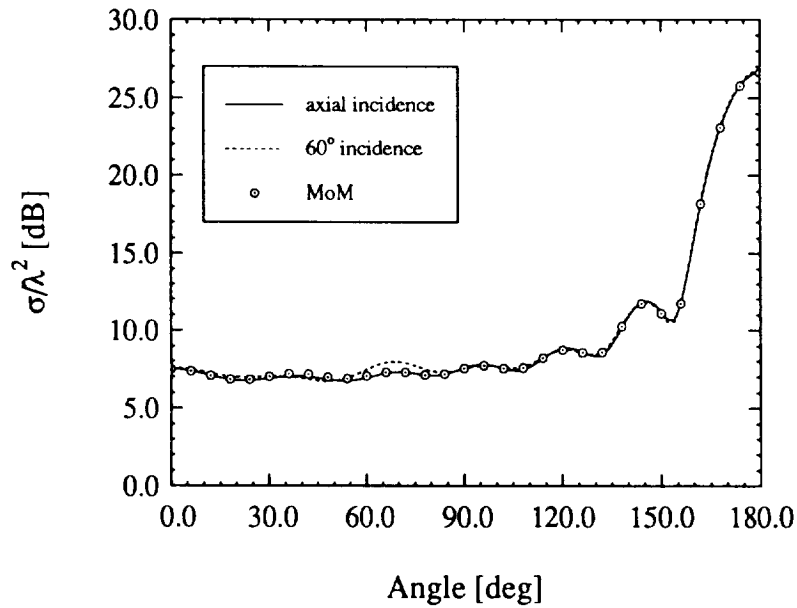
(b)

Figure 6.9: The bistatic scattering pattern for a coated sphere. (a) Shows the summation of modes converging to the correct solution for an incidence of 60 degrees. The converged solution for modes 0-10 at 60 degrees (plotted on a scale shifted by -60 degrees to coincide with the pattern due to axial incidence) shown with the axial incident result and a comparison to moment method results
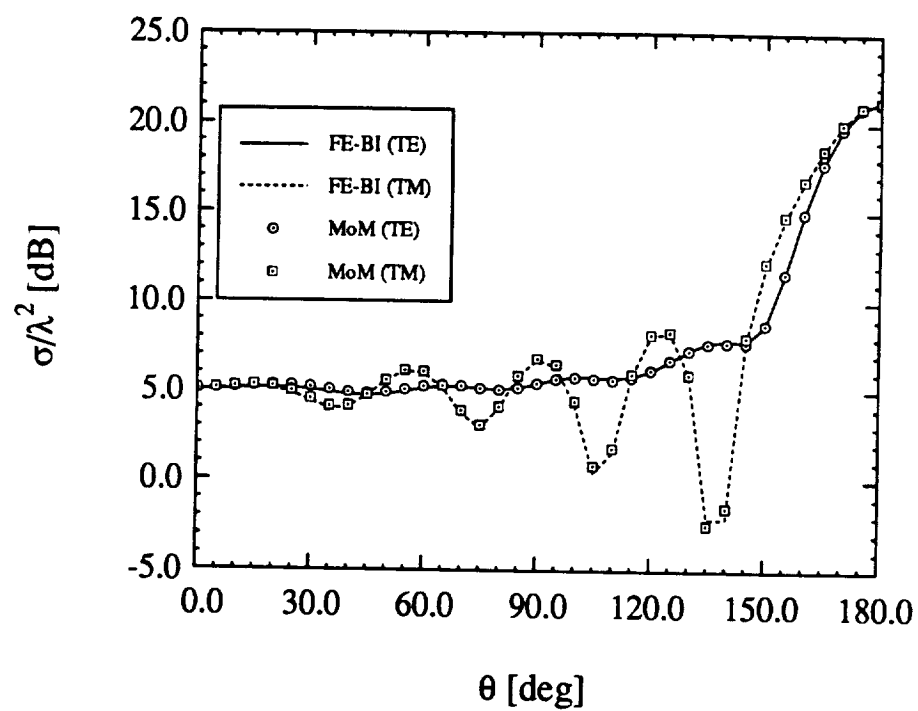
Figure 6.10: The bistatic scattering pattern for a perfectly conducting sphere of radius 1λ. Both E-plane (TE) and H-plane (TM) are shown along with data generated via the moment method
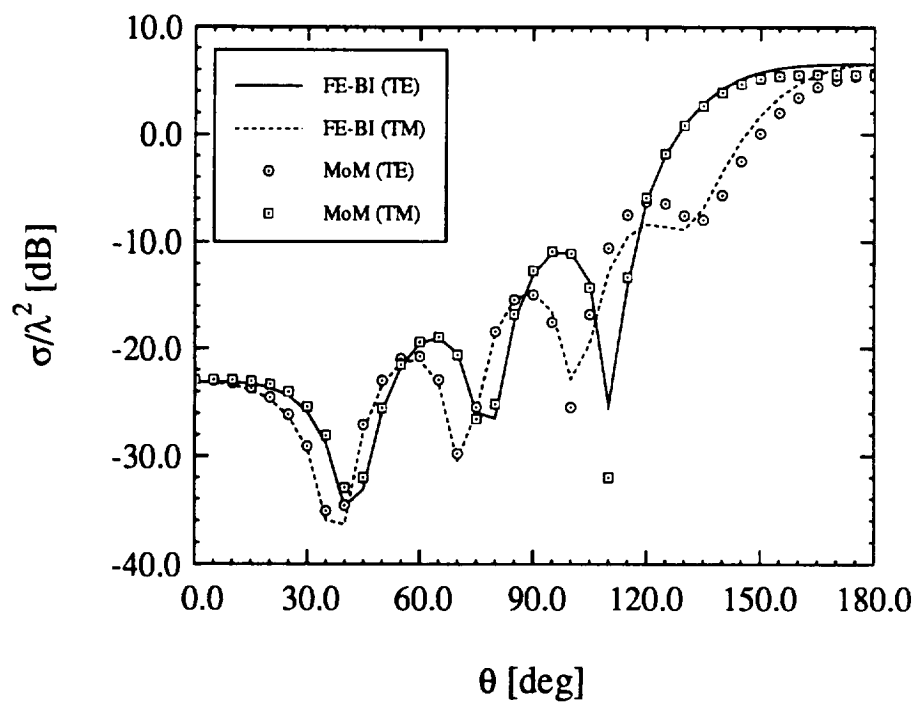
Figure 6.11: The bistatic scattering pattern for a $2\lambda \times 0.176\lambda$ perfectly conducting with a $.0.05\lambda$ coating with $\epsilon_r = 2 - j2$ for an axially incident plane wave. Both E-plane (TE) and H-plane (TM) are shown along with data generated via the moment method
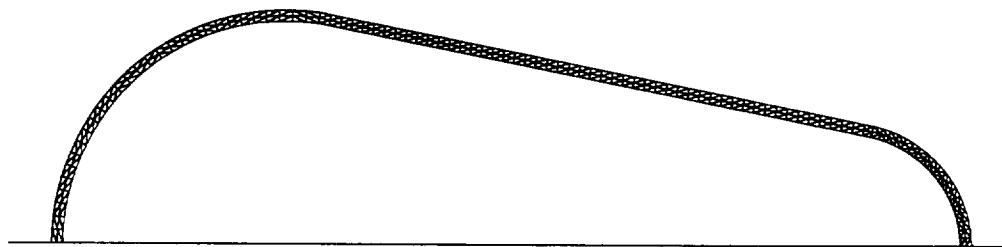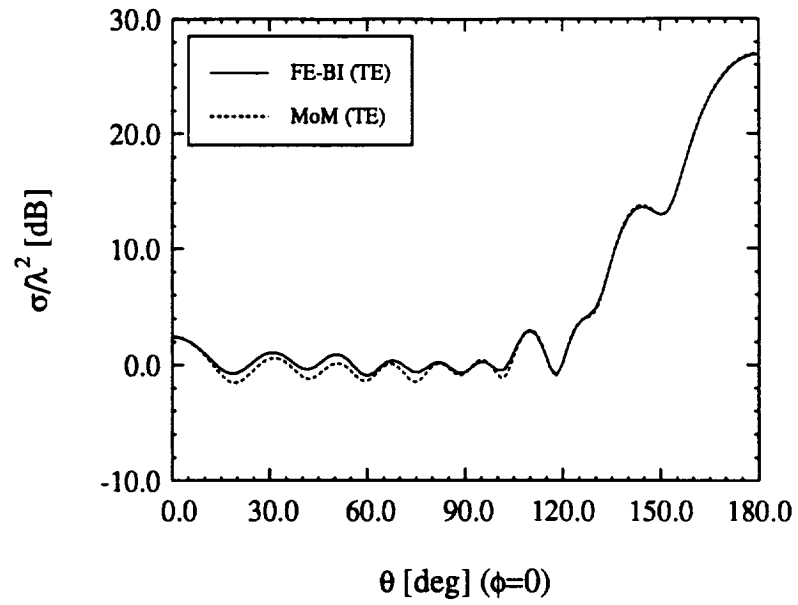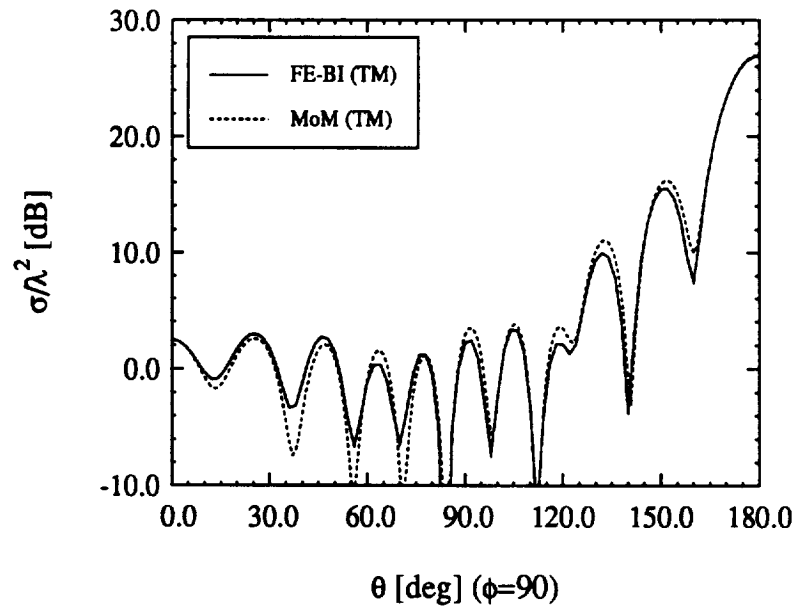

Figure 6.12: The mesh of the sphere-capped cone frustrum

(a)

(b)

Figure 6.13: The bistatic scattering pattern is shown for a plane wave axially incident on the coated sphere-capped cone frustum. Part (a) shows the E-plane pattern, while (b) demonstrates the H-plane pattern

6.7   Conclusions

We have presented the finite element - boundary element formulation for axially symmetric bodies. The storage requirement associated with the boundary integral was reduced by symmetry considerations. Several patterns were generated to demonstrate the validity of the method, and the model shortcomings were presented as well. Also, a method for eliminating the problem of the line singularity inherent in the CAP finite element formulation was given and was shown to give real matrices for lossless structures. It should be noted that frequency sweeps and single mode radiation problems make the most efficient use of the employed CG solver. The method is not well suited, however, to problems incorporating multiple excitations or those requiring many Fourier modes.

CHAPTER VII

Conclusion

7.1 Summary

In this thesis, the FE–BI technique (presented in general terms in chapter II) was developed for two-dimensional and axially symmetric structures. The two-dimensional case was based on the moment-method version developed by Jin [9]. An FE–BI formulation for rectangular enclosures was developed in Chapter III and lead to simple boundary integrals some of which had convolutional form which was exploited for reducing the memory requirement. In chapter IV, circular and ogival enclosures were considered. For the circular boundary, the boundary integral was entirely convolutional in form and an $O(N)$ storage requirement was thus achieved at all times. It was shown that circular enclosures are consequently preferred for storage efficiency if the structure's outer boundary does not substantially deviate from a circle.

In chapter VI, the FE–BI formulation was developed for axially symmetric structures. The finite element method for this problem was based on the CAP equations for generating the FE matrix system, and a boundary integral equation was used for the boundary condition on an arbitrarily shaped mesh termination boundary. Consequently the boundary integrals were no longer convolutional and a storage reduction

was, instead, achieved by exploiting certain symmetry properties of the boundary integral subsystem. Also, a new method was presented for circumventing the singularity problem associated with the CAP equations in the finite element portion of the system.

A method was developed in chapter V for eliminating the internal resonance corruption of the solution, a difficulty found with most boundary integral formulations. These resonances correspond to the eigenvalues of the integral operator, and may be also viewed as the cut-off frequencies of a resonator with conducting walls of the same shape as the mesh termination boundary. Because the eigenvalues become very closely spaced for electrically large structures, any scattering computations become unreliable unless the resonances are suppressed.

In summary, specific contributions of this work include the development and implementation of the FE–BI for rectangular, circular and ogival boundaries as described in chapters III and IV in a manner taking advantage of storage reduction schemes. A new method was also presented for suppressing resonance corruptions existing in almost all implementations employing some form of a boundary integral equation over a closed surface or contour. This method involved the introduction of a complex wavenumber and was demonstrated for both 2-D and axially symmetric bodies. The implementation of the FE–BI method for axially symmetric structures as described in chapter VI was for the most part new and incorporated a scheme for treating the line singularity associated with the CAP equations. This resulted in real matrices for lossless scatterers, a property consistent with 2-D and 3-D implementations of the finite element method.

7.2 Future Work

The FE–BI technique presented in this work remains a promising technique for computing the scattering from ever larger structures. However, as the structure increases in size, so does the condition number of the resulting system due in part to its size. To reduce the number of unknowns, higher order basis functions must be used. For electromagnetic scattering, bases formed with hierarchical functions [5] show promise. Instead of standard functions, in which each undetermined coefficient corresponds to an unknown field quantity, those associated with the hierarchical function are comprised of both field quantities and field errors. For instance, a quadratic hierarchical function for a one-dimensional element takes the form

$$\phi = \sum_{j=1}^{2} N_j^e(x)\phi_j^e + \alpha f(x) \tag{7.1}$$

where $f(x)$ is an arbitrary quadratic function, and the coefficient α is proportion to the deviation of the linear approximation to the quadratic one. Clearly, as higher order terms are added to the sum in (7.1), the smaller the coefficients become. Furthermore, the quadratic function $f(x)$ may be chosen to be approximately orthogonal to polynomials of different order. Thus, in a finite element implementation, the off diagonal elements may become very small increasing the diagonal dominance of the matrix and leading to better matrix conditioning.

The above idea can be extended to include functions other than polynomials. The physical optics solution could be employed as the fundamental solution and linear (or higher order polynomials) functions could then be employed as correcting functions. That is, the unknown coefficients in the solution would then be the deviation of the physical optics solution from the actual one. This could consequently aid in reducing the number of unknowns, particularly if the original approximation was reasonably

good. Note that this technique is applicable for the discretization of the boundary integral and finite element equations.

BIBLIOGRAPHY

BIBLIOGRAPHY

[1] T.K. Sarkar, E. Arvas and S.M. Rao, "Application of FFT and the conjugate gradient method for the solution of electromagnetic radiation from electrically large and small conducting bodies," *IEEE Trans. Antennas Propagat.*, vol. AP-30, pp. 409-418, May 1986.

[2] T.J. Peters, "Computation of the Scattering by Planar and Non-planar Plates using a Conjugate Gradient FFT Method," Ph.D. dissertation, Radiation Laboratory, The University of Michigan, 1988.

[3] K. Barkeshli, "Applications of the CGFFT method in Scattering and Radiation Including Simulations with Impedance Boundary Conditions," Ph.D. Dissertation, The University of Michigan, 1991.

[4] A. Taflove and K.R. Umashankar, "The finite–difference time–domain method for numerical modelling of electromagnetic wave interactions," *Electromagnetics*, vol. 10, pp. 105–126, Jan-June 1990.

[5] O.C. Zienkiewicz and K. Morgan, *Finite Elements and Approximation*, New York: John Wiley and Sons, 1983.

[6] K.K. Mei, "Unimoment method of solving antenna and scattering problems," *IEEE Trans. Antennas Prop.*, vol AP-22, pp. 760-766, Nov. 1974.

[7] P. Silvester and M.S. Hsieh, "Finite-element solution of 2-dimensional exterior field problems," *Proc. Inst. Elec. Eng.*, vol. 118, pp. 1743-1747, Dec. 1971.

[8] B.H. McDonald and A. Wexler, "Finite-element solution of unbounded field problems," *IEEE Trans. Microwave Theory Tech.*, vol. MTT-20, pp. 841-847, Dec. 1972.

[9] Jian-Ming Jin and Valdis V. Liepa, "Application of hybrid finite element method to electromagnetic scattering from coated cylinders," *IEEE Trans. Antennas Propagat.*, vol. AP-36, pp. 50-54, Jan. 1988

[10] A.H.J. Fleming, "A finite element method for composite scatterers,", *Pier 2: Progress in Electromagnetics Research*, ed. M.A. Morgan, Ch. 2.

[11] C.A. Balanis, *Advanced Engineering Electromagnetics*, New York: John Wiley and Sons, 1989.

[12] Harrington, R.F., *Time-Harmonic Electromagnetic Fields*, New York: McGraw-Hill, 1961, p. 203.

[13] M.A. Ricoy and J.L. Volakis, "Integral equations with reduced unknowns for the simulation of two-dimensional composite structures," *IEEE Trans. Antennas Propagat.*, Vol. AP-37, pp. 362-372, 1989.

[14] J.M. Jin and V.V. Liepa, "Simple moment method program for computing scattering from complex cylindrical obstacles," *IEE Proceedings*, Vol. 136, part H, No. 4, pp. 321-329, Aug. 1989.

[15] W.D. Murphy, V. Rokhlin and M.S. Vassiliou, "Solving electromagnetic scattering problems at resonance frequencies," *J. Appl. Phys.*, vol. 67, pp. 6061-6065, May 1990.

[16] A.D. Yaghjian, "Augmented electric- and magnetic-field equation," *Radio Science*, vol. 16, pp. 987-1001, Nov. 1981.

[17] R. Mittra and C.A. Klein, "Stability and convergence of moment method solutions," in *Numerical and Asymptotic Techniques in Electromagnetics*, ed. R. Mittra. New York: Hemisphere, 1987 Reprint.

[18] M.B. Woodworth and A.D. Yaghjian, "Derivation, application and conjugate gradient solution of the dual-surface integral equations for three–dimensional, multi–wavelength perfect conductors," in *PIER 5: Progress in Electromagnetics Research*, ed. Tapan K. Sarkar, Ch. 4.

[19] J.R. Mautz and R.F. Harrington, "H-field, E-field and combined-field solutions for conducting bodies of revolution," AEÜ, pp. 157–164, 1978.

[20] F.X. Canning, "Singular value decomposition of integral equations of EM and applications to the cavity resonance problem," *IEEE Trans. Antennas Propagat.*, vol. AP-37, Sep. 1989.

[21] M.A. Morgan, S.K. Chang and K.K. Mei, "Coupled azimuthal potentials for electromagnetic field problems in inhomogeneous axially symmetric media," *IEEE Trans. Antennas Propagat.*, pp. 413-417, May 1977.

[22] J.A. Stratton, *Electromagnetic Theory*, New York: M Graw-Hill, 1941.

[23] M.A. Morgan, "Numerical computation of electromagnetic scattering by inhomogeneous dielectric bodies of revolution," Ph.D. Dissertation, June 1976.

[24] R.V. Churchill and J.W. Brown, *Complex Variables and Applications*, New York: McGraw–Hill, Inc., 1984.

[25] J.M. Putnam and L.N. Medgyesi-Mitschang, "Combined field integral equation formulation for axially inhomogeneous bodies of revolution," *McDonnell Douglas Research Laboratories report QA003*, Dec 1987.

[26] J.J. Bowman, T.B.A. Senior and P.L.E. Uslenghi, *Electromagnetic and Acoustic Scattering by Simple Shapes*, Amsterdam: North-Holland Publishing Co., 1969.

[27] H.L. Thal, Jr., "Exact circuit analysis of spherical waves," *IEEE Trans. Antennas Propagat.*, pp. 282-287, March 1978.